

Dissertation
submitted to the
Combined Faculties of the Natural Sciences and Mathematics
of the Ruperto-Carola-University of Heidelberg, Germany
for the degree of
Doctor of Natural Sciences

Put forward by
Sebastian Bustamante Jaramillo
born in: Maceo (Colombia)
Oral examination: 24 July 2019

MODELLING SUPERMASSIVE BLACK
HOLE SPINS AND THE METALLICITY
EVOLUTION OF MERGING GALAXIES IN A
COSMOLOGICAL CONTEXT

Referees:

Prof. Dr. Volker Springel

apl. Prof. Dr. Andreas Just

Abstract

Galaxy mergers are a key process in the current paradigm of hierarchical galaxy formation. They are responsible for many galaxy transformations. For instance, they can drive changes in galaxy morphology and colour, boost the star formation activity and trigger strong inflows of pristine gas that dilute the central gas metallicity and feed the central supermassive black hole. To which extent and how galaxy mergers affect some of the galaxy properties are still open questions. In the first part of this thesis, we use simulations and observations to study the processes of merger-induced gas metallicity dilution and star formation enhancement. We find that merging and post-merger galaxies constitute a prominent outlier population in the fundamental metallicity relation, a relation that links the galaxy stellar mass with the star formation rate and the gas metallicity. In the second part of this thesis, we present a sub-grid model of supermassive black hole spin evolution in cosmological simulations of galaxy formation. We find that the accretion discs of low-mass black holes accrete mass in a coherent fashion, resulting in high spin values. On the other hand, high-mass black holes have lower spins because gas accretion is either chaotic or completely suppressed, in which case black hole binary coalescence resulting from galaxy mergers is the only relevant evolution channel. Finally, we test a hypothesis in which the black hole energy feedback transitions from a thermal mode to a kinetic mode at the onset of self-gravity fragmentation in the accretion disc, and is thus coupled to the spin evolution of the black hole. We find that our conjecture reproduces the galaxy colour bimodality and the colour-morphology relation.

Zusammenfassung

Galaxienverschmelzungen sind ein Schlüsselprozess im aktuellen Paradigma der hierarchischen Galaxientstehung. Sie sind für viele Galaxientransformationen verantwortlich. So können sie beispielsweise Veränderungen in der Galaxienmorphologie und -farbe vortreiben und die Sternbildungsaktivität steigern. Außerdem können Galaxienverschmelzungen starke Zuflüsse von reinem, ursprünglichem Gas auslösen, welche die zentrale Gasmetallizität verdünnen und das zentrale supermassereiche Schwarze Loch speisen. Inwieweit sich Galaxienfusionen auf einige der Galaxieneigenschaften auswirken, ist noch offen. Im ersten Teil dieser Arbeit werden Simulationen und Beobachtungen verwendet, um die Prozesse der fusionsbedingten Gasmetallizitätsverdünnung und Sternbildung zu untersuchen. Es wird gezeigt, dass fusionierende und verschmolzene Galaxien eine prominente Ausreißerpopulation in der fundamentalen Metallizitätsrelation darstellen, welche die stellare Galaxienmasse mit der Sternentstehungsrate und der Gasmetallizität verbindet. Im zweiten Teil dieser Arbeit wird ein Subgridmodell der Spinentwicklung von supermassereichen Schwarzen Löchern in kosmologischen Simulationen der Galaxienbildung vorgestellt. Die Akkretionsscheiben von massearmen Schwarzen Löchern akkretieren Materie in kohärenter Weise, was zu hohen Spinwerten führt. Schwarze Löcher mit hoher Masse weisen dagegen niedrigere Spinwerte auf, da die Gasakkretion entweder chaotisch abläuft oder vollständig unterdrückt ist. Im letzteren Fall ist die Verschmelzung zweier Schwarzer Löcher aufgrund von Galaxienfusionen der einzige relevante Evolutionskanal. Schließlich wird eine Hypothese getestet, nach welcher sich die energetische Rückwirkung der Schwarzen Löcher auf das umgebende Gas mit Einsetzen der eigengravitationsbedingten Fragmentierung der Akkretionsscheibe von einem thermischen auf einen kinetischen Modus umstellt und damit direkt an die Entwicklung des Spins gekoppelt ist. Dieses Modell kann die erwartete Bimodalität der Galaxienfarben und die Beziehung zwischen Farbe und Morphologie reproduzieren.

Contents

Contents	viii
List of abbreviations	ix
I Context and theoretical background	1
1 Overview	3
2 Structure formation	7
2.1 Λ CDM cosmology	7
2.2 Linear regime	12
2.3 Zeldovich Approximation	14
3 Properties of galaxies	17
3.1 Dark matter haloes	17
3.2 Galaxy bimodality	19
3.3 Main sequence of star-forming galaxies	22
3.4 Stellar mass – metallicity relation	24
4 Supermassive black holes	27
4.1 Black holes’ properties	28
4.2 Supermassive black hole formation	29
4.3 Growth of supermassive black holes	30
4.4 Accretion discs	31
4.5 Black hole demographics	33
4.6 Impact of supermassive black holes on host galaxies	34

CONTENTS

5	Simulations of galaxy formation	35
5.1	Gravitational forces	36
5.2	Gas magneto-hydrodynamics	37
5.3	Radiative cooling processes	40
5.4	Star formation and stellar winds	41
5.5	Chemical evolution	44
5.6	Simulations	44
II	Evolution of star formation and metallicity in galaxy mergers	45
6	Merger-induced metallicity dilution in simulations	47
6.1	Introduction	47
6.2	Simulations and sample selection	49
6.2.1	Auriga simulations	49
6.2.2	Definition of the merger sample	50
6.2.3	A sample of isolated galaxies	51
6.2.4	Physics model	51
6.3	Metallicity dilution and starburst properties	53
6.3.1	Time evolution	54
6.3.2	Correlations	57
6.3.3	Projected distance	60
6.4	Mergers and the Fundamental Metallicity relation	62
6.4.1	Distribution of mergers	64
6.4.2	Evolution of mergers: stacked profiles	65
6.5	Discussion	68
6.6	Conclusion	69
7	Merger-induced metallicity dilution in SDSS galaxies	71
7.1	Introduction	71
7.2	Sample selection	73
7.2.1	Galaxy sample	73
7.2.2	Pair sample	75
7.2.3	Post-merger sample	75
7.2.4	Control samples	76

7.3	Data Analysis	79
7.3.1	Fundamental metallicity relation	79
7.3.2	Metallicity dilution and SF enhancement	82
7.3.3	Stellar mass ratio dependence	86
7.3.4	Environmental effects	87
7.4	Discussion	91
7.5	Conclusions	92
III Modelling supermassive black holes in a cosmological context		93
8 Spin evolution of supermassive Black Holes		95
8.1	Introduction	95
8.2	Spin evolution of Black Holes	98
8.2.1	Gas accretion	98
8.2.2	Coalescence of BH binaries	106
8.3	Black Hole model	109
8.3.1	Fiducial model	109
8.3.2	Self gravity in the accretion disc as a switch of BH kinetic feedback	113
8.4	Numerical Set-up	116
8.4.1	Simulation Code	116
8.4.2	Numerical implementation of spin evolution	117
8.4.3	Simulation set	119
8.5	Black hole spin in cosmological simulations	120
8.5.1	Individual histories	120
8.5.2	Black Hole demographics	123
8.5.3	Galaxy mergers and BH binary coalescence	127
8.6	Black hole spin and feedback	133
8.7	Summary and Conclusions	135
IV Conclusions and outlook		141
9 Gas metallicity and star formation in galaxy mergers		143
10 Spin evolution of supermassive black holes		145

CONTENTS

List of publications	149
Bibliography	151
Acknowledgements	168

List of abbreviations

ADAF	advection dominated accretion flow
AGB	asymptotic giant branch
AGN	active galactic nucleus
BHL	Bondi-Hoyle-Lyttleton
BLR	broad-line emission region
CMB	cosmic microwave background radiation
cSFRD	cosmic star formation rate density
ETG	early-type galaxies
FLRW	Friedmann-Lemaitre-Robertson-Walker
FMR	fundamental metallicity relation
ISCO	innermost stable circular orbit
IMF	initial mass function
ISM	interstellar medium
LISA	laser interferometer antenna
LTG	late-type galaxies
LSS	large scale structure
MHD	magnetohydrodynamics
QBLM	quasar bolometric luminosity function
SDSS	sloan digital sky survey
SFR	star formation rate
SMBH	supermassive black hole
sSFR	specific star formation rate
SSP	single stellar population
UV	ultraviolet

Part I

Context and theoretical background

Overview

In the widely-accepted standard paradigm of the big bang cosmology, lambda cold dark matter (Λ CDM), the early Universe is in a very compact, homogeneous and hot state. Very shortly after the big bang ($t \sim 10^{-36}$ seconds), the Universe enters a period of extremely accelerated expansion driven by a process called inflation (Guth, 1981; Linde, 1982; Albrecht & Steinhardt, 1982). The inflationary hypothesis provides a sensible explanation to the high homogeneity and isotropy seen in the Universe at the recombination epoch, 378 000 years after the big bang (redshift $z \sim 1100$), even at separations that became casually disconnected before this time.

During the recombination epoch, the Universe has cooled down enough for electrons to become bound to nucleons and form neutral hydrogen atoms. In this way, baryonic matter becomes optically thin to the radiation field, giving thus rise to the cosmic microwave background radiation (CMB) (Penzias & Wilson, 1965; Dicke et al., 1965). This radiation field has a highly uniform black-body spectrum with an average temperature of $\bar{T} = 2.72548$ K and small fluctuations of $\delta T/\bar{T} \sim 10^{-5}$ (Planck Collaboration et al., 2016). Considering that before recombination, the baryonic content of the Universe was coupled to the photons via Thomson scattering, the matter field should also exhibit small fluctuations of the same magnitude, i.e. $\delta\rho/\bar{\rho} \sim 10^{-5}$. These fluctuations originated in quantum fluctuations amplified during the inflationary period. After recombination, the growth rate of baryonic fluctuations is, however, not rapid enough by itself to account for the large structures observed in the

1. OVERVIEW

local Universe, requiring thus the introduction of a second type of matter¹, i.e. dark matter.

By definition, dark matter has a non-baryonic nature, i.e. it interacts with the background radiation field and with itself merely through gravitation. This feature enables the growth of dark matter fluctuations before recombination and thus, the formation of the first dark matter haloes. Historically, two different theories of dark matter have rivalised, namely: hot dark matter, in which relativistic light particles are the fundamental components; and cold dark matter, in which the non-baryonic content is composed of much heavier non-relativistic particles. Hot dark matter predicts that very massive structures form first, e.g. clusters and large galaxies, and then, through fragmentation, smaller structures are subsequently produced. Cold dark matter favours instead the formation of small structures first as the heavy fundamental dark matter particles have low streaming velocities. More massive structures form later on through a hierarchical assembly process in which less massive objects are continuously merging (Fall & Efstathiou, 1980; Blumenthal et al., 1984; Davis et al., 1985). The predicted early massive structures in the hot dark matter scenario should leave an observable imprint on the CMB; this is however not seen even in the most accurate CMB measurements (Smoot et al., 1992; Spergel et al., 2003; Planck Collaboration et al., 2011). Cold dark matter becomes thus the favoured scenario of structure formation.

The first dark matter haloes that formed before recombination provide the potential wells into which primordial gas gravitationally collapses after recombination. Through radiative cooling, gas collapses and forms the first generation of stars, giving thus rise to the first galaxies in the Universe (White & Rees, 1978). Through stellar evolution, this population of first stars produces heavy elements that are later on deposited into the surrounding gas via supernovae driven outflows and stellar winds. The metal-enriched gas of the interstellar medium (ISM) can further cool down and engender new generations of stars. This cycle keeps going on throughout the whole extension of the galaxy, leading thus to the secular evolution of the ISM, the stellar population and, ultimately, the galaxy itself (Mo et al., 2010).

In addition to the stellar, gas and dark matter contents, virtually all galaxies in the local Universe also host a supermassive black hole (SMBH) at their centres (Greene et al., 2010). SMBHs of masses above $10^9 M_{\odot}$ are already present at very early times, approximately 1 Gyr after the big bang ($z > 6.5$) (Bañados et al., 2016; Mazzucchelli et al., 2017), thereby indicating that SMBHs are an ubiquitous feature of primary galaxies as well. Although

¹Historically, the concept of dark matter was introduced to account for the velocity dispersion of galaxies in clusters (Zwicky, 1933), and the relatively flat rotation curves in spiral galaxies (Rubin et al., 1980).

the relatively rapid formation of SMBHs remains poorly understood and poses one of the biggest challenges to the current paradigm of structure formation, it is known that much of their mass is accumulated through gas accretion in the form of a surrounding accretion disc during the active galactic nuclei (AGN) phase (Softan, 1982). The gas accretion process is accompanied by a substantial release of energy that is most dramatically seen in the emission of powerful quasars (Lynden-Bell, 1969). This large amount of energy is able to drive strong outflows of hot gas (McCarthy et al., 2007; Puchwein et al., 2008), and quench star formation activity in massive galaxies, thereby showing that SMBHs play an important role in the galaxy formation process (Kauffmann & Haehnelt, 2000). On the other hand, the galaxy accretion history affects SMBH growth as the central gas reservoir needs to be replenished in order to sustain gas accretion onto black holes. Furthermore, SMBH mergers, which are expected to occur as a natural consequence of galaxy mergers, significantly contribute to the mass budget of SMBHs of masses $M_{\text{bh}} \gtrsim 10^8 M_{\odot}$ (Weinberger et al., 2018). The above suggests a co-evolution scenario between galaxies and SMBHs. This is further supported by the discovery of tight scaling relations between galaxy properties and the masses of SMBHs (Magorrian et al., 1998; Ferrarese & Merritt, 2000; Häring & Rix, 2004).

In the hierarchical galaxy assembly scenario, galaxies are constantly interacting and merging to form more massive galaxies (Fall & Efstathiou, 1980; Blumenthal et al., 1984; Davis et al., 1985). As opposed to the more quiescent secular evolution of individual galaxies, merging galaxies often experience significant changes in their properties, e.g. galaxies with discy morphologies are drastically transformed as a result of gravitational torques moving stars from ordered rotational orbits to chaotic orbits that form spheroidal remnants (Toomre, 1977; Butcher & Oemler, 1984; Dressler et al., 1997); strong gas inflows caused by dynamical instabilities can enhance gas accretion onto the central SMBH and therefore activate it (AGN phase), trigger strong bursts of star formation (Hernquist, 1989), and dilute the central gas metallicity (Ellison et al., 2008b; Scudder et al., 2012; Bustamante et al., 2018). In this thesis, we investigate two major aspects in the context of galaxy formation that are directly related to galaxy mergers. First, interacting galaxies exhibit a significant enhancement of their star formation rate (SFR) and a dilution of gas metallicity, constituting thus a well differentiated galaxy population when compared to non-interacting galaxies. Second, SMBHs grow their mass and acquire angular momentum (black hole spin) through gas accretion and mergers with other SMBHs. The evolution of these quantities and their impact on galaxy properties are expected to be different in merging and in non-interacting galaxies.

1. OVERVIEW

We structure the thesis in four main parts: Part I contains the context of this study and the theoretical background, Part II contains the first major topic on SFR enhancement and metallicity dilution, Part III contains the second major topic on black hole spin evolution, and finally Part IV contains the conclusions and an outlook of the main findings. Part I comprises 6 chapters, from chapter 1 to chapter 5. Chapter 1 corresponds to this overview. In chapter 2, we review the basic framework of the Λ CDM cosmology and galaxy formation in the Universe. We give a brief introduction into the different properties of galaxies and SMBHs in chapters 3 and 4, respectively. Finally, in chapter 5 we present a broad summary of simulation techniques used in computational astrophysics, particularly in the context of galaxy formation simulations and sub-grid modelling. Part II comprises chapter 6, in which we study the processes of SFR enhancement and metallicity dilution in merging galaxies with zoom-in simulations of galaxy formation; and chapter 7, in which we repeat the same study on observed galaxy pairs of the Sloan Digital Sky Survey (SDSS). Part III comprises chapter 8, in which we present a theoretical model of black hole spin evolution, as well as its numerical implementation and the results. We conclude in Part IV, in which we summarise the findings presented in Part II and Part III in chapters 9 and 10, respectively.

Structure formation

Our current standard paradigm of structure formation in the Universe encompasses and links many theories that describe different phenomena over a vast range of dynamical scales. At the largest scales of the Universe, the Λ CDM cosmology accounts for the evolution of the homogeneous and isotropic space-time. During the first stages of structure formation, the cosmological linear theory describes the evolution of the matter perturbations that later on give rise to the first galaxies. At the onset of the non-linear regime, during the so-called quasi-linear regime, the Zeldovich approximation provides a way to compute the velocity and position fields of the perturbations, which serve as initial condition in simulations of galaxy formation. In this chapter, we briefly outline each of these aspects. We refer the reader to the books of [Padmanabhan \(1995\)](#), [Longair \(2008\)](#) and [Mo et al. \(2010\)](#) for more in-depth details.

2.1 Λ CDM cosmology

The two main pillars of the Λ CDM cosmology are the cosmological principle (e.g. [Carroll & Ostlie, 2006](#)) and the theory of general relativity ([Einstein, 1916](#)). The cosmological principle establishes the notion that our position in the Universe is not privileged with respect to any other position. This picture is supported by observations of the CMB ([Smoot et al., 1992](#); [Spergel et al., 2003](#); [Planck Collaboration et al., 2011](#)), therefore, it can be reasonably assumed that the Universe is highly isotropic (invariant under rotations) and

2. STRUCTURE FORMATION

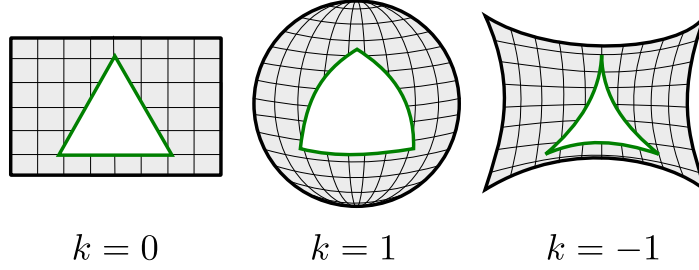


Figure 2.1: Curved spaces according to the curvature parameter. Flat geometry for $k = 0$ (left), open geometry for $k = 1$ (centre) and closed geometry for $k = -1$ (right).

homogeneous (invariant under translations) at large scales ($\gtrsim 100$ Mpc). As discussed in chapter 1, primordial perturbations can grow and eventually form galaxies, which are inherently non-homogeneous and non-isotropic features in the matter field, breaking thus the above assumption at smaller scales. Different theoretical treatments have to be, therefore, adopted for studying the large-scale and small-scale Universe. We devote this section to the description of the large-scale Universe.

The theory of general relativity provides the mathematical framework to describe the geometry of the Universe and link it to the content of matter and energy through gravity. The mathematical description of a curved space-time is given by a manifold in which distances are determined by a metric tensor $g_{\mu\nu}$ (e.g. [Carroll & Ostlie, 2006](#)). The invariant line element ds can be expressed as:

$$ds^2 = g_{\mu\nu} dx^\mu dx^\nu, \quad (2.1)$$

where dx^μ and dx^ν ($\mu, \nu = 0, 1, 2, 3$) are contravariant infinitesimal displacement four-vectors and $dx^0 \equiv cdt$, with c being the constant speed of light in vacuum. Einstein summation notation is adopted, i.e. contravariant and covariant quantities with the same index represent a summation. Given the invariant nature of the line element, i.e. it does not depend on the adopted coordinate system, the distance between two points can be computed by integrating the different line elements that connect them.

In order to derive the components of the metric tensor, we consider the condition of isotropy of the Universe, which enforces that the components connecting two different spatial coordinates vanish, i.e. $g_{ij} = 0$ for $i \neq j$ and $i, j = 1, 2, 3$. Likewise, components connecting spatial coordinates with the time coordinate should also vanish as, otherwise, a preferred direction in space will have a different evolution than the others. Under these conditions, a

convenient way to express the metric is the following:

$$ds^2 = -c^2 dt^2 + a^2(t) \left[\frac{dr^2}{1 - kr^2} + r^2(d\theta^2 + \sin^2 \theta d\phi^2) \right], \quad (2.2)$$

where $a(t)$ is the scale factor that determines the isotropic expansion of the whole Universe as a function of time, (r, ϕ, θ) are the spherical coordinates, and k is the curvature parameter that quantifies the geometry of the Universe, e.g. $k = 0$, $k = -1$ and $k = 1$ correspond to a flat, closed and open universe, respectively (see Figure 2.1). Defining the *eigentime* τ of a point as the elapsed time in the rest-frame of that point, i.e. $ds^2 \equiv -c^2 d\tau^2$, and considering that in such a configuration, the system time t coincides with τ , we conclude that $g_{00} = -1$. The tensor metric is then given by:

$$g_{\mu\nu} = \text{diag} \left(-1, \frac{a^2(t)}{1 - kr^2}, a^2(t)r^2, a^2(t)r^2 \sin^2 \theta \right). \quad (2.3)$$

This is the so-called Friedmann-Lemaitre-Robertson-Walker (FLRW) metric and is the basis for solving the Einstein field equation. As mentioned above, the theory of general relativity links the geometry of the Universe, parameterised via the Einstein tensor $G_{\mu\nu}$, to the matter and energy content described by the stress-energy tensor $T_{\mu\nu}$ via the Einstein field equation:

$$G_{\mu\nu} = R_{\mu\nu} - \frac{1}{2}g_{\mu\nu}R = \frac{8\pi G T_{\mu\nu}}{c^2} - g_{\mu\nu}\Lambda, \quad (2.4)$$

where G is the gravitational constant and Λ is the cosmological constant. The quantities $R_{\mu\nu}$ and R correspond to the Ricci tensor and Ricci scalar, respectively, and are defined as:

$$\Gamma_{\alpha\beta}^{\mu} = \frac{g^{\mu\nu}}{2} \left[\frac{\partial g_{\alpha\nu}}{\partial x^{\beta}} + \frac{\partial g_{\beta\nu}}{\partial x^{\alpha}} - \frac{\partial g_{\alpha\beta}}{\partial x^{\nu}} \right], \quad (2.5)$$

$$R_{\mu\nu} = \frac{\partial \Gamma_{\mu\nu}^{\alpha}}{\partial x^{\alpha}} - \frac{\partial \Gamma_{\mu\alpha}^{\nu}}{\partial x^{\nu}} + \Gamma_{\beta\alpha}^{\alpha} \Gamma_{\mu\nu}^{\beta} - \Gamma_{\beta\nu}^{\alpha} \Gamma_{\mu\alpha}^{\beta}, \quad (2.6)$$

$$R = g^{\mu\nu} R_{\mu\nu}. \quad (2.7)$$

Approximating the behaviour at large-scales of the different components of the Universe

2. STRUCTURE FORMATION

Property	Density	Pressure	Temperature
Matter (baryonic + dark)	$\rho = \rho_{m0}a^{-3}(t)$	$P = P_{m0}a^{-5}(t)$	$T = T_{m0}a^{-2}(t)$
Radiation (+ relativistic matter)	$\rho = \rho_{r0}a^{-4}(t)$	$P = P_{r0}a^{-4}(t)$	$T = T_{r0}a^{-1}(t)$
Vacuum	$\rho = \rho_{\Lambda 0}$	$P = P_{\Lambda 0} = -\rho_{\Lambda 0}c^2$	—

Table 2.1: Functions of density, pressure and temperature for different components of the Universe in terms of the scale factor $a(t)$ (Longair, 2008). Reference values ρ_0 , P_0 and T_0 correspond to values at the current time t_0 , at which, by convention, $a_0 = a(t_0) = 1$.

as to an ideal fluid, the stress-energy tensor for each component can be written as:

$$T_{\mu\nu} = \left(\rho + \frac{P}{c^2} \right) v_\mu v_\nu + P g_{\mu\nu}, \quad (2.8)$$

with P denoting the pressure, ρ the density and v the velocity of the fluid. By combining the previous equations for the FLRW metric, the Einstein tensor and the stress-energy tensor, the Einstein field equation can be readily solved, yielding thus the Friedmann equations (Friedmann, 1922):

$$\begin{aligned} \left(\frac{\dot{a}}{a} \right)^2 &= \frac{8\pi G}{3} \rho - \frac{kc^2}{a^2} + \frac{\Lambda c^2}{3}, \\ \left(\frac{\ddot{a}}{a} \right) &= -\frac{4\pi G}{3} \left(\rho + \frac{3p}{c^2} \right) + \frac{\Lambda c^2}{3}. \end{aligned} \quad (2.9)$$

In order to solve this system of equations for the scale factor $a(t)$, it is necessary to determine the explicit time-dependence of the density ρ and the pressure P for each component of the Universe¹. Detailed derivations of the time-dependent functions can be found in the book of Longair (2008). We simply list them in Table 2.1.

We define the Hubble parameter $H(t)$ as the normalised derivative of the scale factor:

$$H(t) \equiv \frac{\dot{a}}{a}. \quad (2.10)$$

¹Note that these quantities can only depend on time, as otherwise, the assumption of an isotropic universe would be violated.

Note that at the current time, $H(t_0) = H_0$ corresponds to the expansion rate of the local Universe, which is the proportionality constant in Hubble's law (Hubble, 1929):

$$cz = H_0 d, \quad (2.11)$$

where d is the physical distance from an observer (e.g. Earth) to a distant source, and z is the cosmological redshift that measures the Doppler shift in wavelength that light undergoes while travelling from the distant source to the observer. The redshift can be related to the scale factor as:

$$a(t) = \frac{1}{1+z}. \quad (2.12)$$

We define the present-day density parameters of matter, radiation and vacuum energy as:

$$\Omega_m \equiv \frac{\rho_{m0}}{\rho_c}, \quad (2.13)$$

$$\Omega_r \equiv \frac{\rho_{r0}}{\rho_c}, \quad (2.14)$$

$$\Omega_\Lambda \equiv \frac{\Lambda}{3H_0^2}, \quad (2.15)$$

$$\Omega_0 \equiv \Omega_r + \Omega_m + \Omega_\Lambda, \quad (2.16)$$

$$\rho_c \equiv \frac{3H_0^2}{8\pi G}, \quad (2.17)$$

where ρ_c is the reference critical density and is defined as the density in a static ($\Lambda = 0$), flat ($k = 0$) universe.

Making use of the previous definitions, the system of equations (2.9) can be finally rewritten in the following form:

$$H^2(t) = H_0^2 [\Omega_r(1+z)^4 + \Omega_m(1+z)^3 + (1-\Omega_0)(1+z)^2 + \Omega_\Lambda]. \quad (2.18)$$

The most recent measurements of the cosmological parameters are (Planck Collaboration et al., 2018): $H_0 = 67.4 \pm 0.5 \text{ s}^{-1} \text{ Mpc}^{-1} \text{ km}$, $\Omega_m = 0.315 \pm 0.007$, $\Omega_\Lambda = 0.692 \pm 0.012$, $\Omega_r \approx 0$ and $\Omega_0 \approx 1$. According to these values, our present-day Universe is spatially flat and is dominated by the cosmological constant that causes an accelerated expansion. In analogy with the positive pressure exerted by the matter and radiation content of the Universe, if the cosmological constant is associated to a hypothetical energy field, the corresponding pressure will be negative (see Table 2.1). This energy is often referred to as dark energy

2. STRUCTURE FORMATION

(Riess et al., 1998). The content of non-relativistic matter is in turn divided into a baryonic component and a non-baryonic component. The latter corresponds to the already-discussed cold dark matter and accounts for 84.2% of the total matter content. Baryonic matter only amounts for 15.8%, playing thus a comparatively weaker role in the evolution of the large-scale Universe. Nevertheless, the rich and complex plethora of interactions exhibited by baryonic matter makes it the most relevant and interesting component at small scales.

2.2 Linear regime

In the previous section, we described the large-scale Universe under the assumptions of isotropy and homogeneity. As discussed in chapter 1, these assumptions do no longer hold at smaller scales owing to the growth of matter fluctuations and subsequent structure formation. Nevertheless, it is still possible to describe the evolution of the early Universe at the smaller scales by treating the growing fluctuations as small perturbations of the homogeneous and isotropic solution. This is the so-called linear regime of structure formation. In order to adopt this approach, some assumptions have to be made first, namely: the different modes of the matter field evolve independently from each other, i.e. they are linearly independent; density fluctuations are very small with respect to the background density $\delta\rho \ll \bar{\rho}$; and the characteristic physical size of the perturbations is smaller than the Hubble radius¹ $r_\delta \ll r_H \sim cH_0^{-1}$. The last assumption allows us to neglect relativistic effects of the curvature of the space-time and therefore, use a Newtonian framework to describe the evolution of the perturbations.

For the sake of convenience, we define the comoving distance to an object \mathbf{r} as:

$$\mathbf{r} \equiv \frac{\mathbf{x}}{a}, \quad (2.19)$$

where \mathbf{x} is the proper distance and a is the time-dependent scale factor. In this new coordinate system, the expansion of the Universe is factored out, and therefore, the comoving distance between two fixed comoving points is always constant. This definition has an interesting consequence when the proper velocity \mathbf{u} is calculated:

$$\begin{aligned} \mathbf{u} \equiv \frac{d\mathbf{x}}{dt} &= \dot{a}\mathbf{r} + a\frac{d\mathbf{r}}{dt} \\ &= H\mathbf{x} + \mathbf{v} \end{aligned} \quad (2.20)$$

¹The Hubble radius r_H is a length scale that approximates the radius of the observable Universe.

with

$$\mathbf{v} \equiv a \frac{d\mathbf{r}}{dt}. \quad (2.21)$$

The second term in the right-hand side in equation (2.20) is dubbed peculiar velocity and refers to the velocity of an object relative to the rest frame in which the expansion is isotropic and homogeneous. An object that is static in this frame, i.e. $\mathbf{v} = 0$, has still a non-vanishing proper velocity as the first term prevails. That term represents the recessional velocity that is caused solely by the expansion of the Universe. At the present-day Universe, this corresponds to Hubble's law, which was presented before in equation (2.11).

Previously, we have approximated the behaviour of the matter as an ideal gas. Under this assumption, the classical equations of fluid dynamics along with the equation of state of an ideal gas can be employed to describe the evolution of the fluctuations (Longair, 2008):

$$\begin{array}{l} \text{Continuity} \\ \text{equation} \end{array} \quad \frac{\partial \delta}{\partial t} = -\frac{1}{a} \nabla_r \cdot [(1 + \delta)\mathbf{v}], \quad (2.22)$$

$$\begin{array}{l} \text{Euler's} \\ \text{equation} \end{array} \quad \frac{\partial \mathbf{v}}{\partial t} + \frac{\dot{a}}{a} \mathbf{v} + \frac{1}{a} (\mathbf{v} \cdot \nabla_r) \mathbf{v} = -\frac{\nabla_r P}{a\bar{\rho}(1 + \delta)} - \frac{1}{a} \nabla_r \Phi, \quad (2.23)$$

$$\begin{array}{l} \text{Poisson's} \\ \text{equation} \end{array} \quad \nabla_r^2 \Phi = 4\pi G \bar{\rho} a^2 \delta, \quad (2.24)$$

$$\begin{array}{l} \text{Equation} \\ \text{of state} \end{array} \quad \nabla_r P = c_s^2 \bar{\rho} \Delta \delta + \frac{2}{3} \bar{T} \rho \Delta s, \quad (2.25)$$

where δ is the density parameter, defined by $\rho = \bar{\rho} + \delta\rho = \bar{\rho}(1 + \delta)$; \mathbf{v} is the peculiar velocity; P is the gas pressure; Φ is the peculiar gravitational potential; c_s is the speed of the sound; \bar{T} is the mean temperature of the gas; and s is the specific entropy. Note that all the equations are expressed in comoving coordinates, as in this way, the expansion of the space-time is factored out and the treatment of the fluctuations is purely Newtonian.

We combine the previous set of equations to obtain the following differential equation for the density parameter:

$$\frac{\partial^2 \delta}{\partial t^2} + 2\frac{\dot{a}}{a} \frac{\partial \delta}{\partial t} = 4\pi G \bar{\rho} \delta + \frac{c_s^2}{2} \nabla^2 \delta + \frac{2}{3} \frac{\bar{T}}{a^2} \nabla^2 s. \quad (2.26)$$

In the linear regime, the density field can be decomposed into a set of orthogonal modes. For the case of a flat universe, i.e. $k = 0$, the orthogonal base corresponds to sinusoidal

2. STRUCTURE FORMATION

functions. The density parameter can be therefore expressed in the following form:

$$\delta(\mathbf{r}, t) = \int \delta_{\mathbf{k}} e^{i\mathbf{k}\cdot\mathbf{r}} d^3\mathbf{k}, \quad (2.27)$$

where $\delta_{\mathbf{k}}$ is the amplitude of an orthogonal mode and represents the Fourier transform of the density field. The equation that describes the evolution of $\delta_{\mathbf{k}}$ is then given by:

$$\frac{d^2\delta_{\mathbf{k}}}{dt^2} + 2\frac{\dot{a}}{a}\frac{d\delta_{\mathbf{k}}}{dt} = \left[4\pi G\bar{\rho} - \frac{c_s^2}{a^2}k^2 \right] \delta_{\mathbf{k}}. \quad (2.28)$$

By inserting the Friedmann equations (2.9), the previous equation can be solved for each mode $\delta_{\mathbf{k}}(t)$ of the density field. Initial conditions are provided by the power spectrum, which describes the distribution of power into each mode of the field. An initial power spectrum for matter fluctuations that is motivated by inflation theories is (Guth, 1981; Linde, 1982):

$$P(k) \propto k^{n_s-1}, \quad (2.29)$$

where n_s is the spectral index and one of the cosmological parameters. Its measured value is $n_s \sim 1$ (Planck Collaboration et al., 2018), which implies a flat power spectrum.

An analogous procedure can be followed for fluctuations in the radiation field and for relativistic matter. We refer the reader to the books of Padmanabhan (1995) and Longair (2008) for exhaustive details and derivations.

2.3 Zeldovich Approximation

When matter perturbations grow much larger than the background density, the stronger modes of the density field start to couple with each other as more complex interactions come to play, breaking thus the assumption of linearity and giving rise to the non-linear regime. At the onset of the non-linear regime, when perturbations do not deviate significantly from the linear solution, it is possible to describe the evolution of the perturbations in terms of the displacement field Ψ , defined by the following expression:

$$\mathbf{r}_f(t, \mathbf{q}) = a(t)\mathbf{r} = a(t) [\mathbf{q} + \Psi(\mathbf{q}, t)], \quad (2.30)$$

where \mathbf{r}_f is the Lagrangian trajectory of a portion of fluid, \mathbf{r} is its comoving position at the time t , and \mathbf{q} corresponds to the initial Lagrangian coordinate of the fluid element when the

medium is unperturbed. The position and velocity fields of the perturbations can be solved in terms of Ψ . This is the so-called Zeldovich approximation (Zeldovich, 1970).

From equation (2.27) for the evolution of the density parameter, it is possible to demonstrate that the displacement field satisfies (Yoshisato et al., 2006):

$$\frac{\partial^2 \Psi}{\partial t^2} + 2H \frac{\partial \Psi}{\partial t} = \frac{3}{2} H^2 \Psi, \quad (2.31)$$

$$\Psi = \frac{3}{2} H_0^{-2} a(t) \nabla \Phi, \quad (2.32)$$

where Φ is the peculiar gravitational potential, which can be solved by integrating Poisson's equation (2.24). To this end, it is convenient to express the principle of mass conservation in terms of the initial Lagrangian coordinates:

$$\rho(\mathbf{r}, t) d^3 \mathbf{r} = \bar{\rho}(t) d^3 \mathbf{q}. \quad (2.33)$$

From the the Jacobian $\partial q_i / \partial r_j$ of the transformation $\mathbf{r} \rightarrow \mathbf{q}$, the perturbed density field can be rewritten as (Padmanabhan, 1995):

$$\rho(\mathbf{r}, t) = \frac{\bar{\rho}(t)}{(1 - a(t)\lambda_1(\mathbf{q})) (1 - a(t)\lambda_2(\mathbf{q})) (1 - a(t)\lambda_3(\mathbf{q}))}, \quad (2.34)$$

where $-\lambda_i(\mathbf{q})$ are the eigenvalues of the Jacobian and are sorted such that $\lambda_1 \geq \lambda_2 \geq \lambda_3$. These eigenvalues can be interpreted in a geometrical way, i.e., as indicators of the local collapse or expansion of the fluid into the direction of the corresponding eigenvector; thus, for example, if $\lambda_i > 0$, the fluid is collapsing locally into the direction of the eigenvector \mathbf{u}_i , whereas if $\lambda_i < 0$, it is expanding into the same direction. The Zeldovich approximation is widely used in cosmological simulations because it allows to construct the position and velocity fields of the perturbations, which serve as initial conditions in particle-based numerical techniques to solve the problem of structure formation in the Universe.

Properties of galaxies

Although galaxies are the fundamental units of structure in the Universe, they are complex and rich systems that harbour many different physical phenomena. As mentioned in chapter 1, dark matter perturbations can grow before recombination due to the absence of radiative pressure, allowing much higher density anisotropies of the dark matter component relative to that of the baryons, and giving thus rise to the dark matter haloes. These haloes provide the potential wells into which primordial gas collapses after recombination, forming thus the first galaxies. Through radiative cooling, the gas can further collapse and form the first population of stars, which later on deposit heavy elements into the ISM via supernovae outflows and stellar winds. New stellar populations are born and the cycle is repeated, resulting in an overall evolution of the galaxy properties. In this chapter, we present some important properties and relations of galaxy populations, namely: properties of the dark matter haloes, the bimodality in galaxy structure and colour, the main sequence of star-forming galaxies and the mass-metallicity relation.

3.1 Dark matter haloes

Perturbations of the dark matter field that reach and exceed a certain threshold value in the resulting overdensity relative to the background density undergo a spherical collapse into virialised structures known as dark matter haloes. They are characterised by the virial radius r_{200} , the radius of a region in which the average density is 200 times the cosmic background

3. PROPERTIES OF GALAXIES

density; and the virial mass M_{vir} , which is the total mass enclosed within r_{200} . Additionally, dark matter haloes acquire angular momentum through tidal torques, which endows them with centrifugal support (Hoyle, 1951; Peebles, 1969; White, 1984) and shapes their inner structure. The angular momentum is quantified by the dimensionless spin parameter λ , which indicates the specific angular momentum of the halo normalised by the theoretical maximum.

The radial structure of dark matter haloes has been found to be universal and independent of mass (Navarro et al., 1997), and is given by:

$$\rho(r) = \frac{\rho_0}{(r/r_s)(1 + r/r_s)^2}, \quad (3.1)$$

where ρ_0 is the density at the centre of the halo; and r_s is the scale radius, which is related to the virial radius via $r_s = r_{200}/c$, where c is the concentration parameter.

Once dark matter halos have formed, they provide the potential wells into which primordial gas gravitationally collapses through the filamentary cosmic web structure. Infalling gas is shock-heated as it encounters a settled medium inside the halo, thereby reaching high virial temperatures $T \sim 10^6$ K (Rees & Ostriker, 1977). After this point, radiative processes drive the cooling of the gas, which causes it to segregate from the dark matter and subsequently settle down into a centrifugally supported disc structure (Fall & Efstathiou, 1980; Mo et al., 1998), giving thus rise to the ISM and enabling the star formation processes (White & Rees, 1978). The details of gas accretion and cooling are strongly dependent on the properties of the dark matter haloes. For instance, small haloes with masses $M_{\text{vir}} \leq 10^{12} M_{\odot}$ also accrete gas via cold streams along the filaments of the cosmic web. In this scenario, cold gas can penetrate deep into the halo and avoids being shock-heated. For more massive haloes, the cold accretion mode is suppressed by shock-heating and hot accretion becomes dominant, causing radiative cooling to play a critical role in the gas settling (Silk, 1977; Rees & Ostriker, 1977; Kereš et al., 2005; Dekel & Birnboim, 2006). Galaxy properties are therefore expected to correlate with the properties of the dark matter haloes (Mo et al., 1998):

In addition to the above mentioned processes of gas accretion and cooling, and the formation of the disc structure, there are other crucial and complex processes that have an important influence on galaxy evolution. For example, the feedback from star formation can balance and overcome the cooling process by injecting heat into the galactic and extra-galactic gas via stellar winds and supernovae driven outflows. The feedback from supermassive

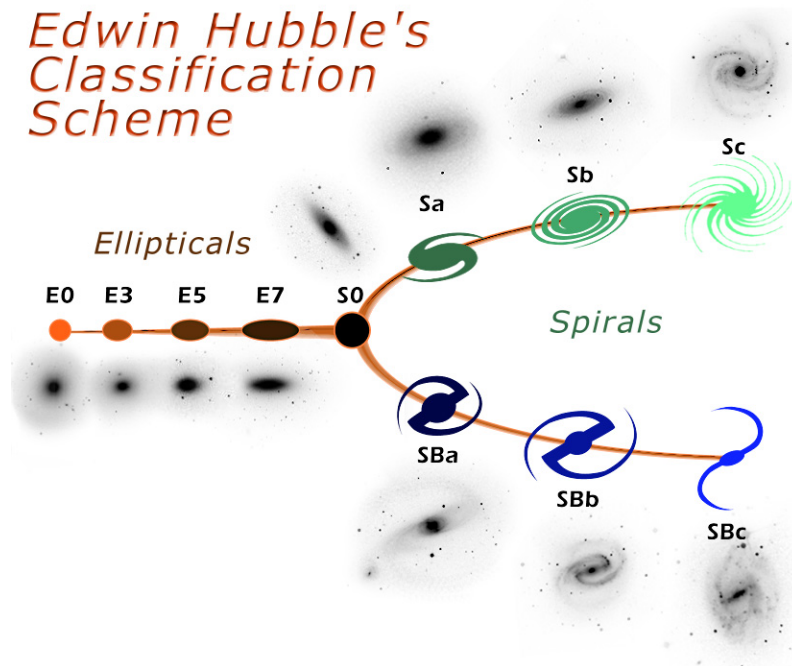


Figure 3.1: The Hubble classification scheme of galaxies. Image credits: https://en.wikipedia.org/wiki/Hubble_sequence#/media/File:HubbleTuningFork.jpg.

black holes that form at the centre of galaxies can drive very powerful gas outflows if there is a gas reservoir that can sustain a continuous accretion (Lynden-Bell, 1969; McCarthy et al., 2007; Puchwein et al., 2008). Feedback processes result in most cases in a shutting down of star formation activity by either expelling or heating up the gas, thereby impacting directly the stellar and the gas distributions of galaxies. Moreover, internal secular processes and galaxy mergers can significantly redistribute the baryon content inside galaxies, leading thus to a large variety of galaxy morphologies.

Thus, in order to understand the build-up history of galaxies in the context of galaxy formation, it is important to determine the baryonic structure and the processes that shape it.

3.2 Galaxy bimodality

Observations of local galaxies have revealed a clear bimodality in several galaxy properties. This was first evinced by Hubble (1926) in the form of a bimodality in the morphology of the population of local galaxies. In this pioneering work, Hubble devised a classification scheme in which galaxies are separated into ellipticals (so-called early-type galaxies, ETGs)

3. PROPERTIES OF GALAXIES

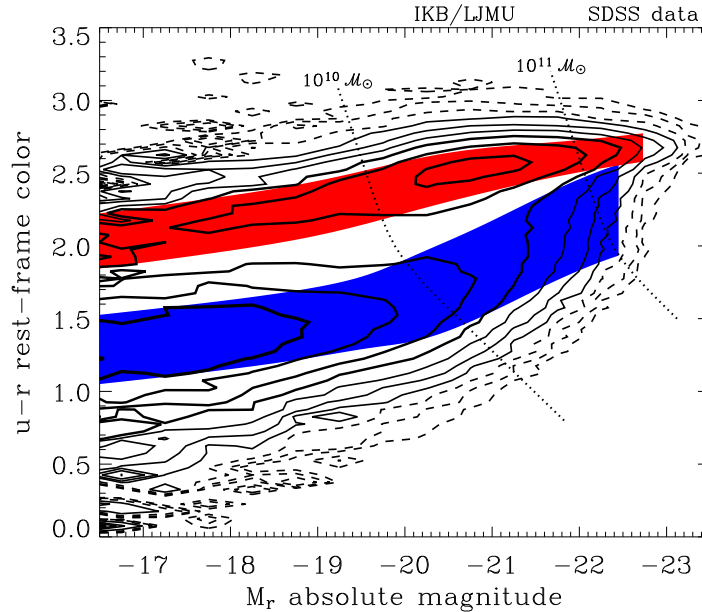


Figure 3.2: Colour-magnitude distribution of local galaxies from the SDSS ($z < 0.1$). The bimodality of the distribution is reflected in the two peaks in galaxy colour, which are associated to the red and blue sequences (shaded regions) (Baldry et al., 2004). Image credits: <http://www.astro.ljmu.ac.uk/~ikb/bimodal-figure/>.

and into spirals (so-called late-type galaxies, LTGs). They can be seen on the right and left parts of the diagram shown in Figure 3.1, respectively.

Spiral galaxies are systems in which most of the stars and the gas move along regular circular orbits and are, therefore, concentrated in a geometrically flat disc. Galactic discs can in turn develop features like arms and bars, which are used in the Hubble diagram to subdivide spiral galaxies into different groups. For instance, the presence/absence of bars determines whether a galaxy is a *SB* (barred spiral) or a *S* (spiral) system. Likewise, the number of spiral arms and their pitch angle determine the subcategory, which is indicated by a lowercase letter: *a*, *b* or *c*. Thus, for example, *SBa* refers to a barred spiral galaxy with tightly wound arms.

On the other hand, elliptical galaxies are more spheroidal systems with a smoother appearance. The orbits of gas and stars are not regular and instead are dominated by random motion, implying thus a limited rotational support. In the Hubble diagram, they are denoted by the letter *E*, followed by a number that represents the ellipticity of the system, e.g. *E0* correspond to a fully spherical configuration, whereas *E7* to a very flat spheroid. A somewhat intermediate category is represented by lenticular galaxies, which are disc galaxies

with no spiral arms and are denoted by $S0$ in the Hubble diagram.

Recent studies in local galaxy populations have revealed a connection between the morphology bimodality and a colour bimodality, which is in turn linked to the star formation properties of galaxies (Strateva et al., 2001; Kauffmann et al., 2003; Baldry et al., 2004). Spiral galaxies exhibit substantial ongoing star formation activity due to the high amount of gas that acts as fuel (Kennicutt, 1998). As a result, short-lived massive and hot stars that emit light at short optical wavelengths are produced in high abundance and spiral galaxies display blue optical colours. In contrast, stellar populations in elliptical galaxies are often dominated by long-lived smaller and cold stars that emit light at longer optical waves, resulting in galaxies with red optical colours (Kelson et al., 2001; Bell et al., 2004). This is an indication that star formation activity shut downs on short timescales, a process also referred to as quenching. In Figure 3.2, we show the colour-magnitude distribution of local galaxies from the SDSS, in which the red (generally ETGs) and the blue (generally LTGs) sequences are identified (Baldry et al., 2004). Considering that the absolute magnitude is a measurement of the luminosity of a galaxy, which, in turn, can be related to luminous mass (Kauffmann et al., 2003), a bimodality in galaxy mass is also represented in this plot. Thus, ETGs tend to be more massive than LTGs. Finally, galaxies hosting AGNs have been shown to exhibit a bimodal distribution on the radio-optical plane, with radio-loud galaxies being about 10^3 times brighter in radio than radio-quiet galaxies (Kellermann et al., 1989; Xu et al., 1999; Sikora et al., 2007). The radio-loudness bimodality is also linked to the galaxy morphological type, with radio-loud and radio-quiet objects tending to be red massive ETGs and blue LTGs, respectively¹.

The origin of these bimodalities is currently not fully understood as the assembly of the massive red early-type galaxies is still an open question. One possible explanation might lie in the different gas accretion modes for low-mass and high-mass dark matter haloes, with the former being dominated by cold filamentary accretion, whereas the latter by spherical hot accretion (Silk, 1977; Rees & Ostriker, 1977; Kereš et al., 2005; Dekel & Birnboim, 2006). SMBH properties such as accretion rate and spin seem to have an important impact on the bimodal distribution of galaxy colour and radio-loudness as radio-loud galaxies often exhibit strong relativistic jets and AGN feedback-driven gas outflows (Wilson & Colbert, 1995; Hughes & Blandford, 2003; Jester, 2005). These processes regulate the availability of cold ISM gas for the star formation process and lead often to galaxy quenching and

¹In addition, there is an important dependence on the BH accretion rate, e.g. ETGs hosting highly accreting BHs are usually radio-quiet.

3. PROPERTIES OF GALAXIES

reddening.

3.3 Main sequence of star-forming galaxies

The collapse of baryons into dark matter haloes and the subsequent radiative cooling and settling of the gas are followed by the formation of stars. If primordial gas is cooled down sufficiently, internal processes can lead to the formation of molecules, which eases a small scale fragmentation of the gas into clouds that can gravitationally collapse after losing hydrostatic equilibrium and finally evolve into stars. The details of the collapse process strongly depend on the timescales over which the gas is able to cool down, which differ significantly between the first population of stars (so-called population III stars) and the more metal-rich population that are produced in later evolutionary stages (population I and II stars). This results in population III stars being more massive and less long-lived than present-day population I and II stars.

The overall star formation activity in the Universe evolves in time and becomes significantly high between $z \sim 1 - 4$, reaching its peak at about $z \sim 2$ (lookback time of about 10.5 Gyr), as revealed by observations of the cosmic star formation rate density (cSFRD) (see e.g. [Madau & Dickinson, 2014](#)). Furthermore, recent observational studies have shown that most of the actively star-forming galaxies follow a relation dubbed the main sequence, which links the assembled stellar content, i.e. the galaxy stellar mass M_* , with the current ongoing star formation rate (SFR) (e.g. [Noeske & et al., 2007](#); [Daddi et al., 2007](#); [Elbaz et al., 2007](#); [Whitaker et al., 2012](#)). In [Figure 3.3](#), we show the stellar mass and SFR of star-forming galaxies for different redshift ranges measured by [Whitaker et al. \(2012\)](#). These observations evince the presence of the main sequence at different cosmic times. The normalisation of the relation, which is given by the specific star formation rate (sSFR) with $\text{sSFR} = \frac{\text{SFR}}{M_*}$, is redshift-dependent due to the evolution of the cSFRD. Specifically, $\text{sSFR} \propto (1+z)^3$, as shown by [Lilly et al. \(2013a\)](#). This indicates that, at a given stellar mass, SFRs at $z = 0$ are lower by a factor of $\sim 10 - 20$ compared to those at $z = 2$; in other words, present-day galaxies are less efficient in forming stars than galaxies at $z \sim 2$. The relatively small scatter of the relation (0.2 – 0.3 dex) is interpreted as that star-forming galaxies evolve along the main sequence as they build up their stellar content, while keeping their sSFR at equilibrium. This implies the existence of different universal star formation regimes that operate at different cosmic times. Thus, galaxies at high redshifts grow their stellar content in a fast and continuous fashion. This is sustained by efficient feeding through cold accretion

3.3 Main sequence of star-forming galaxies

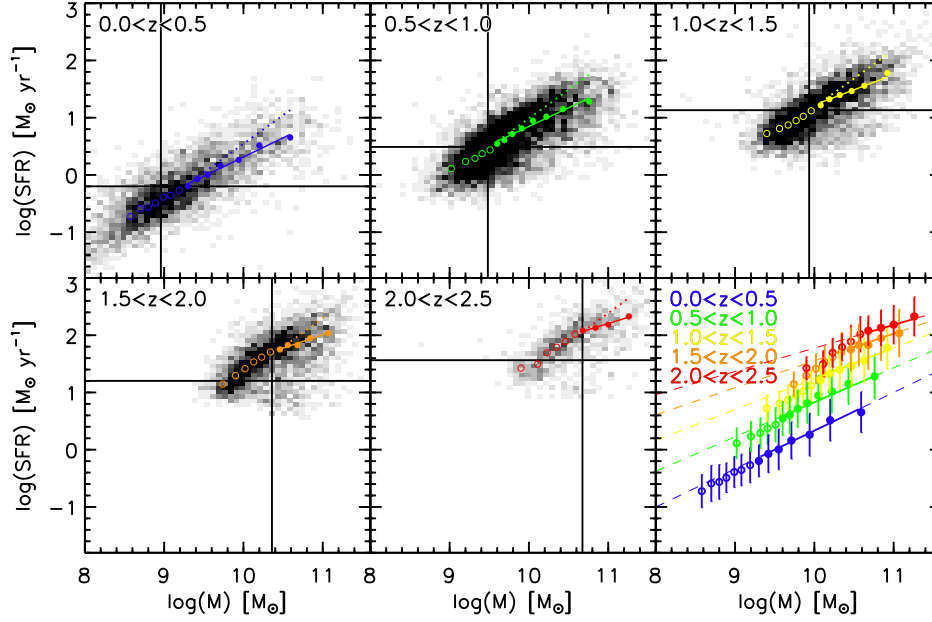


Figure 3.3: Relation between stellar mass M_* and SFR of observed galaxies. Each panel shows galaxies measured within the NEWFIRM Medium-Band survey in different redshift ranges by Whitaker et al. (2012). The symbols denote the running medians. In the bottom, right panel, vertical bars represent the scatter and dashed lines correspond to the best-fit power law to the medians. The main sequence of star-forming galaxies is ubiquitous, with only the normalisation varying in redshift. This figure is taken from Whitaker et al. (2012).

streams from the cosmic web and minor mergers. At low redshift, self-regulated feedback processes from stars and central black holes, inefficient cooling rates and gas exhaustion cause a drop in star formation efficiency, ultimately resulting in low SFRs (for a thoughtful discussion of these processes, see Schaye et al., 2010).

In addition to the population of star-forming galaxies that are closely aligned on the main sequence, there exist other populations of galaxies that are outliers in the relation. For instance, star-bursting galaxies exhibit anomalously large SFRs that are 4 – 10 times higher than main sequence counterparts. They are likely the result of transient strong interaction such as major mergers that drive gas inflows and compress the central gas, enhancing thus the star formation process (Rodighiero et al., 2011). On the other hand, the population of red sequence ETGs exhibits very low SFRs compared to main sequence galaxies as most of the star formation activity is quenched.

3.4 Stellar mass – metallicity relation

During the recombination era, when electrons become bound to nucleons, the baryonic content of the Universe is dominated by neutral hydrogen. Helium and small traces of lithium are also present as a result of primordial nucleosynthesis, which occurred about 10 – 20 s after the Big Bang. As discussed before, baryons collapse onto already-settled dark matter structures. Due to its collisional nature, the gas is heated up as the kinetic energy released during the infall is converted into thermal energy. Additionally, processes such as shock heating and photoionisation from local sources and from the ultraviolet background (UVB) can further heat up the gas. Nevertheless, in order to sustain the fragmentation and the small-scale gravitational collapse needed for forming stars, the gas has to be cooled down.

For the composition of the primordial gas, the processes that drive the cooling are two-body radiative processes, e.g. collisional excitation, collisional ionisation and standard recombination of neutral hydrogen H^0 , neutral helium He^0 and single ionised helium He^+ , dielectronic recombination of single ionised helium He^+ and free-free emission (bremsstrahlung) (Black, 1981; Cen, 1992). The subsequent gravitational collapse of the gas leads to the formation of the first generation of stars in the Universe, i.e. the population III stars. These massive stars have short lifetimes as they burn their hydrogen supply through thermonuclear fusion processes very quickly, resulting in a rapid evolution and a chemical enrichment of the stellar interior. They end up as core-collapse supernovae, releasing thus a significant amount of metal-enriched gas¹ to the surroundings.

As the chemical composition of the ISM evolves, new cooling channels become available, namely the metal-line emissions (Wiersma et al., 2009). This allows for the gas to undergo even further fragmentation, thereby preventing the formation of more population III stars, but triggering instead the formation of less massive, more long-lived, metal-rich populations I and II stars. During the evolution and final stages of these late stellar populations, the ISM is chemically enriched with heavier elements, including trans-iron elements that are only produced by supernovae.

Thus, it is theoretically predicted that the assembly of the stellar content of galaxies is accompanied by a chemical evolution of the ISM. Observations of oxygen abundances of H II (ionised atomic hydrogen) regions in local galaxies have revealed a relation between gas-phase metallicity and luminosity (Skillman et al., 1989; Zaritsky et al., 1994). This has been recently confirmed to be a manifestation of a more fundamental stellar mass –

¹In astronomy, elements other than H and He are often referred to as “metals”.

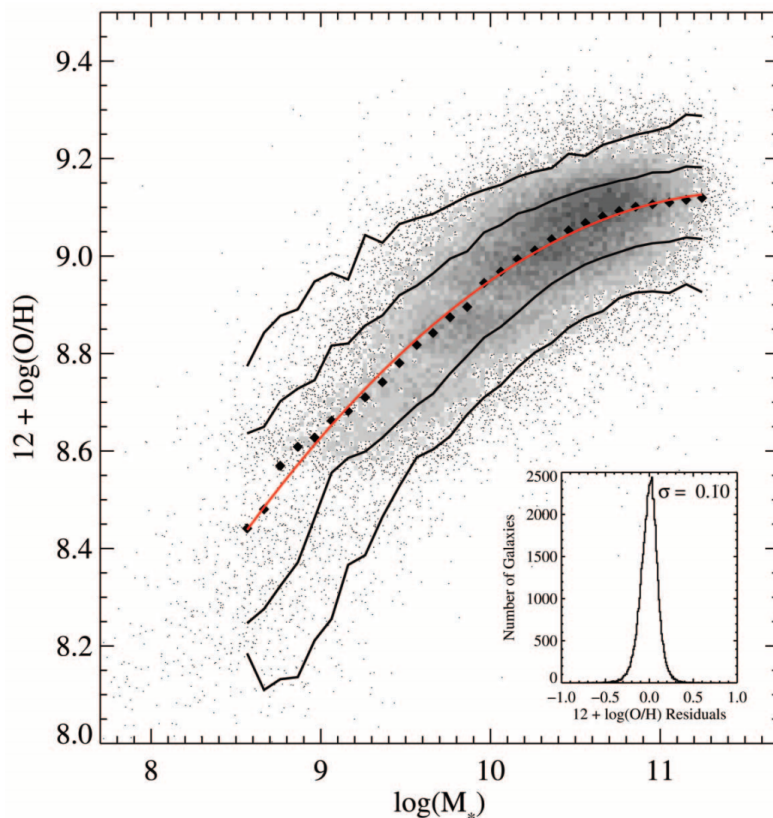


Figure 3.4: Relation between stellar mass and gas-phase oxygen abundance of star-forming galaxies in the SDSS. Diamonds correspond to medians in different mass bins. Solid lines represent the 68% and 95% percentiles. The red line is a polynomial fit to the data. This figure is taken from Tremonti et al. (2004).

metallicity relation (MZR; Lequeux et al., 1979; Tremonti et al., 2004). In Figure 3.4, we show the local MZR for star-forming galaxies of the SDSS at $z \sim 0.1$ compiled by Tremonti et al. (2004). The small scatter of the residual distribution (0.1 dex) indicates that star-forming galaxies evolve along the MZR, thereby supporting the theoretical predictions. At stellar masses above $10^{10.5} M_{\odot}$, the evolution of the gas metallicity can be treated as a “closed box model”, in which gas inflows and outflows can be neglected. Therefore, the metallicity is only controlled by gas recycling and star formation. Considering that at this range of stellar mass, AGN quenching processes start to become relevant, the relation tends to flatten. In the stellar mass range $10^{8.5} - 10^{10.5} M_{\odot}$, the relation is relatively steep due to presence of strong winds driven by supernovae and AGB stars. The winds are loaded with metals, reducing thus the gas metallicity when they leave the galaxy. This scenario can be thought as a “leaky box model”.

3. PROPERTIES OF GALAXIES

In addition to the the main dependence of the gas-phase metallicity on stellar mass, a secondary dependence on the SFR has been found in SDSS galaxies (see e.g. [Ellison et al., 2008a](#); [Mannucci et al., 2010](#)). This is encoded in the so-called fundamental metallicity relation (FMR), which shows that, at a fixed stellar mass, galaxies with higher SFRs tend to have lower metallicities. This behaviour is likely an effect of the complex interplay between accretion of pristine gas and stellar chemical enrichment. Although steadily evolving, relatively isolated star-forming galaxies are well aligned on the FMR, galaxies undergoing major and intermediate mergers have been shown to be a prominent outlier population in the relation, displaying lower-than-expected metallicities ([Mannucci et al., 2010](#); [Grønnow et al., 2015](#)). In part II of this thesis, we investigate the properties of the outlier population of interacting galaxies in both simulations and observations.

Supermassive black holes

In addition to the gas and stellar components, virtually all observed galaxies in the local Universe have been shown to host a supermassive black hole (SMBH) at their centres (Greene et al., 2010). The nature of these objects has been revealed through the analysis of stellar orbits in the Milky-Way’s galactic centre, close to the local SMBH, Sagittarius A*. The mass of Sgr A* has been measured to be around $4 \times 10^6 M_{\odot}$ and is enclosed in a relatively small sphere with a radius of at most 125 AU, which is consistent with the properties of a space-time singularity, i.e. a BH (for a review of this method, see Genzel et al., 2010). The presence of these massive objects already at $z \sim 6.5$ (Bañados et al., 2016; Mazzucchelli et al., 2017), i.e. only 1 Gyr after the Big Bang, remains an unsolved mystery in modern theories of galaxy formation. However, the discovery at high redshift of extremely luminous galaxies with very distinct spectra (the so-called quasars; Schmidt, 1963, 1968) has shed light on the assembly of SMBHs. The spectral features of quasars are consistent with the modelled emission of a fast accreting, optically thick, geometrically thin gas disc around a SMBH (Shakura & Sunyaev, 1973). Before crossing the event horizon, a significant fraction of the rest mass and potential energy of the infalling gas is radiated (Soltan, 1982), outshining in some cases the host galaxy (Lynden-Bell, 1969). This large amount of radiated energy can drive large-scale gas outflows and trigger stellar quenching in the host galaxy. The remaining gas that crosses the event horizon is ultimately accreted by the SMBH, increasing thus its mass and angular momentum. In this chapter, we discuss

4. SUPERMASSIVE BLACK HOLES

different aspects of SMBHs, namely: their properties, the different formation scenarios and growth channels, and the scaling relations with host galaxies.

4.1 Black holes' properties

Black holes are defined as regions in the space-time that exhibit such strong gravitational effects that nothing (including photons) can escape from inside a small region around them called the event horizon. The no-hair theorem postulates that BHs can be completely characterised by three classical physical properties, namely: mass, angular momentum (spin) and electrical charge (Heusler, 1996). Aside of this, BHs are featureless objects. For a thoughtful review on BHs, see Chandrasekhar (1983).

Although SMBHs by definition do not emit, transmit or reflect light, it is possible to measure their properties by using indirect techniques based on observations of the gas distribution around them. The most relevant example is reverberation mapping, which is commonly employed to measure BH masses. This technique estimates the disc radius from the time delay in the response of broad emission lines in the external region of the disc (BLR) to fluctuations in the continuum spectrum emitted in the inner disc. In combination with measurements of rotation-induced Doppler broadening of spectral lines, it is possible to estimate the central SMBH mass (for a review, see Peterson, 2014). These observations have revealed that SMBHs are present in virtually all galaxies (Greene et al., 2010), and their masses span a wide range, i.e. $10^5 - 10^9 M_{\odot}$ (Ferrarese & Ford, 2005). A very recent breakthrough in observations of SMBHs was presented by Event Horizon Telescope Collaboration et al. (2019). They used a large telescope array to obtain the first ever image of the event horizon of a SMBH (M87*).

The accretion of gas through a rotationally-supported disc has the consequence that SMBHs should have a non-vanishing spin. Direct observational measurements of this parameter are challenging and difficult to obtain with modern techniques. Some attempts have been made through X-ray spectroscopy of the iron fluorescence line observed in accretion discs, which allows to estimate the radius of the inner edge of the disc, a quantity directly related to the BH spin. Unfortunately, this technique yields somewhat contradictory results, and hence, models of BH spin evolution are poorly-constrained (for a compilation of observational results, see Reynolds, 2013). Finally, SBMHs are often assumed to have a vanishing electrical charge due to the presence of surrounding plasma, which has a neutralising effect. Nevertheless, this assumption depends on the specific formation scenario and

might not hold under certain conditions (Zajaček et al., 2018).

The mathematical description of an uncharged, rotating BH is given by the Kerr solution of the Einstein field equations (Kerr, 1963), which is a generalisation of the Schwarzschild solution for non-rotating BHs. An interesting consequence of the Kerr solution is the frame-dragging effect (also known as Lense-Thirring precession), which predicts that any object coming close to a rotating BH would be entrained to rotate with it as a mere result of the swirling curvature of the space-time induced by the rotating body. This has interesting consequences on gas accretion and BH spin evolution, and might play a key role in the origin of the galaxy colour bimodality. We explore this scenario in chapter 8.

4.2 Supermassive black hole formation

The presence of SMBHs with masses above $10^9 M_{\odot}$ at redshifts $z > 6.5$ indicates that these objects must have been formed at very early times (Bañados et al., 2016; Mazzucchelli et al., 2017). In spite of this, our understanding of the SMBH formation process is rather limited due to the inherent difficulties and challenges in observing at high redshifts. The few observations we have to date correspond to extremely massive BHs, which are likely rather rare objects and do not represent the bulk of less massive SMBHs formed at that time. From the theoretical side, Rees (1978) has hypothesised three different scenarios whereby a SMBH could form in a galactic nucleus. Thus, SMBHs might be: remnants of massive population III stars, formed from the direct collapse of giant clouds of primordial gas, or a product of runaway collisions and stellar dynamical processes in dense star clusters. For a modern and detailed review on SMBH formation see Volonteri (2010).

The first scenario suggests that massive BHs are a byproduct of the formation of massive population III stars at early times. In some cases, the collapse of pristine gas at redshift $z \sim 20$ might lead to the formation of very massive stars of around $100 M_{\odot}$ (Yoshida et al., 2006), which later on end up as BHs with masses of the same order. These objects would thus serve as the primordial seeds of present-day SMBHs. In the second scenario, the direct collapse of virialised gas clouds of up to $10^6 M_{\odot}$ might result in the formation of SMBHs of mass $M_{\text{bh}} \sim 10^5 M_{\odot}$ on short timescales. The feasibility of this process depends on certain conditions. For instance, considering that gas cooling via metal-line emissions and molecular hydrogen can trigger a small-scale fragmentation that would inhibit the required global collapse, the gas has to be very metal-poor and UV ionising sources have to be present to suppress the formation of molecules. Additionally, residual angular momentum has to

4. SUPERMASSIVE BLACK HOLES

be removed from the gas during the collapse, which can be achieved through central bar instabilities. Finally, in the third scenario, dynamical instabilities in early, dense nuclear star clusters increase the frequency of three body interactions and scattering processes, resulting in the evaporation of stars and a subsequent contraction of the system. In this way, stellar collisions become increasingly frequent and, as a result, very massive stars are formed at cluster nuclei. The remnants of these stars would constitute thus the seeds of SMBHs, with masses of $10^2 - 10^4 M_{\odot}$ (Devecchi & Volonteri, 2009).

Each of these scenarios predicts a different order of magnitude for the masses of the SMBH seeds, which means that they can be tested straightforwardly once statistically relevant observations of high-redshift SMBHs become available. With the advent of the gravitational wave era, opened by the recent discovery of gravitational waves from stellar-mass BHs (Abbott et al., 2016), such observations might be available soon. In the near future, coalescing SMBH binaries in the relevant mass range should become detectable by the Laser Interferometer Antenna (LISA), and thus, it will be possible to constrain the different models of SMBH formation.

4.3 Growth of supermassive black holes

In spite of the uncertain origin of SMBH seeds, observations at high-redshift of extremely luminous quasars have revealed that the main channel of SMBH growth is gas accretion. A basic theoretical picture of this process is given by the Bondi-Hoyle-Lyttleton (BHL) formula (Hoyle & Lyttleton, 1939; Bondi & Hoyle, 1944; Bondi, 1952):

$$\dot{M}_{\text{Bondi}} = \frac{4\pi G^2 M_{\text{bh}}^2 \rho}{c_s^3}, \quad (4.1)$$

where ρ and c_s are the local density and sound speed of the gas in the vicinity of the BH. The BHL formula describes a scenario in which a massive object (e.g. a SMBH) moves through a homogeneous gaseous medium (the ISM) and accretes mass in a spherical fashion as a result of its gravitational influence. This approach is commonly adopted in numerical simulations of galaxy formation because of its simplicity and robustness (for recent examples, see Pillepich et al., 2018; Weinberger et al., 2018; Schaye et al., 2015).

When the accreted gas comes close to the BH, it settles on a geometrically thin, optically thick disc structure that results from the rotational support provided by the gas angular momentum (Shakura & Sunyaev, 1973). Viscous processes in the gas cause the material

in the disc to spiral inward towards the central BH, whilst angular momentum is transported outwards. At the same time, gravitational energy is released in the form of radiation, thereby producing the characteristic spectra seen in quasars and AGNs. A theoretical limit to the accretion rate is imposed by the Eddington luminosity L_{Edd} , which is defined as the maximum luminosity a body can achieve before the radiation pressure outbalances the gravitational force acting inwards, breaking thus the hydrostatic equilibrium. The corresponding Eddington accretion rate is given by:

$$\dot{M}_{\text{Edd}} = \frac{L_{\text{Edd}}}{\epsilon_r c^2}, \quad \text{with} \quad L_{\text{Edd}} = \frac{4\pi G M_{\text{bh}} m_{\text{p}}}{\kappa}, \quad (4.2)$$

where m_{p} is the proton mass, and $\kappa \approx 0.3 \text{ cm}^2 \text{ g}^{-1}$ is the electron scattering opacity. The radiative efficiency ϵ_r determines the fraction of accreted mass processed into radiation by the accretion disc before the gas reaches the innermost last stable circular orbit (ISCO).

4.4 Accretion discs

Accretion discs are the natural product of infalling gas sinking into a SMBH (massive bodies in general) while retaining most of its angular momentum. Before the gas is ultimately accreted by the SMBH, its angular momentum has to be transported outwards and its gravitational energy has to be released. It is commonly assumed that the physical mechanism that drives the angular momentum transport is viscous dissipation produced by magnetorotational instabilities (Balbus & Hawley, 1991). On the other hand, the release of the gravitational energy depends on the specific configuration of the accretion disc. For instance, the energy can be emitted as black body thermal radiation in radiatively efficient discs, with an efficiency of up to 40% for highly spinning BHs. In advection dominated, radiatively inefficient discs, the energy is instead carried away by blown-away gas in the form of kinetic energy. These regimes are closely associated with the thermal and kinetic BH feedback modes employed in recent galaxy formation simulations (for an example, see e.g. Weinberger et al., 2017).

Properties such as the level of ionisation of the gas, the surface density and the mass accretion rate determine the geometry and the optical depth of the accretion disc. The most widely used model is the geometrically thin, optically thick Shakura-Sunyaev α -disc (Shakura & Sunyaev, 1973). The success of this model lies in the simplicity of its analytical treatment, the wide range of physical conditions under which the disc can form and the

4. SUPERMASSIVE BLACK HOLES

early observational evidence that shows that the spectra of quasars are consistent with being produced by an α -disc (Schmidt, 1968). One of the main assumptions of the model is that the disc is stationary, with only an implicit time dependence carried by the disc accretion rate \dot{M} . As a consequence of this, the disc must be in vertical pressure equilibrium and have an inward radial velocity much smaller than the rotational velocity at any given radius, i.e. $v_r(r) \ll v_\phi(r)$. Although the viscosity in the gas has most likely a magnetic origin (Balbus & Hawley, 1991), the high complexity of the underlying mechanism makes any analytical treatment of the viscous terms difficult. In the α -disc model, this is overcome by the following parametrisation of the viscosity ν :

$$\nu = \alpha c_s H, \quad (4.3)$$

where c_s is the sound speed of the gas, H is the scale height of the disc and α is a free dimensionless parameter that goes from 0 for an inviscid Keplerian disc, to 1 for the limiting case in which the inward radial velocity becomes supersonic. Observations suggest that α is in the range $10^{-2} \leq \alpha \leq 1$. In this thesis we adopt the canonical value of $\alpha = 0.1$.

An interesting prediction of the α -disc model is the radius of the inner edge of the accretion disc. For a disc settled around a rotating SMBH, the inner edge is given by the radius of the innermost stable circular orbit (ISCO) r_{isco} . Any gas that comes closer than this radius will be effortlessly accreted by the SMBH as its trajectory is no longer circular. Because of this, such gas cannot provide any viscous support and the accretion disc ends at this radius. Using the Kerr metric for rotating bodies (Kerr, 1963), the radius of the ISCO is given by (Novikov & Thorne, 1973):

$$r_{\text{isco}} = \frac{c}{GM_{\text{bh}}} \left\{ 3 + Z_2 \pm [(3 - Z_1)(3 + Z_1 + 2Z_2)]^{1/2} \right\}, \quad (4.4)$$

$$Z_1 = 1 + (1 - a^2)^{1/3} [(1 + a)^{1/3} + (1 - a)^{1/3}], \quad (4.5)$$

$$Z_2 = (3a^2 + Z_1^2)^{1/2}, \quad (4.6)$$

where a is the dimensionless BH spin parameter. The negative sign in equation 4.4 is taken if the disc is counter-rotating with respect to the BH spin. The positive sign corresponds to the case of co-rotation. For the maximum allowed spin parameter $a = 0.998$ (Thorne, 1974), the value of r_{isco} for a counter-rotating disc is 9 times larger than for a co-rotating one. This direct dependence of r_{isco} on BH spin has also consequences for the fraction of gravitational energy that is radiated away during the gas inspiral phase. For co-rotating discs

with $a = 0.998$, about 40% of the gravitational energy is radiated. This value drops to 5% for non-spinning SMBHs. In chapter 8, we discuss in more detail how different modes of BH spin evolution affect the growth of SMBHs through an α disc and the properties of the host galaxies.

The range of luminosities for which an α -disc can operate is $10^{-2} \lesssim L/L_{\text{Edd}} \lesssim 0.3$, where L_{Edd} is the Eddington luminosity. Above this range, the accretion rate is very high and the disc is no longer in vertical pressure equilibrium, losing thus its vertical support and becoming slim or thick. Slim and thick accretion discs are expected to have large optical depths since the gas inflow timescale can be shorter than the diffusion timescale it takes for the radiation to reach the surface of the disc. As a result, most of the radiated energy is trapped in the gas and ultimately accreted by the SMBH. AGNs with super Eddington accretion rates are the most likely scenarios for the formation of these discs. For very low luminosities and accretion rates, accretion discs can still efficiently remove angular momentum; however, the low density of the gas conspires to increase the cooling timescale, even above the inflow timescale. As a consequence, the gas retains most of its gravitational energy until it is accreted by the SMBH, suppressing thus any radiative emission. These are the so-called advection dominated accretion flows (ADAF). The properties of these discs are strongly influenced by the local magnetic field, resulting in some cases in mass losses through strong winds, which also carries a large fraction of the initial gravitational energy in a kinetic form. For a more thoughtful discussion on accretion discs, see [Netzer \(2013\)](#).

4.5 Black hole demographics

The process of gas accretion onto SMBHs is thought to be the most efficient mechanism to convert mass into energy in the Universe. Owing to this, the spectral energy distribution of an AGN is very broad and specially significant at X-ray wavelengths. Thus, AGNs account for up to 80% of the cosmic X-ray background, as revealed by deep X-ray surveys such as the Chandra X-ray Observatory ([Brandt & Hasinger, 2005](#)). Assuming a constant average radiative efficiency for all AGNs, the density ρ_{bh} of SMBHs can be estimated from the measured integrated energy density due to AGN output. This is the so-called Sołtan argument and was first applied in [Sołtan \(1982\)](#). Modern observational estimates of the density of SMBHs show that $\rho_{\text{bh}} \sim 4 \times 10^5 M_{\odot} \text{Mpc}^{-3}$ ([Marconi et al., 2004](#)).

The spectral energy distribution of AGNs is not only seen in X-rays, but also in other wavelengths such as infrared, optical and radio bands. They constitute together the quasar

4. SUPERMASSIVE BLACK HOLES

bolometric luminosity function (QBLM). Observations have shown that the QBLM evolves in time (Hopkins et al., 2007); thus, for redshifts $z \gtrsim 2$, the QBLM is often described as a double power-law that increases with time. At redshifts $z \lesssim 2$, AGNs become considerably less luminous, impacting thus the normalization of the relation such that at a fixed luminosity, the density of AGNs decreases. This evolutionary trend has important implications for the demographics of AGNs as it shows that massive SMBHs that formed at early times are by now no longer strongly accreting, while less massive SMBHs that formed later on are still very active (AGNs).

4.6 Impact of supermassive black holes on host galaxies

In spite of their tiny sizes when compared to galaxies, SMBHs can produce large amounts of radiated energy, which in some cases, can outshine the host galaxies (e.g. in quasars). Only a small fraction of this energy suffices to significantly impact the properties of the surrounding gas in such a way that the star formation rate is altered in the whole galaxy (King, 2003). Although SMBHs convert accreted mass into energy with an efficiency ϵ_r , which can be as high as 40% for highly spinning BHs, the exact mechanism that couples that energy to the gas is poorly understood. This is mainly due to the inherent theoretical challenges in connecting the huge dynamical range involved in the problem.

From the observational side, there is solid evidence of the existence of tight scaling relations between galaxy properties and the masses of SMBHs (see e.g. Magorrian et al., 1998; Ferrarese & Merritt, 2000; Häring & Rix, 2004). This indicates that BHs are not merely spectators in the galaxy formation process, but rather influence it in decisive ways. The observationally motivated incorporation of BH evolution models and feedback processes in modern theories of galaxy formation has proven to be crucial to account for different phenomena in galaxies (Kauffmann & Haehnelt, 2000). For example, many simulation models explain the quenching transition of galaxies from the star-forming blue cloud to the red sequence of elliptical galaxies as a result of BH feedback (Di Matteo et al., 2005; Springel et al., 2005; Sijacki et al., 2007). In large clusters of galaxies, the BHs can furthermore offset radiative cooling losses through sporadically going through phases of active galactic nuclei (AGN) activity, thereby preventing excessive cooling flows. Another importance of AGN feedback lies in its ability to expel baryons even from deep potential wells of galaxy groups and clusters, helping to understand the observed trends of the baryon content in these objects (McCarthy et al., 2007; Puchwein et al., 2008).

Simulations of galaxy formation

The early evolution of perturbations in the matter content is remarkably well described by the linear regime formalism (see chapter 2). Nevertheless, after the recombination epoch at redshifts $z \lesssim 1100$, once the primordial gas settles at the centre of dark matter haloes, non-linear gravitational evolution and baryonic effects couple the small-scale modes of the density field, thereby breaking the assumption of linear independence and rendering it infeasible to follow the processes of evolution and hierarchical assembly of galaxies in an analytical fashion. Numerical approaches have to be adopted instead as they provide an effective way to solve complex non-linear problems. In this context, computer simulations have become in the last decades an essential tool to understand the problem of structure formation.

In order to realistically reproduce the present-day Universe, state-of-the-art simulations of galaxy formation incorporate a large variety of physical processes that operate at a wide range of scales and are intricately coupled to each other. The latest measurements of the cosmological parameters of the Λ CDM model show that matter is only the second most important component in the Universe after dark energy (Planck Collaboration et al., 2018). Gravity is the main driver of structure evolution at the largest scales, and thus, it must be the basic ingredient of any simulation of galaxy formation. To this end, particle-based methods that discretise the matter content are commonly used to solve gravity at all scales. The measured values of the density parameters $\Omega_m = 0.3089$ and $\Omega_b = 0.0486$ show that around 15% of the matter content corresponds to baryons, which have a collisional nature. This implies that the evolution of baryons is not only governed by gravity but also by the laws of

5. SIMULATIONS OF GALAXY FORMATION

magnetohydrodynamics. Owing to this, different particle-based and mesh-based magnetohydrodynamical schemes are implemented in simulations to solve the baryonic component. Finally, we have seen in the last chapters how small-scale baryonic processes such as gas cooling, star formation, stellar and AGN feedback play a key role in galaxy formation and evolution. In spite of this, these processes cannot be fully resolved in a cosmological setup due to the associated unaffordable computational cost. Instead, coarse-grained sub-grid approaches are often used to approximate this physics at the price of higher systematic uncertainties.

In this chapter, we present the simulations used in this thesis as well as the different models of gravity, magnetohydrodynamics, gas cooling, star formation, stellar feedback and chemical evolution. Note that a section on black hole physics is omitted in this chapter, because the numerical implementation of black hole physics will be discussed in detail in chapter 8, section 8.3.

5.1 Gravitational forces

Given the unknown nature of dark matter, coarse-grained discretisation schemes are commonly employed in simulations to represent the dark matter density field as a collection of particles that interact gravitationally with each other, but ignoring in most cases possible self-interaction effects. The dynamics of collisionless particles that interact via long-range forces (e.g. gravity) can be described by the Vlasov equation:

$$\begin{aligned} \frac{df}{dt} &= \frac{\partial f}{\partial t} + \frac{dx_i}{dt} \frac{\partial f}{\partial x_i} + \frac{dv_j}{dt} \frac{\partial f}{\partial v_j} = 0 \\ &= \frac{\partial f}{\partial t} + v_i \frac{\partial f}{\partial x_i} + \frac{d\phi}{dx_j} \frac{\partial f}{\partial v_j} = 0, \end{aligned} \quad (5.1)$$

where f is the phase-space distribution function and ϕ is the gravitational potential. The Poisson equation links the potential with the density field ρ . In terms of the distribution function, they are expressed as:

$$\rho = m \int f d^3x, \quad (5.2)$$

$$\nabla^2 \phi = 4\pi G(\rho - \bar{\rho}), \quad (5.3)$$

where m is the mass of a simulation particle and $\bar{\rho}$ the mean density of the Universe. Thus, in order to compute the gravitational interaction of collisionless particles in simulations, it

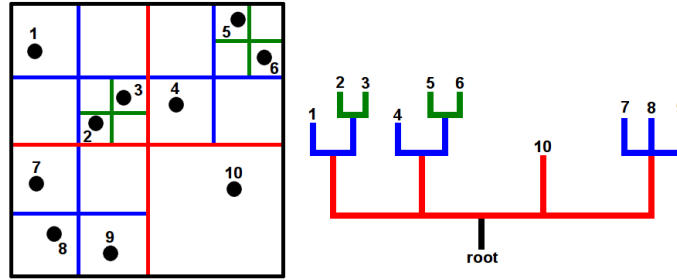


Figure 5.1: Illustration of the construction of a hierarchical oct-tree. The gravitational interaction between simulation particles is computed through direct summation, multipolar expansion or particle mesh techniques according to the level in the tree.

is necessary to solve this system of equations.

The most straightforward of the solutions consists in summing up the monopole contribution of each particle at a given point. This is the so-called direct summation method and is only suitable for problems with a small number of particles (few-body problem) due to its poor CPU-time scalability, i.e. $O(N^2)$, with N the number of particles. For cosmological setups with about $10^8 - 10^{10}$ particles, such a method is computationally unaffordable and other methods have to be implemented instead. For instance, a much faster approximation is the oct-tree method (Barnes & Hut, 1986), in which the simulation volume is hierarchically divided into branches (octants) until each one contains a predetermined number of particles. In Figure 5.1, we illustrate the construction of the tree structure for a random set of particles. The gravitational interaction at a given point is calculated through direct summation, multipole expansion, and particle mesh techniques (see e.g. Dawson, 1983), in order of hierarchy in the tree (for an implementation, see e.g. Springel, 2005). The computing time required to build the tree structure scales with the number of particles as $O(N \log(N))$. Another family of methods consist in solving the Poisson equation directly on a grid with Fourier based techniques (see e.g. Guillet & Teyssier, 2011), or iterative relaxation methods such as the multigrid approach.

5.2 Gas magneto-hydrodynamics

The macroscopic dynamics of the baryonic content of the Universe is governed by the laws of gravity and ideal magnetohydrodynamics (MHD). The equations of ideal MHD are given by:

5. SIMULATIONS OF GALAXY FORMATION

$$\frac{\partial \rho}{\partial t} + \nabla_{\mathbf{r}} \cdot (\rho \mathbf{v}) = 0, \quad (5.4)$$

$$\frac{\partial \rho \mathbf{v}}{\partial t} + \nabla_{\mathbf{r}} \cdot (\rho \mathbf{v} \mathbf{v}^T + p_{\text{tot}} - \mathbf{B} \mathbf{B}^T) = 0, \quad (5.5)$$

$$\frac{\partial E}{\partial t} + \nabla_{\mathbf{r}} \cdot [\mathbf{v}(E + p_{\text{tot}}) - \mathbf{B}(\mathbf{v} \cdot \mathbf{B})] = 0, \quad (5.6)$$

$$\frac{\partial \mathbf{B}}{\partial t} + \nabla_{\mathbf{r}} \cdot (\mathbf{B} \mathbf{v}^T - \mathbf{v} \mathbf{B}^T) = 0, \quad (5.7)$$

where \mathbf{r} is the physical position; ρ , \mathbf{v} and \mathbf{B} represent the local gas density, velocity field and magnetic field strength, respectively. The total gas pressure and total energy per unit volume are defined as $p_{\text{tot}} = p_{\text{gas}} + \frac{1}{2} \mathbf{B}^2$ and $E = \rho u_{\text{th}} + \frac{1}{2} \rho \mathbf{v}^2 + \frac{1}{2} \mathbf{B}^2$, with u_{th} denoting the thermal energy per unit volume (see e.g. [Pakmor & Springel, 2013](#)).

The inherent complexity in solving the previous set of non-linear equations demands the implementation of numerical schemes commonly referred to as hydro-solvers. Traditionally, two different families of hydro-solvers have been used in the context of simulations of galaxy formation, both in isolated and cosmological setups. The first family is the so-called Smoothed Particle Hydrodynamics (SPH), a set of Lagrangian schemes based on moving point masses that represent parcels of the fluid ([Monaghan, 1992](#)) (for an implementation, see e.g. the GADGET code by [Springel \(2005\)](#)); the second family consists of Eulerian solvers on an adaptive stationary mesh known as Adaptive Mesh Refinement (AMR) ([Berger & Colella, 1989](#)) (for an implementation, see e.g. the RAMSES code by [Teyssier \(2002\)](#)).

Owing to the Lagrangian nature of SPH schemes, simulation particles of fixed mass travel by construction along with the fluid. As a consequence, regions of high-density are naturally sampled with a larger number of particles than low-density regions. This feature provides a self-adjusting spatial resolution that allows a rather straightforward computational implementation. Additionally, sub-resolution physics models can be easily incorporated as each simulation particle represents a fixed fluid parcel, and thus, advection terms are automatically accounted for. Nevertheless, SPH schemes have also been shown to spuriously suppress fluid instabilities due to the smoothing and interpolation procedure applied to recover the continuous fluid quantities. Also, shocks, which are crucial in the process of gas accretion into galaxies, are commonly broadened in SPH schemes and require artificial viscosity. In AMR schemes, the fluid equations are directly solved on a fixed mesh that spans the simulation volume and whose resolution can be locally (de)refined. Therefore, no interpolation is required to recover the fluid quantities and shock dynamics and fluid in-

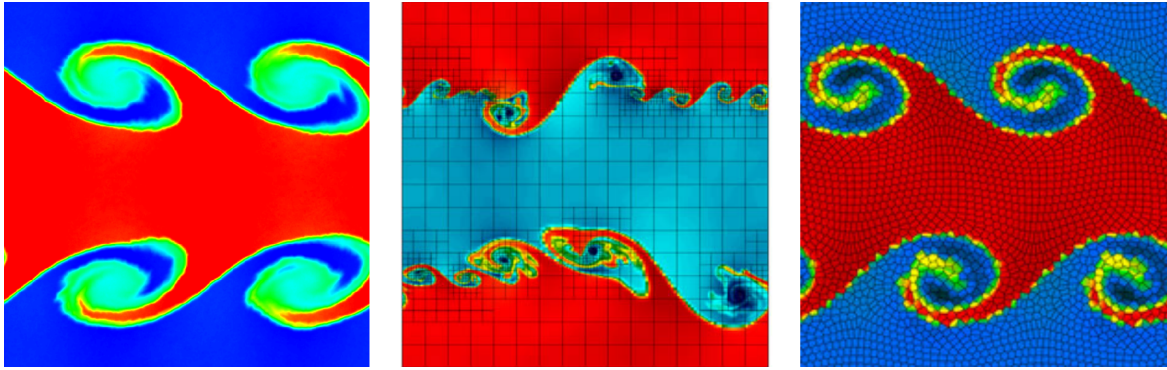


Figure 5.2: Density field of the Kelvin-Helmholtz instability solved with 3 different hydro-solvers. SPH (left), AMR (centre) and the AREPO hydro-solver (right). Image credits: (Price, 2008), (Schive et al., 2010) and (Springel, 2010), respectively.

stabilities are consequently more accurately captured. However, the stationary nature of the grid and its fixed geometry create problems with Galilean invariance and the conservation of angular momentum. For a detailed discussion and comparison of SPH and AMR see Plewa (2001).

Recently, a completely new approach to solve hydrodynamical problems was introduced by Springel (2010) and implemented in the AREPO code. It combines the strengths of AMR and SPH but overcomes many of their weaknesses. This is achieved by solving the fluid equations on an unstructured mesh based on a Voronoi tessellation defined over a set of mesh-generating points that move with the local fluid velocity. The geometry of the mesh resembles very closely that of the point distribution, retaining thus the automatic adaptivity inherent of SPH and also keeping a grid to capture shocks like AMR does. We note that this approach is only approximately Lagrangian as there exist small advection terms across the interfaces of the Voronoi cells, and thus, a volume element represents a fixed parcel of the fluid only during a finite time interval. The previous features make AREPO highly efficient and accurate for simulating a wide range of hydrodynamical problems, making it one of the best available approaches for computing galaxy evolution in the gaseous cosmic web of the Universe.

We show in Figure 5.2 three snapshots of the density field of the Kelvin-Helmholtz instability problem solved with the three different hydro-solvers. For illustrative purposes, the geometry of the underlying mesh is highlighted for AMR and AREPO. For SPH, the density field is reconstructed through a smoothing kernel around each fluid particle.

5.3 Radiative cooling processes

In an ideal, adiabatic and magnetised gas, the evolution of the total energy density is described by equation 5.6. Nevertheless, after the recombination epoch, once baryons decouple from the photon field and collapse into dark matter haloes, non-adiabatic cooling and heating mechanisms such as radiative processes, shock heating, photoionisation from local sources and an ultraviolet background become important. As a consequence, equation 5.6 needs to be modified in order to include source and sink terms, resulting in:

$$\frac{\partial E}{\partial t} + \nabla_{\mathbf{r}} \cdot [\mathbf{v}(E + p_{\text{tot}}) - \mathbf{B}(\mathbf{v} \cdot \mathbf{B})] = -\Lambda_{\text{net}}(\rho, E, \{X\}), \quad (5.8)$$

where $\Lambda_{\text{net}}(\rho, E, \{X\})$ is the cooling function that describes external sinks or sources of heat for the gas. This function generally depends on the the local density, energy (temperature), chemical species present in the gas and external factor such as radiation fields.

Characteristic timescales associated to cooling processes can vary by orders of magnitude from one region to another depending on the local state of the gas. Because of this, the implementation of explicit time integration schemes to solve cooling processes in simulations has proven to be very challenging due to the extremely small time steps that have to be resolved in order to reliably follow the evolution of the gas. A common solution to this consists in using an implicit integration scheme in which adiabatic terms are computed first and then the following implicit equation is solved:

$$\hat{E}_i^{(n+1)} = E_i^{(n)} + \dot{E}^{\text{ad}} \Delta t - \Lambda_{\text{net}} \left[\rho_i^{(n)}, \hat{E}_i^{(n+1)}, \{X\} \right] \Delta t, \quad (5.9)$$

where $\dot{E}^{\text{ad}} \Delta t$ is the adiabatic contribution, i.e. the solution to the homogeneous equation 5.6, i denotes the i -th volume element and n the n -th time step. The corresponding rate of change of the energy density is finally given by:

$$\dot{E}_i = \frac{\hat{E}_i^{(n+1)} - E_i^{(n)}}{\Delta t}. \quad (5.10)$$

In order to prevent numerical issues such as overshooting, which might result in very small or even negative energies, often each resolution element is allowed to lose only half of its energy at a given time step (Springel et al., 2001).

The explicit form of the cooling function $\Lambda_{\text{net}}(\rho, E, \{X\})$ is a superposition of several non-adiabatic cooling and heating (treated as negative cooling) terms. Cooling processes

consist of primordial cooling (Cen, 1992; Sutherland & Dopita, 1993; Katz et al., 1996), metal-line and Compton cooling (Wiersma et al., 2009) and molecular cooling (Glover & Abel, 2008), each of which operates in different regimes of the gas. Heating terms include ionising UV radiation from quasars and early star formation (Haardt & Madau, 2012; Faucher-Giguère et al., 2009), which is usually implemented as a homogeneous background radiation field that affects the gas.

5.4 Star formation and stellar winds

Once the primordial baryons settle in the centre of dark matter haloes, radiative cooling triggers a run away process in which the gas undergoes small-scale fragmentation and gravitational collapse, becoming thus denser and more prone to further cooling. This ultimately results in dense, compact and cold gas clouds that constitute the perfect environment for the formation of stars. The exact physical mechanisms that shape the process of star formation are still a major research topic (Mac Low & Klessen, 2004). In addition to these theoretical uncertainties, computational limitations arise from the minimum mass resolution that can be achieved in simulations for the gas component (around $10^6 M_\odot$ in modern cosmological simulation). This implies that the formation of individual stars cannot be self-consistently followed and sub-resolution effective approaches have to be adopted instead.

One of the most widely used approaches to model the ISM and the star formation process in simulations is the self-regulated two-phase model from Springel & Hernquist (2003). In this model, a resolution element (gas particle or cell¹) of the ISM gas that reaches a density threshold ρ_{th} is split in two non-resolved co-existing phases, namely: an ambient volume-filling hot phase, and a cold phase condensed in clouds from which stars can form, both in pressure equilibrium with each other. Several internal processes govern the mass losses and the mass exchange between the two phases, e.g. star formation, supernovae and cloud evaporation remove mass from the cold phase, whereas thermal instabilities driven by radiative cooling deposit mass from the ambient hot phase into the cold phase. The corresponding evolution equations for the densities are given by:

$$\frac{d\rho_c}{dt} = -\frac{\rho_c}{t_\star} - A\beta\frac{\rho_c}{t_\star} + \frac{1-f}{u_h - u_c}\Lambda_{\text{net}}(\rho_h, u_h), \quad (5.11)$$

¹This ambiguity when referring to a resolution elements is kept as most sub-grid models can be implemented in particle based as well as in grid based hydro-solvers.

5. SIMULATIONS OF GALAXY FORMATION

$$\frac{d\rho_h}{dt} = \beta \frac{\rho_c}{t_\star} - A\beta \frac{\rho_c}{t_\star} - \frac{1-f}{u_h - u_c} \Lambda_{\text{net}}(\rho_h, u_h), \quad (5.12)$$

where ρ_c and ρ_h denote the density of the cold and hot phases, respectively.

The first term of equation 5.11 corresponds to the rate at which the cold gas reservoir is converted into stars, which occurs at a characteristic timescale t_\star , defined as $t_\star \equiv m_g/\dot{m}_\star$, where m_g is the mass of the gas and \dot{m}_\star the star formation rate. The second term corresponds to the rate at which cold clouds are evaporated by nearby supernovae. The efficiency of this process is denoted by A and is usually assumed to be a function of the gas density, i.e. $A \propto \rho^{-4/5}$ (McKee & Ostriker, 1977). The parameter β quantifies the fraction of stars that are very massive ($M > 8 M_\odot$) and die out quickly as supernovae (instantly for computational purposes). The third term corresponds to the rate at which hot gas cools through thermal instabilities. The second and third terms also appear in equation 5.12 but with opposite sign, which reflects the mass exchange between the two phases. In contrast, the first term does not appear as the transformed cold gas stays locked up in the stellar phase. The first term of equation 5.12 corresponds to the gas deposited from the stellar phase into the ambient phase by supernovae of massive stars. Note that only gas in the hot phase is assumed to experience radiative cooling.

In the model of Springel & Hernquist (2003), the characteristic timescale of star formation is set to be a function of the density ρ :

$$t_\star(\rho) = t_0^\star \left(\frac{\rho}{\rho_{\text{th}}} \right)^{-1/2}, \quad (5.13)$$

where t_0^\star is the a free parameter that is calibrated to reproduce the Kennicutt-Schmidt law (Kennicutt, 1998), an observational relation that links the total gas surface density Σ_{gas} with the star formation surface density Σ_{SFR} . The equation that balances the rate at which gas is locked up in the stellar phase \dot{m}_\star , mass losses from the cold gas phase \dot{m}_g , and the rate at which hot gas is ejected in the form of stellar winds by core collapse (SNII) supernovae and stars in the asymptotic giant branch (AGB) phase \dot{m}_w is given by

$$\dot{m}_\star(1 + \eta_w) = -\dot{m}_g, \quad (5.14)$$

where $\eta_w = \dot{m}_w/\dot{m}_\star$ is the mass loading factor. Combining this with equation 5.13 and integrating yields:

$$\dot{m}_{\star,w} = m_g \left(1 - e^{-(1+\eta_w)\Delta t/t_\star} \right). \quad (5.15)$$

Accounting for star formation by directly solving this balance equation for each gas particle/cell poses the problem that the related processes are occurring at sub-resolution scales. While the hot and cold phases can coexist because they are both collisional components, keeping track of an extra collisionless stellar phase within the same resolution element is technically unfeasible. An elegant alternative to overcome this issue is to adopt a probabilistic approach instead (Springel & Hernquist, 2003). The combined probability for star formation and wind launching can be defined as:

$$P_{\star,w}(t_{\star}) \equiv 1 - e^{-(1+\eta_w)\Delta t/t_{\star}}. \quad (5.16)$$

Thus, a gas particle/cell will be completely converted into a stellar/wind particle with a probability $P_{\star,w}$, keeping in this way the stellar and the gas components separated. While this is a rather imprecise and rough approximation at small scales, it is numerically robust and satisfies the balance equation 5.14 at macroscopic scales. Gas particles/cells that are not converted and have a density above the threshold value ρ_{th} are still evolved with equations 5.11 and 5.12. On the other hand, converted gas particles/cells can become either stellar particles or wind particles, with probabilities $1/(1 + \eta_w)$ and $\eta_w/(1 + \eta_w)$, respectively. Stellar particles inherit the properties of their parent gas particles/cells, including position, mass, momentum and metallicity, are treated as a collisionless component and represent a single stellar population (SSP) with a given initial mass function (IMF), usually a Salpeter (1955) or a Chabrier (2003) IMF. On the other hand, wind particles represent a parcel of ejected gas and thus, they still have a collisional nature. They also inherit the properties of the parent gas particle/cell and are additionally launched with a velocity that scales with the local one-dimensional dark matter velocity dispersion (Okamoto et al., 2010). In order to simulate the launching and ejection process, they are temporarily decoupled from the hydrodynamic interactions until they reach a low density region with density $\rho < 0.05\rho_{\text{th}}$, or a maximum travel time is exceeded (typically 2.5% of the Hubble time at the corresponding redshift). After one of these conditions is met, they are recoupled and either become fluid particles in particle based hydro-solvers, or deposit all their mass together with metals, thermal energy and momentum into the nearest gas cell in mesh based hydro-solvers.

5.5 Chemical evolution

In addition to building up the stellar content in galaxies, the process of star formation also drives the enrichment of metals in the gas component. Together with primordial nucleosynthesis, stellar processes such as SNII and SNIa supernovae, and winds from AGB stars constitute the primary mechanisms to produce and distribute metals in the Universe.

As discussed before, the massive stellar precursors of SNII supernovae are assumed to die out instantly, which together with the fraction of AGB stars in each SSP, result in the probabilistic generation of wind particles. These particles carry away the mass of the expelled gas and are loaded with heavy elements according to SNII (see e.g. [Portinari et al., 1998](#)) and AGB (see e.g. [Karakas, 2010](#)) yields. The enriched material is deposited into the gas once the wind particles are recoupled into the hydrodynamics. On the other hand, the stellar precursors of SNIa supernovae live longer and thus, the number of SNIa events has to be calculated by integrating the delay time distribution $g(t)$:

$$N_{\text{Ia}}(t, \Delta t) = \int_t^{t+\Delta t} g(t' - t_0) dt', \quad (5.17)$$

$$g(t) = \begin{cases} 0 & \text{if } t < \tau_{8M_{\odot}}, \\ N_0 \left(\frac{t}{\tau_{8M_{\odot}}} \right)^{-s} \frac{s-1}{\tau_{8M_{\odot}}} & \text{if } t > \tau_{8M_{\odot}}, \end{cases} \quad (5.18)$$

where N_0 is a normalisation parameter typically set as twice the supernovae rate. $s = 1.12$ and $\tau_{8M_{\odot}} = 40$ Myr are the power law index and the main sequence lifetime of a $8 M_{\odot}$ star, which is the upper mass limit for SNIa. The corresponding amount of mass and metals that are returned to the ISM are calculated from SNIa yield tables (see e.g. [Thielemann et al., 2003](#); [Travaglio et al., 2004](#)), and distributed among neighbouring gas particles/cells for each stellar particle.

5.6 Simulations

All the simulations used throughout this thesis were carried out with the code AREPO and make use of the previously described techniques and sub-grid models, which are also integrated in the code. In chapter 6, we use the set of simulated Milk-Way-like galaxies of the Auriga project ([Grand et al., 2017](#)). In chapter 8, we run cosmological simulations that employ the physics model of the IllustrisTNG project ([Pillepich et al., 2018](#); [Springel et al., 2018](#)). A complete description of these simulations is presented in the respective chapters.

Part II

Evolution of star formation and metallicity in galaxy mergers

Merger-induced metallicity dilution in simulations

In this chapter, we analyse the process of SFR enhancement and metallicity dilution in simulated merging galaxies. This work was published in Monthly Notices of the Royal Astronomical Society, Volume 479, Issue 3, p.3381-3392.

6.1 Introduction

The interstellar medium (ISM) in galaxies is steadily enriched by heavy elements formed during the life and death of stars. This enrichment is accompanied by accretion of low-metallicity gas from reservoirs surrounding galaxies. Observations yield a correlation between the stellar mass (M_*) and the metallicity of the star-forming gas (Z_{gas}) of galaxies (Tremonti et al., 2004). The existence of this correlation shows that the heavy chemical elements of a galaxy are – at least to first order – gradually built up during its lifetime. However, the relation has a significant scatter of 0.1 dex (Tremonti et al., 2004), indicating that galaxies evolve on diverse paths through the M_*-Z_{gas} -plane.

A partial reason for the scatter in this relation is that galaxies with high star formation rates (SFR) at a fixed stellar mass usually have lower metallicities than galaxies with smaller SFR. This behaviour is encoded in the observation that galaxies evolve on a two-dimensional curved surface, dubbed the *fundamental metallicity relation* (FMR), in a three-dimensional

6. MERGER-INDUCED METALLICITY DILUTION IN SIMULATIONS

space defined by the SFR, M_* and Z_{gas} of galaxies (Ellison et al., 2008a; Mannucci et al., 2010). While the presence of this relation has been confirmed by several studies (Lara-López et al., 2010; Belli et al., 2013; Stott et al., 2013; Yabe et al., 2015), it has, however, been questioned whether the FMR is *fundamental* (i.e. redshift-independent) because several observations at $z \sim 2.3$ reveal differences from the FMR in the local Universe (Salim et al. 2015; Brown et al. 2016; Grasshorn Gebhardt et al. 2016; Sanders et al. 2018, see also Christensen et al. 2012 for a study of $1 < z < 6$ lensed galaxies). Sanders et al. (2018) suggest that the redshift-evolution of the FMR can be explained by an evolution of the mass-loading factor at fixed stellar mass, and by an evolution of the metallicity of infalling gas.

Even though the FMR might be redshift-dependent, it is interesting to ask what is driving its shape. A simple analytical model by Dayal, Ferrara & Dunlop (2013) explains the local FMR by accounting for star formation, inflow of metal-poor gas from the intergalactic medium, and outflow of gas from the interstellar medium. The FMR has also been reproduced in more sophisticated hydrodynamical galaxy formation models (Lagos et al., 2016; De Rossi et al., 2017; Davé et al., 2017; Torrey et al., 2019).

Galaxy pairs are observed to have lower gas-phase metallicities and an increased SFR compared to isolated galaxies with comparable stellar masses (Ellison et al., 2008b; Scudder et al., 2012; Cortijo-Ferrero et al., 2017). They also show a flattening of the standard radial metallicity gradient in the case of spiral galaxies (Rupke et al., 2010; Kewley et al., 2010; Perez et al., 2011). Qualitatively, this agrees well with the FMR, but a careful statistical study of SDSS galaxies shows that the FMR has an overabundance of outliers (compared to a Gaussian distribution of residuals), which might be caused by interacting galaxies with strong merger-induced gas inflows that dilute the metallicity and enhance the SFR (Grønnow et al., 2015).

Given that observations can only probe a single instant in time of any individual merger, it is helpful to use simulations to establish how the metallicity dilution and SFR-enhancement in mergers occur. Remarkable insights have been gained about the metallicity evolution of mergers based on idealised simulations, where two equilibrium galaxies are set up to collide on a Keplerian orbit. Torrey et al. (2012), for example, established that metallicity dilution is associated with nuclear inflows, and metallicity enhancement is caused by chemical enrichment from active star formation. Even though idealised merger simulations can give important hints on how a merger makes the gas migrate inwards and subsequently causes a starburst, it is important to keep in mind that such simulations are

not cosmologically self-consistent. Cooling of hot gas onto the ISM (Moster et al., 2011), accretion of minor galaxies, and post-merger gas accretion (which proves to be important, e.g. Sparre & Springel, 2017) are usually not included in idealised simulations. Properly accounting for these phenomena gives a more realistic view of how the metallicity dilution and SFR-enhancement occur in real galaxies.

In this chapter, we study the metallicity dilution of galaxies in galaxy mergers based on a large set of high-resolution cosmological simulations. In addition to having realistic collision orbits and structures of the involved galaxies, using cosmological simulations also makes it possible to self-consistently study how the galaxy properties evolve before and after the merger under the influence of the surrounding gas reservoirs. We can use this to reveal for the first time how simulated mergers evolve relative to the FMR.

In Section 7.2, we present the Auriga simulations on which our analysis is based, and we briefly discuss the implemented physics model and the selection of our sample of mergers. In Section 6.3, we correlate both metal dilution and SFR-enhancement with the mass-ratio of the mergers. We also study how the metallicity dilution depends on the separation of the merging galaxies. In Section 6.4 we analyse how mergers behave relative to the FMR. Finally, we discuss our results and conclude in Sections 6.5 and 6.6, respectively.

6.2 Simulations and sample selection

6.2.1 Auriga simulations

The simulations studied in this chapter are based on the Auriga project (Grand et al., 2017), which comprises a set of 30 cosmological magneto-hydrodynamical zoom simulations of the formation of late-type isolated galaxies within Milky Way mass dark haloes. These haloes were extracted from a parent dark matter only simulation in a periodic cube of 100 comoving Mpc on a side from the EAGLE project (Schaye et al., 2015), and were selected to have a viral mass¹ in the range $10^{12} < M_{200}/M_{\odot} < 2 \times 10^{12}$, and to satisfy a mild isolation criterion at $z = 0$. However, no selection criteria were imposed at $z > 0$, therefore the merger histories are unconstrained and exhibit a variety of evolutionary paths. The simulations were carried out with the moving-mesh code AREPO (Springel, 2010; Pakmor et al., 2016). A Planck-2014 Λ CDM cosmology (Planck Collaboration et al., 2014) was adopted, specified

¹Defined to be the mass inside a sphere in which the mean matter density is 200 times the critical density, $\rho_{\text{crit}} = 3H^2(z)/(8\pi G)$.

6. MERGER-INDUCED METALLICITY DILUTION IN SIMULATIONS

by $\Omega_m = 0.307$, $\Omega_b = 0.048$, $\Omega_\Lambda = 0.693$ and Hubble constant $H_0 = 100 h \text{ km s}^{-1}$, with $h = 0.6777$. We refer the reader to [Grand et al. \(2017\)](#) for a detailed and comprehensive description of the simulations.

6.2.2 Definition of the merger sample

To construct our global merger sample we use the 30 Auriga simulations at resolution *level 4*¹. Galaxies and merger trees are identified by standard methods ([Rodriguez-Gomez et al., 2015](#); [Springel et al., 2005](#)). We define merger events as times when a galaxy has more than one direct progenitor and each progenitor has a stellar mass of at least 1% the stellar mass of the main progenitor. This is done in order to avoid spurious effects introduced by unresolved objects. With these conditions, we obtain 137 mergers.

For each galaxy merger we define the stellar mass-ratio, μ , as the mass of the secondary galaxy divided by that of the main progenitor. We determine the stellar masses at the time when the mass of the secondary galaxy reaches its local maximum before the merger. We define the merger ratio in such a way that we always have $\mu \leq 1$.

To characterise the mergers we also calculate the *time of first pericentral passage*, t_{per} , and the *time of final coalescence*, t_{coal} . We define the latter as the peak time of the central black hole accretion rate, or the time at which the mean radial distance of the 10 most bound particles of the secondary progenitor reaches the half-mass radius of the main progenitor, whichever is later. As a caveat, due to the relatively sparse temporal frequency at which the snapshots of the simulations are stored, i.e. $\sim 100 \text{ Myr}$ at the redshift range of our sample, all temporal quantities associated to the mergers have an intrinsic uncertainty of about this value.

We restrict ourselves to coalescence times corresponding to $z_{\text{coal}} \leq 1.5$, and we require the most massive galaxy in a merger to have at least $M_* \geq 10^{9.5} M_\odot$. We briefly remind the reader that the limited $z = 0$ mass range of the Auriga galaxies sets an upper limit of $M_* \simeq 2 \times 10^{11} M_\odot$ on our merging galaxies.

To create a master sample consisting only of *clean mergers*, from our global sample we exclude those that have other mergers in a short timespan; we specifically require no other mergers with $\mu > 1 : 100$ to occur within 1 Gyr of the first pericentral passage and of final coalescence, i.e. in the time interval $t_{\text{per}} - 1 \text{ Gyr} < t < t_{\text{coal}} + 1 \text{ Gyr}$.

In a few instances, our merger tree method has problems to properly track the main

¹In the nomenclature of [Grand et al. \(2017\)](#).

progenitor. This happens when we have two galaxies of similar mass experiencing a fly-by, but no subsequent merger. In these cases the merger tree algorithm may swap the assignment of being the main progenitor several times back and forth between the two galaxies. We exclude epochs from our sample where such progenitor swaps occur.

With these selection criteria we obtain a master sample of 70 mergers, allowing us to statistically study the properties of mergers. To summarize, all these mergers occur at $z < 1.5$ and have masses of $10^{9.5}M_{\odot} \leq M_* \leq 2 \times 10^{11}M_{\odot}$. The total gas fractions of the mergers, defined relative to the total halo mass, range from 9% to 16%, meaning that they are typically gas-rich, and thus ideal to study the process of metallicity dilution.

6.2.3 A sample of isolated galaxies

In Section 6.4.1 we will compare our merger sample with isolated galaxies. We construct a suitable comparison sample by marking those Auriga galaxies as isolated where no mergers with $\mu \geq 1 : 100$ occur within 1 Gyr. To be specific, we exclude all times within time-intervals, $t_{\text{per}} - 1 \text{ Gyr} < t < t_{\text{coal}} + 1 \text{ Gyr}$, of any $\mu \geq 1 : 100$ merger.

6.2.4 Physics model

All simulations use the Auriga galaxy formation model, see [Grand et al. \(2017\)](#) for a comprehensive overview. As highlighted in [Torrey et al. \(2012\)](#), there are four key processes that influence the evolution of metallicity and star formation in galaxies, namely nuclear inflows of low-metallicity gas, chemical enrichment from active star forming regions, galactic outflows and locking of gas-phase metallicity in the stellar phase. Metallicity dilution and SFR-enhancement can therefore be understood as a consequence of the competition between these processes, where usually nuclear inflow and chemical enrichment dominate at low and high redshift, respectively. Below we concisely describe how these different aspects are accounted for in the Auriga physics model (for more details, see [Vogelsberger et al., 2013](#); [Marinacci et al., 2014](#); [Grand et al., 2016](#)).

For modelling the interstellar medium (ISM), the subgrid two-phase model first presented in [Springel & Hernquist \(2003\)](#) is implemented. In this, star-forming gas cells are considered to be composed of two different phases, namely a cold, dense phase embedded into a hot, diffuse ambient medium. Above a density threshold of $n = 0.13 \text{ cm}^{-3}$, gas cells are assumed to enter a thermally unstable star-forming regime where, according to the [Chabrier \(2003\)](#) initial mass function, they are stochastically converted either into a star particle or a

6. MERGER-INDUCED METALLICITY DILUTION IN SIMULATIONS

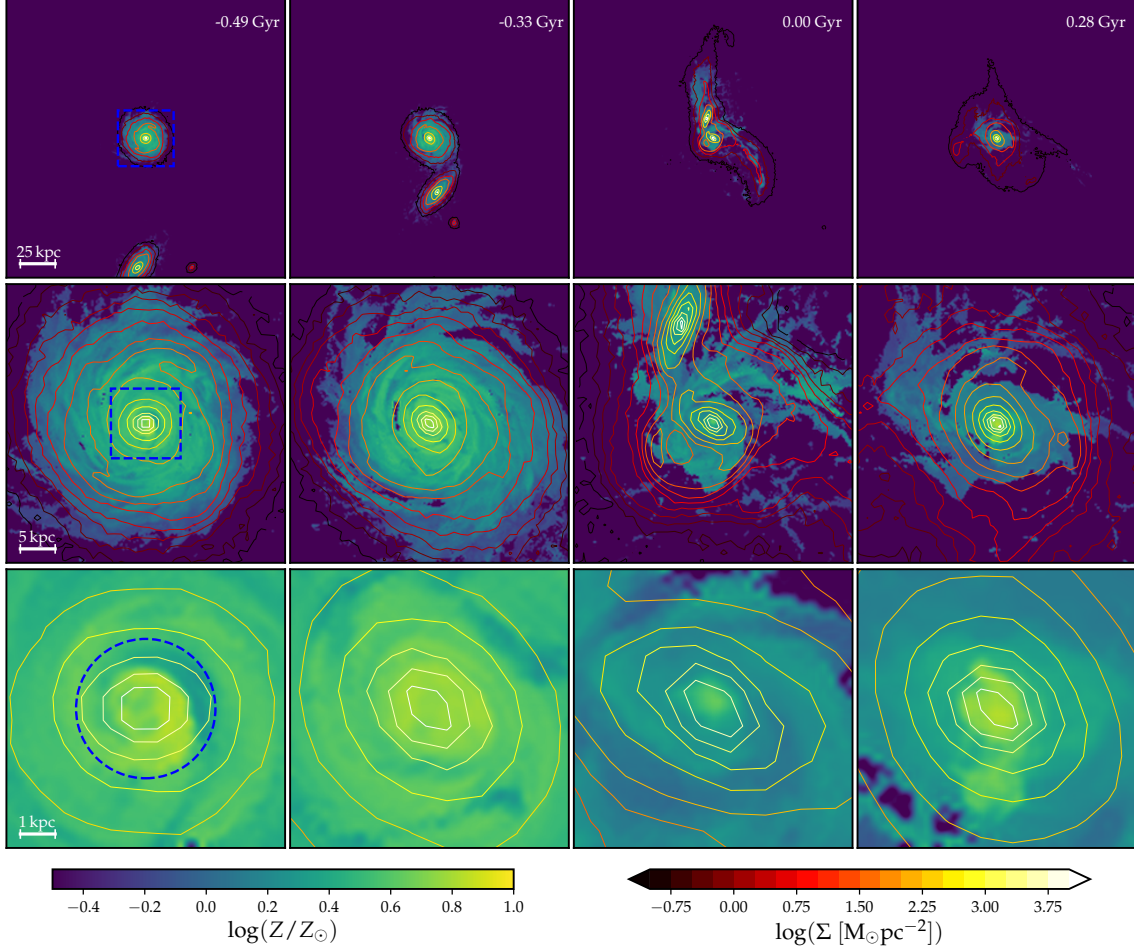


Figure 6.1: Projection of the SFR-weighted gas-phase metallicity (colour map) and stellar surface density (colour contours) of the primary galaxy in *merger 1*. From left to right we show 4 different snapshots of the evolution, corresponding to -0.49 , -0.33 , 0 and 0.28 Gyr. From top to bottom we show different zoom levels with 200, 40 and 8 kpc on a side, respectively. For the first and second rows, the white dashed-line squares enclose the region shown in the next zoom level. For the third row, the white dashed-line circles correspond to the central 2 kpc-radius region for which we calculate all the studied properties. The metallicity in the nuclear region reaches its lowest value close to the coalescence time ($t = 0$ Gyr), when the gas inflow is strong. Furthermore, we note that outside this region there is also a somewhat weaker dilution, indicating that the dilution process extends across the galactic disc. In the post-merger stage, the metallicity increases again in an inside-out way.

6.3 Metallicity dilution and starburst properties

SNI feedback-induced wind particle launched in an isotropic direction. In the former case, the created star particle represents a single stellar population with a given age, mass and metallicity. Metal enrichment and mass loss from SNIa (Thielemann et al., 2003; Travaglio et al., 2004) and AGB stars (Karakas, 2010) are modelled by calculating how much mass per star particle moves off the main sequence at every time step. The returned metals and gas mass are then deposited into nearby gas cells with a top-hat kernel.

Note that the implemented gas-recycling approach is drastically different from the stochastic approach presented in Torrey et al. (2012), where a star particle has a probability to become a SPH gas particle depending on a characteristic recycling timescale. Although their approach gives a less accurate tracking of the spatial and temporal distribution of metals and mass, it allows the tracing of the origin of any particular mass or metal element, thereby allowing to differentiate enriched metals from an initially set metallicity profile. In our case of cosmological simulations, all the metal content is produced from star formation enrichment within the simulation. The wind particles are launched with a metal content determined by the initial gas-phase metallicity, and are re-coupled to the gas once they reach a gas cell with a density below 0.05 times the density threshold for star formation or a maximum travel time is exceeded. In either of these cases, their metal, mass, momentum and energy contents are deposited into the local gas cell. This ensures that the wind material leaves its launching site, favouring the production of gas outflows in the simulation.

Additionally, we include prescriptions for a uniform background UV field for reionization (completed at $z = 6$), primordial and metal line cooling, magnetic fields, as well as subgrid models for black hole seeding, growth through accretion and associated feedback.

6.3 Metallicity dilution and starburst properties

To introduce the concept of metallicity dilution we show the evolution of the SFR-weighted gas-phase metallicity of the primary galaxy of one of the major mergers in our sample in Figure 6.2. Note that we use SFR-averaged metallicities to mimic observations of HII regions of star-forming gas. The projections in Figure 6.2 are done onto the galactic plane for 3 different zoom levels of 200, 40 and 8 kpc. In the analysis we adopt a solar metallicity of $Z_{\odot} = 0.02$. For the first two snapshots, shown in the first and second columns, we see that the metallicity profile does not change appreciably, and it is only when the secondary galaxy comes closer than 40 kpc that the metallicity gets significantly diluted, as seen at the coalescence time in the third column (see also *merger 1* in Figure 6.2). In the fourth column,

6. MERGER-INDUCED METALLICITY DILUTION IN SIMULATIONS

0.28 Gyr after the merger, the enhanced SFR replenishes the metal content of the gas in the central region through stellar enrichment, defining thus the end of the dilution period. In the following, we study the dilution process in galaxy mergers in more detail.

6.3.1 Time evolution

To introduce the primary quantities we use in our analysis, we plot the evolution of four different mergers from our sample in Figure 6.2. These mergers are selected as representative cases for major mergers (defined to have $\mu > 1/3$, which is also the same criterion used to select major mergers, e.g., in Lotz et al. 2008).

In order to quantify the behaviour of metallicity dilution and SFR-enhancement during a merger, we analyse the nuclear region of the main progenitor. We define the nuclear region to be a sphere of radius 2 kpc around the galactic centre (identified with the minimum of the galactic gravitational potential). This cut is chosen to mimic the effect of a limited aperture of a SDSS fibre. For each snapshot we define the SFR-averaged metallicity as

$$Z_{\text{gas}} = \frac{\sum_i \text{SFR}_i Z_i}{\sum_i \text{SFR}_i}, \quad (6.1)$$

where i runs over all gas cells inside the nuclear region, SFR_i and Z_i are the instantaneous star formation rate and the fraction of gas mass in metals in the i -th gas cell, respectively.

In the first row in Figure 6.2, the gas-phase metallicity has been calculated based on the gas cells inside the galaxy corresponding to the main branch of the merger tree, as a function of time. The evolution of Z_{gas} reveals that these galaxies experience a dilution of metallicity right before or at the time of the SFR peak. To quantify the metallicity dilution, we define the pre-merger background metallicity level as the previous local maximum prior to the time when the metallicity minimum occurs. We refer to the time where we determine the background metallicity as $t_{Z_{\text{max}}}$. In the plot, the background and minimum metallicity levels are marked as the ends of the dashed vertical lines, which represent the metallicity dilution times. Based on the ratio of these two levels we define $\Delta \log Z_{\text{gas}}$, which we will refer to as the metallicity dilution.

The second row shows the SFR, which is calculated in the same fashion as the metallicity. The SFR peaks, marked by dashed vertical lines, are determined as the largest SFR-value of the main progenitor within 1 Gyr of the merging time registered in our merger trees. To determine the fractional increase in SFR due to the merger-induced starbursts,

6.3 Metallicity dilution and starburst properties

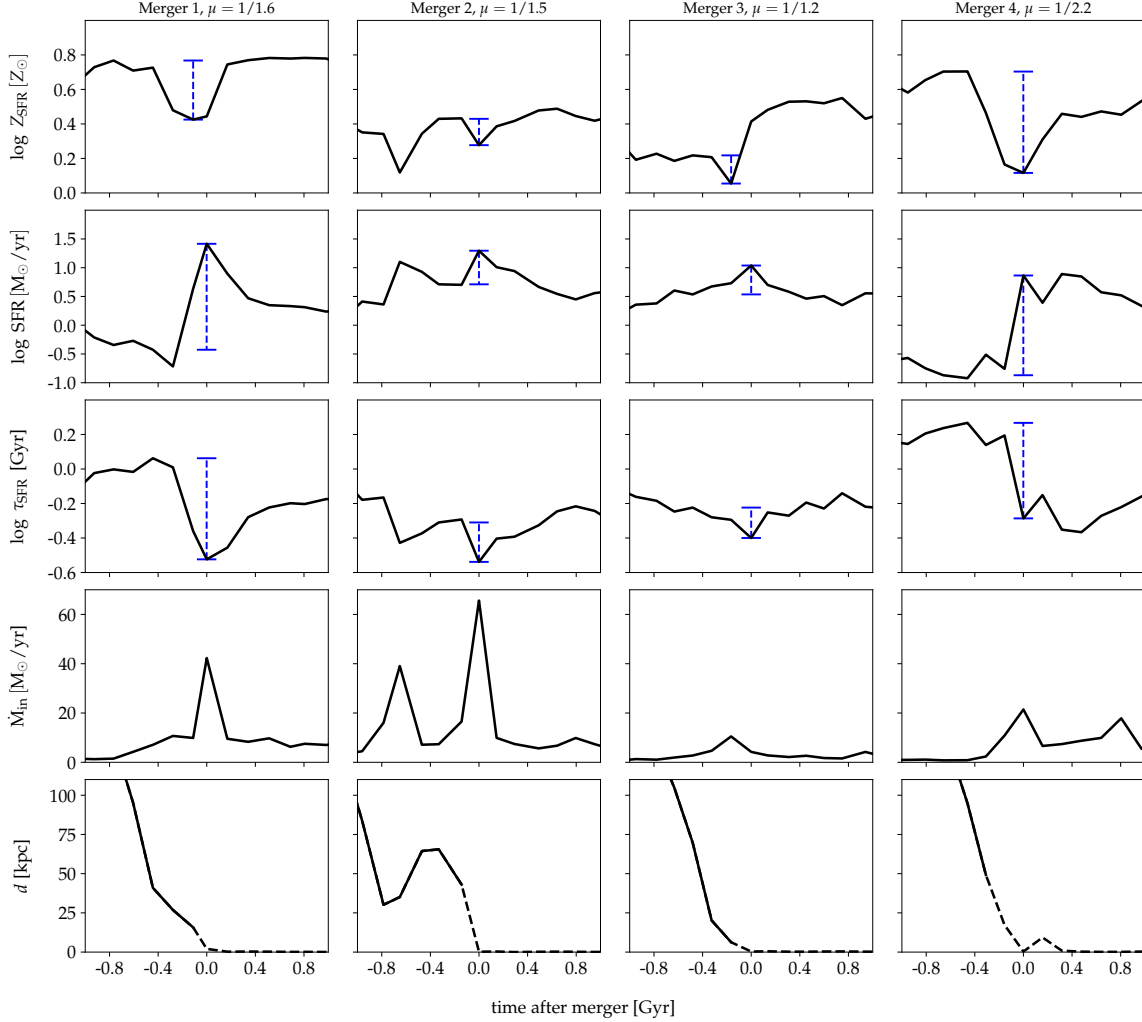


Figure 6.2: We show four typical major mergers, each presented in a separate column headed by the mass ratio. From top to bottom we show the time-evolution of the gas metallicity inside 2 kpc (first row), the SFR (second row), the gas consumption timescale (third row) and the nuclear gas inflow rate (fourth row). We also show the radial distance between the two galaxies (fifth row), where dashed lines correspond to a reconstruction of the orbit based on the most bounded particles of the secondary galaxy after both galaxies have fused in the merger trees. The x -axis shows the time elapsed since t_{coal} , with negative values corresponding to pre-coalescence stages. In the first three rows, vertical dashed lines correspond to the fractional changes of the respective quantities. We see that these major mergers of our sample cause a significant metallicity dilution (especially for *merger 1* and *merger 4*), strong SFR-peaks, and a decrease in the gas consumption timescale, demonstrating that those mergers form stars in a more bursty mode.

6. MERGER-INDUCED METALLICITY DILUTION IN SIMULATIONS

we measure the pre-merger background SFR-level by applying a smoothing algorithm to filter out short timescale fluctuations over 1 Gyr. Then, we find the local minimum before the SFR-peak. The background SFR-level is determined as the corresponding value in the original non-smoothed profile, and the time at which this occurs defines $t_{\text{SFR,min}}$. The fractional SFR-enhancement is then calculated as the ratio between the peak SFR and the background level. In the remaining parts of the chapter we will use $\Delta \log \text{SFR} \equiv \log[\text{SFR}(\text{peak})/\text{SFR}(\text{background})]$ to quantify this fractional enhancement.

We see that the two strongest fractional metallicity dilutions occur in *merger 1* and *merger 4*. For *merger 2* and *merger 3*, we see a somewhat weaker dilution. Establishing the presence of metallicity dilution in cosmological simulations is a notable result, since this has so far mainly been studied in idealised merger simulations. The only other work that has found this effect in a cosmological simulation is [Torrey et al. 2019](#) (see the left panel of their Fig. 9), who identified a merger-induced epoch of metallicity dilution in a $M_* = 10^9 M_\odot$ galaxy.

The third rows show the ISM gas consumption timescale, calculated as the ratio of the ISM gas mass (M_{ISM} , calculated using Eqn. 1 from [Torrey et al. 2012](#)) and the SFR of the galaxy. We calculate this based on the ISM-gas-cells of the primary galaxy. The evolution of the gas consumption timescale reveals that merger-induced starbursts are typically associated with a decrease in the ISM gas consumption timescale, quantified in a similar fashion as for the gas-phase metallicity dilution, i.e. as the logarithm of the ratio between the nearest local minimum to the SFR-peak and the pre-merger local maximum $\Delta \log \tau_{\text{SFR}}$. This behaviour is also identified in the merger simulations of [Sparre & Springel \(2016\)](#), which uses the same physical galaxy formation model that we employ. A decrease in τ_{SFR} shows that star formation occurs in a more bursty mode than for normal star-forming galaxies. A similar bursty mode is observed in galaxy mergers and ULIRGS ([Sanders et al., 1991](#); [Daddi et al., 2010](#); [Krumholz et al., 2012](#); [Scoville, 2013](#)).

Additionally, we show the nuclear gas inflow rate and relative radial distance (fourth and fifth rows, respectively). Note that all SFR-peaks and metallicity dilutions are accompanied by a conspicuous increase in the nuclear gas inflow, supporting thus the scenario where infalling pristine gas disrupted during the merger is the main driving mechanism of the dilution. The post-merger gas-phase metallicity level can vary widely from galaxy to galaxy depending on the infalling gas supply. For example, for *merger 1* and *merger 2*, the post-merger levels are similar to their pre-merger values owing to comparable pre- and post-merger gas supplies. In *merger 3*, the gas supply is not enough to counteract enrichment

from recently formed stars, and the post-merger metallicity is thus much larger than the pre-merger value. The opposite case occurs in *merger 4*, where a continuous post-merger gas supply keeps diluting the metallicity.

6.3.2 Correlations

Having shown that four of our mergers in subsection 6.3.1 have a strong SFR-peak associated with a decrease in the gas consumption timescale and the nuclear metallicity, we will now study the behaviour of these quantities in our full merger sample. In order to do so, we show how $\Delta \log \text{SFR}$, $\Delta \log Z_{\text{gas}}$ and $\Delta \log \tau_{\text{SFR}}$ correlate with μ in Figure 6.3.

First, we see that the strongest SFR-enhancements occur in mergers with large merger ratios. For example, the three highest values of $\Delta \log \text{SFR}$ occur in galaxies with $\mu > 0.5$. This is in good agreement with other studies showing that major mergers cause strong starbursts (Mihos & Hernquist, 1996; Barnes, 2004; Springel et al., 2005; Hayward et al., 2014). Specifically, the range of our relative SFR-enhancements for major mergers is in good agreement with what is typically found in idealised simulations (Martig & Bournaud, 2008; Di Matteo et al., 2008; Teyssier et al., 2010; Hopkins et al., 2013; Karman et al., 2015; Moreno et al., 2015; Gabor et al., 2016).

For low merger mass-ratios of $1/30 < \mu < 1/3$ there are a few mergers with relatively large SFR-enhancement of around 1.0 dex. Further inspection shows that while the merger goes on, there is another galaxy on its first passage around the main galaxy of the merger. The time between coalescence of the two galaxies, which are about to merge with the main galaxy, is more than 1 Gyr, which is why these galaxies have not been filtered out by our selection criteria for mergers to be *clean*. We have marked all these merging systems, which are affected by a third galaxy, with a square in the figure. The presence of systems where more than two galaxies are participating in the merger is a clear consequence of our use of cosmological simulations, where mergers do not occur in isolation. An interesting conclusion is that a minor merger – if we include the full cosmological structure in the surroundings including other galaxies – can trigger a star formation enhancement which is comparable to a major merger. This is not the first time such systems of multiple interacting galaxies are reported. For example, one of the systems (1349-3) from the simulations of Sparre & Springel (2016) also consists of multiple merging galaxies, and the observations of Stephan’s Quintet also reveal such a system. Even though such systems of multiple interacting galaxies are expected to occur in the real Universe, they have, however, been largely

6. MERGER-INDUCED METALLICITY DILUTION IN SIMULATIONS

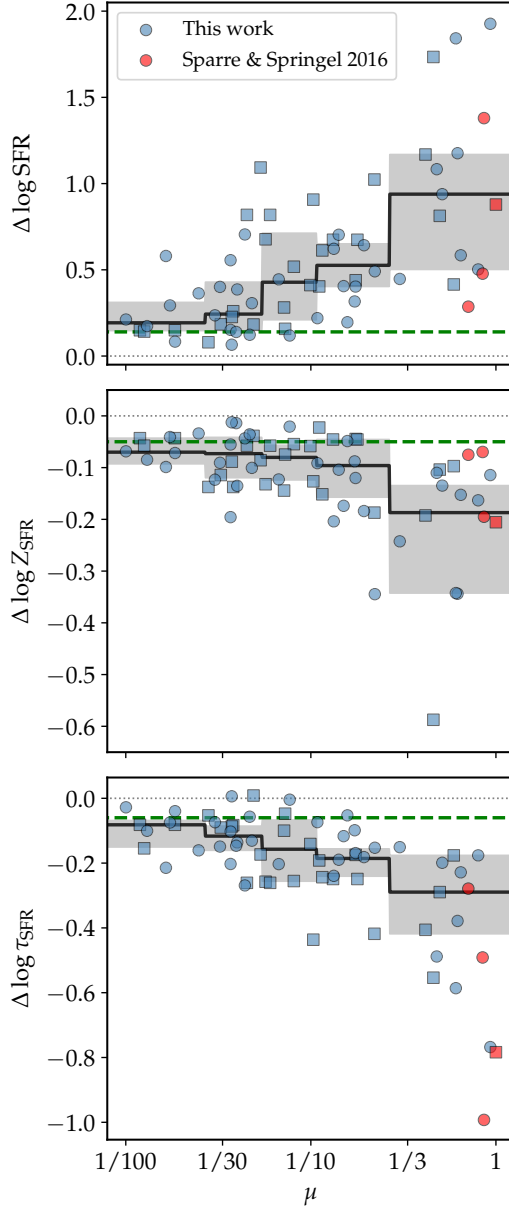


Figure 6.3: Dependence of the fractional enhancement/dilution of SFR (top panel), metallicity (middle panel) and gas depletion timescale (bottom panel) on the merger mass-ratio (μ). Solid lines correspond to median values, and grey regions to 25%-75% percentiles. The squares show galaxies where the merging pair is gravitationally affected by a third galaxy nearby (see text for details), and the circles show mergers where no other galaxies are nearby. All the properties exhibit a gradually increasing dependence on merger ratio. If we only take into account galaxies without a nearby third galaxy these results are consistent with previous idealised simulations of mergers, where $\mu > 1/3$ mergers can cause strong starbursts and $\mu < 1/3$ mergers cause more modest starbursts. A full inclusion of the cosmological environment, such as in the form of additional galaxies in the vicinity of the merger, can, however, significantly increase the SFR and decrease the gas depletion timescale of minor mergers.

6.3 Metallicity dilution and starburst properties

overlooked in previous generation's of idealised modelling of merging galaxies.

On average, minor mergers with $\mu \simeq 0.1$ cause substantial SFR-enhancements of about 0.5 dex (a factor of 3). For lower merger ratios of $\mu < 0.05$, the SFR-enhancements are more modest, in most cases lower than a factor of 2. In idealised simulations, [Cox et al. \(2008\)](#) found the same conclusions; their merger with $\mu = 0.02$ causes an almost negligible SFR-peak, whereas their $\mu = 0.1$ merger causes a more visible – but still small – SFR-enhancement.

For the metallicity, the strength of the dilution increases gradually until $\mu \sim 1$, where the peak dilution is around 0.17 dex. We thus confirm the idealised simulations from [Torrey et al. \(2012\)](#), which also show that metallicity dilution occurs in the centre of galaxies. The magnitude of the dilution in our work is slightly larger than the maximum dilution of ~ 0.05 dex observed in [Scudder et al. \(2012\)](#) for galaxies being ~ 11 kpc apart. However, there are several possible explanations for this discrepancy: first, their selection criteria for galaxy pairs do not guarantee that these systems are strictly interacting galaxies; therefore, when non-interacting systems are included, the real extent of the metallicity dilution would be likely underestimated. Second, we are reporting values near to or at the coalescence time, when the dilution is supposedly strongest¹. This time corresponds to small projected distances $\lesssim 5$ kpc, which are more challenging to probe observationally. Finally, due to their weaker dilutions, they do not split the metallicity offsets into different merger ratio bins, even including merger ratios above one, i.e. they also use the secondary galaxies. When we do the same, we obtain a more modest median metallicity dilution of 0.08 dex, which is in better agreement. Overall, establishing the presence of metallicity dilution in cosmological simulations is an interesting finding as it shows that tidal forces and gravity torques exerted during more realistic mergers are mechanisms capable of driving enough nuclear gas inflows to produce metallicity dilution and SFR-enhancement, even in minor mergers, albeit at a lesser extent.

Epochs of very strong gas compression mostly appear when the merger ratios are high, see the median curve in the $(\mu, \Delta \log \tau_{\text{SFR}})$ -plot. A similar bursty mode for major mergers is also found in the hydrodynamical simulations of [Renaud et al. \(2014\)](#) and [Sparre & Springel \(2016\)](#). The same plot also shows that $\mu \simeq 0.3$ is a characteristic scale above which the average τ_{SFR} -value experiences a decrease of ~ 0.3 dex (a factor of 2) during a merger. Moreover, four of the mergers in the same range ($\sim 30\%$) exhibit even larger decreases of 0.5 dex up to 0.8 dex. Therefore, using $\mu \simeq 0.3$ as a threshold to distinguish major and

¹Major mergers seem to be an exception to this. See Figure 6.4.

6. MERGER-INDUCED METALLICITY DILUTION IN SIMULATIONS

minor mergers captures whether bursty epochs with short τ_{SFR} -values are likely to occur.

Finally, we quantify the fluctuations of SFR, metallicity and depletion timescale in isolated galaxies. In order to do so, we have implemented the same algorithm used for finding the peaks and dips associated to SFR-enhancements and metallicity dilution in mergers. For example, in the case of SFR, we find all the local maxima of a galaxy whenever it is marked as isolated according to our merger selection criteria. Then, for each maximum, we find the local minimum that occurs right before the time of the maximum. With these two values we quantify the fractional change of the fluctuation. For metallicity and depletion timescale, we apply an analogous procedure. We show in every panel the mean value of the fractional change of these fluctuations as green dashed lines. Mergers with small stellar mass ratios (i.e. $\mu < 1/30$) exhibit fractional changes comparable to the fluctuation levels of isolated galaxies, which is consistent with the idea of very minor mergers not driving gas inward.

6.3.3 Projected distance

In Figure 6.4 we have determined the SFR, the metallicity and the projected distance as the merging galaxies from our sample approach each other for three different mass ratio bins. The projected distance corresponds to the projection on the XY plane of the merger orbit, which means that we assume only one viewing direction per merger. Metallicity dilutions and SFR-enhancements are measured relative to the pre-merger values at $t_{Z_{\text{max}}}$ and $t_{\text{SFR}_{\text{min}}}$, respectively. Since we only have snapshots of our galaxies at a relatively sparse temporal frequency, it is not always the case that each galaxy merger is represented in every radial bin. In such a case, these galaxy mergers get a vanishing weight in those bins. Furthermore, a few mergers exhibit more complex orbits, causing their trajectories to be counted more than once in some radial bins. We evenly distribute the weights of multiple points of a given galaxy within a radial bin such that the sum of the weights is one. The final median profile is obtained by stacking all the trajectories with the proper weights in every radial bin. Besides, we include data points at $r = 0$ corresponding to values at the coalescence time. Finally, to simplify comparison with the results reported by [Scudder et al. \(2012\)](#), our error bars also correspond to the standard error of the median.

The fractional changes near coalescence are stronger for larger mass ratios. For major mergers, the SFR-enhancement becomes significant at projected distances $r < 30$ kpc, whereas the metallicity dilution becomes noticeable at slightly larger distances $r < 40$ kpc. This difference is caused by merger-induced gas inflows diluting firstly the metals,

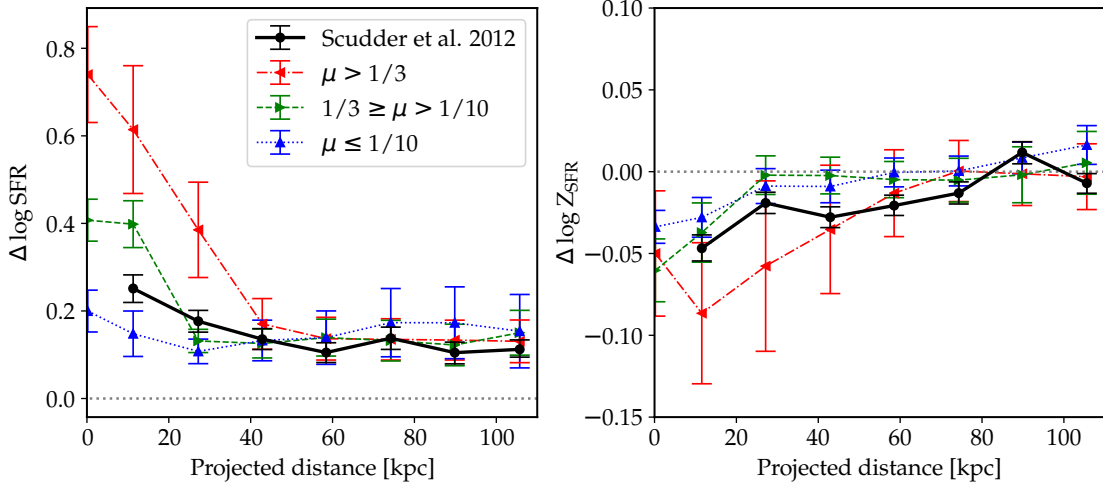


Figure 6.4: Fractional change of the SFR (left panel) and the metallicity (right panel) as a function of projected distance for our sample of galaxies (dashed lines) and the observations of Scudder et al. 2012 (solid lines). The error bars show the standard error of the median. The observed sample shows SFR-enhancement at $r < 40$ kpc and metallicity dilution at $r < 60$ kpc. For our simulated sample, major mergers show SFR-enhancement at $r < 30$ kpc and dilution at $r < 40$ kpc. For minor mergers, SFR-enhancement and dilution occur at the same distances, within $r < 30$ kpc. The fractional changes are progressively stronger for larger mass ratios and smaller distances, with the exception of major mergers, where the dilution peak occurs at a distance ~ 10 kpc, which is slightly increasing with the coalescence time. This is caused by stellar metal enrichment overcoming the dilution.

6. MERGER-INDUCED METALLICITY DILUTION IN SIMULATIONS

and soon after producing a strong SFR-enhancement as a result of gas compression in the galactic centre. The magnitude of this process is also revealed by the slight increase of the metallicity at the coalescence time, caused by stellar metal enrichment starting to overcome the dilution. For minor mergers, both effects become significant at comparatively smaller distances, for $r < 20$ kpc. A smaller distance of influence is expected from the modest gravitational influence of smaller galaxies. Due to weaker gas inflows in this case, the SFR-enhancement and the metallicity dilution sync up, with stellar metal enrichment overcoming the dilution only after coalescence.

Finally, we compare with the observations of [Scudder et al. \(2012\)](#). At large projected distances the SFR-enhancements exhibit a similar behaviour, although their metallicity dilution is lower than ours. The reason for the differences is probably the different adopted normalisations. While they use a carefully selected control sample from which the fractional changes are calculated, we use pre-merger values due to our limited number of galaxies. At smaller distances, their values sit between our major and minor mergers, consistent with the mixed merger ratios in the sample that they use. Taking these considerations into account we regard our simulations as consistent with the [Scudder et al. \(2012\)](#) observations. Our results also agree with the idealised simulations of [Patton et al. \(2013\)](#), who reproduced the observed trend from [Scudder et al. \(2012\)](#).

6.4 Mergers and the Fundamental Metallicity relation

In this section we characterise how mergers are positioned relative to the fundamental metallicity relation (FMR). In order to do so, we show in the left panel of [Figure 6.5](#) the three-dimensional distribution of 1577 data points representing our galaxies in both isolated and merging phases. For each simulation we study all galaxies in 60 snapshots logarithmically distributed in the redshift range $0 \leq z \leq 1.5$. The blue wireframe corresponds to a second-order polynomial in M_* and SFR fitted to the metallicity values, yielding:

$$\begin{aligned} \log(Z_{\text{gas}})_{\text{FMR}} = & 0.471 + 0.549 m - 0.214 s - 0.099 m^2 \\ & + 0.010 m s + 0.007 s^2, \end{aligned} \quad (6.2)$$

where $m \equiv \log(M_*) - 10$ and $s \equiv \log(\text{SFR})$, with Z_{gas} , M_* and SFR in units of Z_{\odot} , M_{\odot} and $M_{\odot} \text{yr}^{-1}$, respectively. With the aim of testing the goodness of fit of this model, in the bottom panel of [Figure 6.5](#) we calculate the histogram of residuals $r \equiv \log(Z_{\text{gas}})_{\text{data}} -$

6.4 Mergers and the Fundamental Metallicity relation

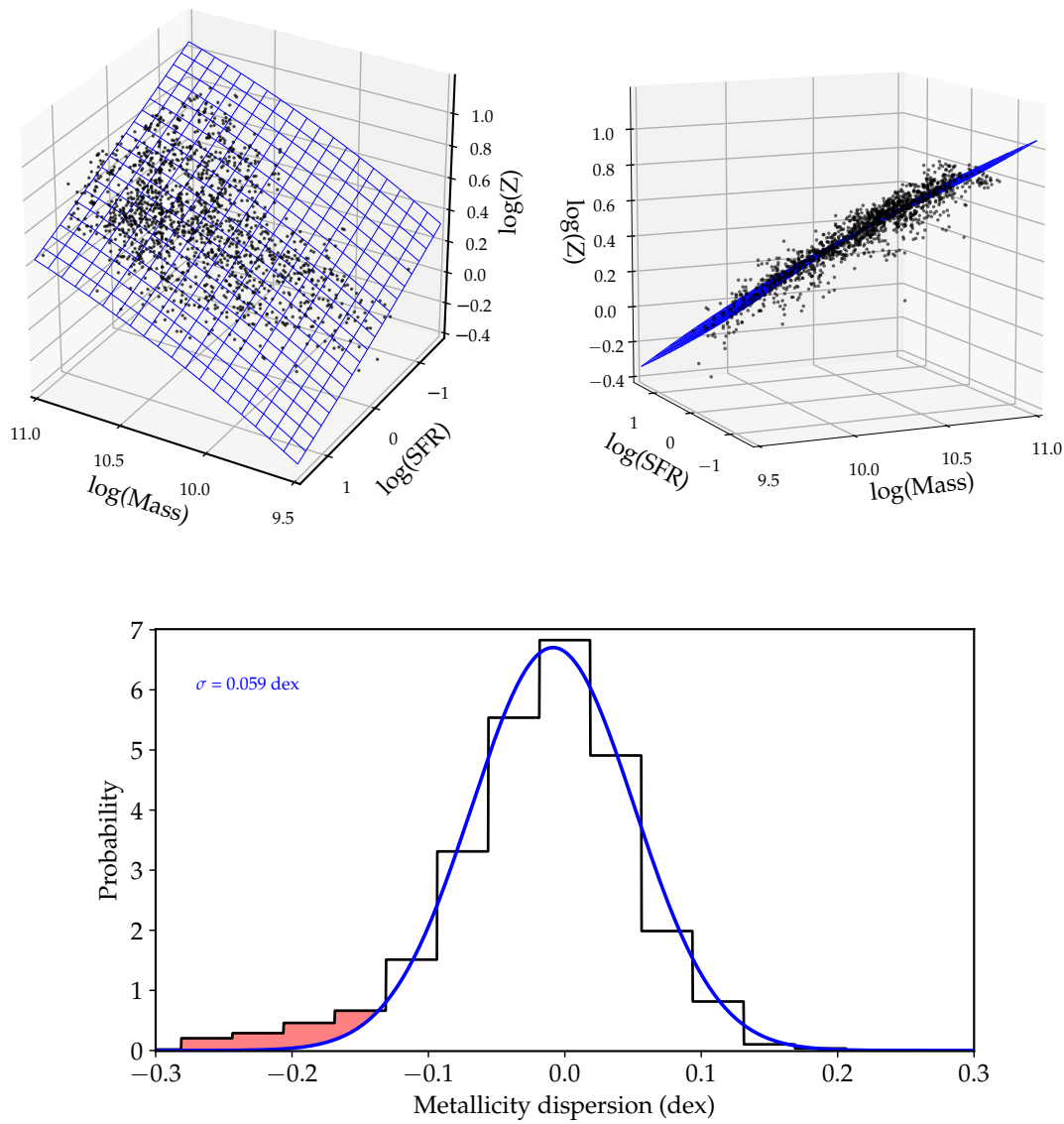


Figure 6.5: *Top panels:* two projections of the distribution of simulated galaxies at different times in the three-dimensional space of stellar mass–SFR–metallicity. The blue wireframe shows a second-order polynomial fitted to the data. *Bottom panel:* Normalised histogram of residuals around the fitted surface. We highlight the overabundance of low-metallicity outliers with a red shaded region. The blue line corresponds to a fitted Gaussian distribution function. The dispersion is similar to the value $\sigma = 0.053$ dex found by [Mannucci et al. \(2010\)](#) for their galaxy sample, which indicates a similar level of consistency of our simulated galaxies with a FMR.

6. MERGER-INDUCED METALLICITY DILUTION IN SIMULATIONS

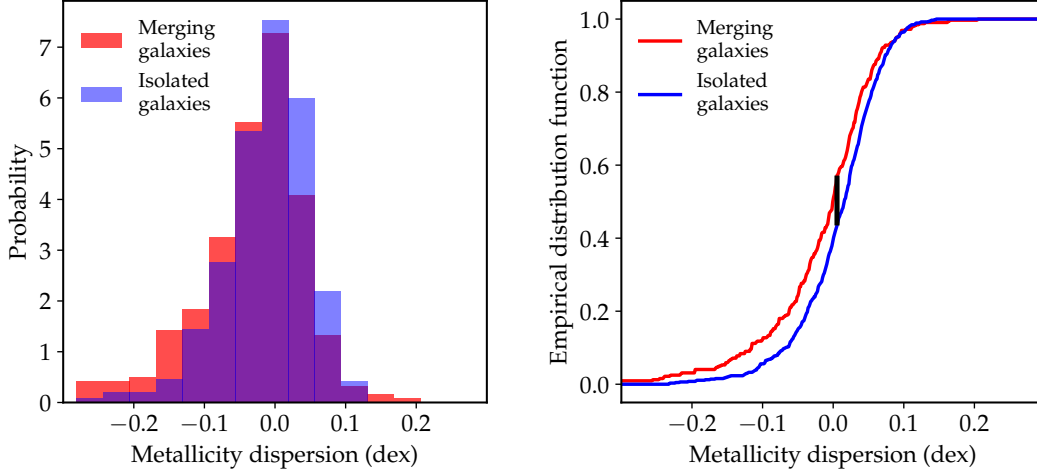


Figure 6.6: *Left panel:* Normalised distributions of residuals of isolated galaxies (blue) and merging galaxies (red) with respect to the FMR. Merging galaxies have a more distinct tail towards low metallicities than isolated galaxies. *Right panel:* Empirical cumulative distribution functions for isolated and merging galaxies. Applying a Kolmogorov-Smirnov test, both distributions differ at a confidence level of $\alpha = 0.1\%$, which is good enough to affirm that isolated and merging galaxies follow different evolutionary trends.

$\log(Z_{\text{gas}})_{\text{FMR}}$, using 16 bins with a width of 0.04 dex. The metallicity dispersion is almost a Gaussian distribution, but with a noticeable tail towards lower metallicity values, as also noted in [Mannucci et al. \(2010\)](#) and [Grønnow et al. \(2015\)](#). We fit a Gaussian distribution function using least squares, which yields an offset $\mu = 0.009$ dex and a standard deviation $\sigma = 0.059$ dex, which is very similar to the observed values of $\sigma = 0.053$ dex and $\sigma = 0.048$ dex for SDSS galaxies found by [Mannucci et al. \(2010\)](#) and [Grønnow et al. \(2015\)](#), respectively. This shows that both observed and simulated galaxies exhibit a similar level of consistency with the evolution encoded in the FMR.

6.4.1 Distribution of mergers

[Mannucci et al. \(2010\)](#) proposed that strong low-metallicity gas inflows triggered during a merger are a plausible scenario to explain the tail of low-metallicity galaxies in the metallicity distribution. More recently, [Grønnow et al. \(2015\)](#) proposed a sophisticated model to infer different properties of mergers – merger ratios, metallicity dilutions and characteristic timescales – from the distribution of residuals and the overabundance of outliers, showing

also consistency with this scenario.

In order to study how merging galaxies are distributed with respect to the FMR, we opt to follow a different approach. Instead of trying to directly quantify the overabundance of outliers, which strongly depends on the number of merging systems included in the sample, we calculate and compare the normalised distributions of residuals for isolated and merging galaxies. To do so the isolated phases of a galaxy are determined according to the sample in Section 6.2.3.

In the left panel of Figure 6.6 we show the normalised distribution of residuals. First, we note that merging galaxies exhibit a slightly higher probability to have lower than average metallicity values compared with their isolated counterparts. Moreover, they show a more distinct tail in the low-metallicity end, consistent with a merger-induced overabundance of outliers in the global distribution of residuals. The distribution of isolated galaxies also exhibits a somewhat smaller tail, which might be due to numerical issues related to our isolation criterion, or have a more physical origin; namely very minor mergers ($\mu < 1/100$), long post-merger transients, or cold gas accretion.

Finally, we test how different both distributions are. We compute the empirical distribution function (ECDF) in the right panel of Figure 6.6. Then, after applying a Kolmogorov-Smirnov test, we conclude that the null hypothesis of both distributions being numerical realisations drawn from the same underlying distribution can be rejected at a confidence level of $\alpha = 0.1\%$. This is good enough to affirm that the distributions are different and that isolated and merging galaxies follow different evolutionary paths in the SFR, M_* and Z_{gas} space. We thus confirm the result from Grønnow et al. (2015) that mergers cause outliers in the FMR.

6.4.2 Evolution of mergers: stacked profiles

After establishing that merging galaxies represent a distinct population with respect to the FMR, we explore how they are evolving out of and back into the isolated phases. In Figure 6.7, we calculate the evolution of the fractional change of the SFR (top panels) and metallicity (bottom panels) for our merger sample. Each merger is normalised to its pre-merger values at $t_{\text{SFR}_{\text{min}}}$ and $t_{Z_{\text{max}}}$, respectively. The reference time is set to the coalescence time, with negative values corresponding to pre-merger stages.

In the central panels we show the median of the stacked profiles, where the shaded regions represent 25% – 75% percentile intervals. In the top-central panel we note that

6. MERGER-INDUCED METALLICITY DILUTION IN SIMULATIONS

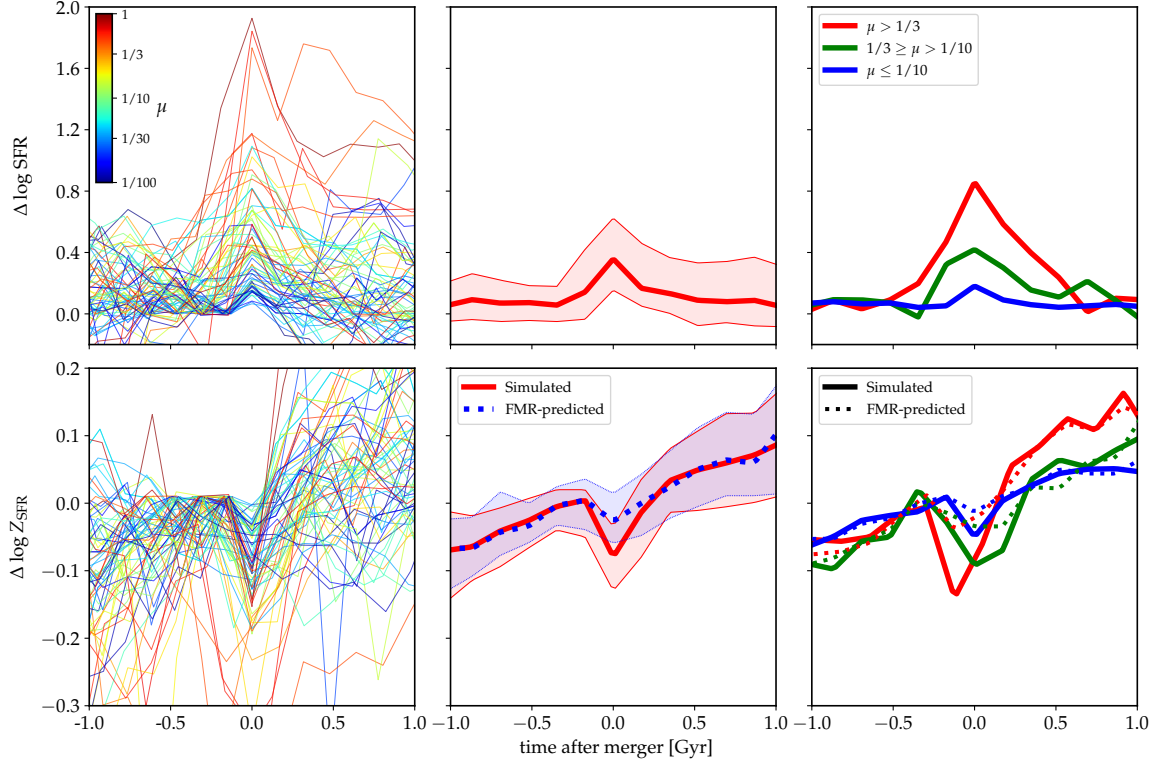


Figure 6.7: Fractional changes of the SFR (top-left panel) and metallicity (bottom-left panel) for the merger sample. Each merger is normalised to its pre-merger values at $t_{\text{SFR}_{\min}}$ and $t_{Z_{\max}}$, respectively. The x -axis shows the elapsed time since coalescence, with negative values corresponding to pre-merger stages. In the central panels we show the median of the stacked profiles, where the shaded regions correspond to 25% – 75% percentiles. In the right panels we show the median fractional changes for 3 different mass ratio bins, namely major (red), intermediate (green) and minor mergers (blue). For the metallicity, we compute the simulated and the FMR-predicted values. The latter is computed from the stellar mass and the SFR of each galaxy along with the fitted FMR of equation (6.2). Close to coalescence, we note that the simulated metallicity is always lower than the FMR prediction.

6.4 Mergers and the Fundamental Metallicity relation

galaxies in a merger start experiencing a significant SFR-enhancement at around -0.3 Gyr, reaching a peak of 0.36 dex at coalescence and then decreasing again to pre-merger values. A closer inspection in the top-right panel, where we use three different mass ratio bins corresponding to major, intermediate and minor mergers, shows that this evolution is mass-ratio dependent. For example, the SFR-peak values are 0.79 dex, 0.54 dex and 0.18 dex for each respective bin, and they all occur at coalescence time. This result is expected given the correlations presented in Figure 6.3, and also applies to the strongest metallicity dilutions seen in the bottom-central panel.

A second interesting aspect is the characteristic timescale of the enhancement. Major mergers start the SFR-enhancement period at around -0.3 Gyr up to 0.7 Gyr, i.e. over a timescale of 1 Gyr. For intermediate and minor mergers, this period goes from -0.3 Gyr to 0.5 Gyr, and from -0.2 Gyr up to 0.2 Gyr, respectively.

Now we calculate the distributions of the fractional change for the simulated and the FMR-predicted metallicities. The latter is computed from the stellar mass and the SFR of each merger along with the FMR of equation (6.2). In the bottom-central panel we see that overall the metallicity is increasing in time due to the secular evolution of the galaxy. An exception to this occurs around the coalescence time, where significant dilutions of 0.08 dex and 0.025 dex are registered in the simulated and the FMR-predicted distributions, respectively. The FMR-predicted decrease is caused because the merging SFR-enhanced galaxies naturally yield lower metallicities in the FMR relation. However, this dilution is smaller than the simulated value, thereby confirming once more that merging galaxies consist of a differentiated population.

It is interesting to note that when we look at both distributions at more distant times from coalescence, i.e. for pre- and post-merger stages, they are more similar, meaning that the evolution is again well described by the FMR. This has the interesting consequence that a direct comparison can hint when the onset and the end of the dilution take place. In the bottom-right panel we show the dilution for the different mass ratio bins. For major mergers, we find that the onset of the dilution occurs at -0.4 Gyr, i.e. 0.1 Gyr before the onset of the SFR-enhancement. A time delay of 0.15 Gyr is also seen between the strongest metallicity dilution and the SFR-peak. In general, this is consistent with the results presented in Figure 6.4 for metallicity versus distance projection, for which the dilution starts to be significant at slightly larger distances than the SFR-enhancement. The dilution ends shortly after coalescence at 0.2 Gyr, while the SFR-enhancement is still significantly high. About 0.5-0.7 Gyr after the end of the dilution, the SFR reaches pre-merger values and the enhancement is

6. MERGER-INDUCED METALLICITY DILUTION IN SIMULATIONS

over. During this period of time, the stellar enrichment is able to compensate the inflow of low-metallicity gas, placing the metallicity again close to the FMR-prediction.

For smaller merger ratios the metallicity dilution occurs at nearly similar times as the SFR-enhancement, with both having almost the same timescales (see also [Torrey et al., 2018](#)). This implies that the stellar enrichment from SF activity is less efficient at compensating gas inflows than in major mergers, and the dilution only ends when the infalling gas supply is dimmed after the merger process is completed.

Metallicity dilution and SFR-enhancement timescales have been previously reported in hydrodynamical simulations of merging galaxies by [Montuori et al. \(2010\)](#). They study 1:1 gas rich mergers and find a timescale of 1.5 Gyr for both processes. Our SFR-enhancement timescale of 1 Gyr for major mergers is consistent with their result, although our dilution timescale is considerably shorter. A plausible explanation for this discrepancy is that their galaxies are more gas-rich, with gas fractions of 20% compared to 9 – 16% for our galaxies. This, along with the higher mass ratio, might cause significantly stronger low-metal gas inflows in their simulations, hence the stellar enrichment during the SFR-enhancement cannot overcome the dilution, resulting in both processes having similar timescales.

6.5 Discussion

Based on idealised merger simulations where two composite model galaxies collide on a Keplerian orbit, it has previously been suggested that *wet mergers* can be sensibly divided into two categories; minor and major mergers. The merger mass ratios defining these two classes are typically taken to be $1/10 < \mu < 1/3$ and $\mu > 1/3$, respectively. The former mass-ratio reflects the limit below which a negligible SFR-enhancement arises, and the latter reflects the threshold above which a strong SFR-peak occurs. Furthermore, it has been established that major mergers also consume their gas on shorter timescales than minor mergers (e.g. [Cox et al., 2008](#)). In our cosmological simulations we confirm that stronger SFR-peaks and shorter gas consumption timescales occur for major mergers compared to minor mergers. We additionally show that a strong metallicity dilution occurs for major mergers, whereas for minor mergers the effect is more modest. We advocate that merger-induced metallicity dilution is an important addition to the standard picture of the behaviour of wet mergers. Aside from our own simulations, this is also supported by those of [Torrey et al. \(2012\)](#) and [Torrey et al. \(2019\)](#). Furthermore, this effect is seen in the observations of [Scudder et al. \(2012\)](#).

Observers have for more than half a decade advocated the existence of the FMR, and recently several hydrodynamical galaxy formation simulations have reproduced this relation (Lagos et al., 2016; De Rossi et al., 2017; Davé et al., 2017; Torrey et al., 2018). The effect of merger-induced metallicity dilution has important consequences for the FMR, because mergers are expected to produce a low-metallicity tail in the residuals around the FMR. This result has been seen in analysis of the observations of Grønnow et al. (2015) and is also visible in our simulations.

In the present chapter, we have focused on the effect of gas flows in the central parts of galaxies. Several questions which can be addressed in future research arise from this work. It would for example be interesting to study gas flows by using *Lagrangian gas tracer particles* (for a study of gas tracers within our simulation framework, see Genel et al., 2013) to quantify how the gas is redistributed within a galaxy in a merger. This would specifically make it possible to estimate to what extent gas is moved between the core of a galaxy, the disc and the circumgalactic medium. Furthermore, it would be possible to study gas accretion from outside the galaxy in detail. In our current set of merger simulations we have not included such gas tracer particles, but in future simulations we plan to do so.

6.6 Conclusion

In this chapter we study cosmological simulations of *wet mergers* of main progenitor galaxies with masses in the range $5 \times 10^9 M_\odot < M_* < 2 \times 10^{11} M_\odot$ from the Auriga simulation suite. Our sample of mergers is much larger than what has been typically used in studies of idealised merger simulations, and with our full cosmological setup we furthermore have more realistic structure, encounter orbits and environment of our galaxies. Our main results are:

- We confirm the result from idealised simulations that strong starbursts occur in major mergers with a mass-ratio larger than $\mu > 1/3$. For minor mergers with $1/10 < \mu < 1/3$ there is typically a smaller, but still clearly visible SFR enhancement. Exceptions do, however, occur when several galaxies are involved in the minor merger; in this case the SFR can also increase by an order of magnitude. We note that this scenario, which happens at least occasionally for galaxies in the real Universe, has not been properly explored in previous generations of idealised merger simulations.
- An increased merger ratio also causes a shorter gas consumption timescale, i.e. more

6. MERGER-INDUCED METALLICITY DILUTION IN SIMULATIONS

bursty star formation. We furthermore find that a low-metallicity epoch is typically associated with a merger. The magnitude of the metallicity dilution is strongest for major mergers. Our cosmological simulations thus confirm the occurrence of metallicity dilution, which has previously been seen in observations of merging galaxies and in idealised merger simulations. We consider the period of metallicity dilution as an equally characteristic feature of major mergers as the increased SFR and decreased gas consumption timescale.

- During the epoch of metallicity dilution mergers have lower metallicity than predicted by the *fundamental metallicity relation* (FMR). This creates a tail of low-metallicity galaxies offset from the FMR. Consistent with findings for observed galaxies the residuals around the FMR indicate that there are more galaxies with low metallicity than predicted by a Gaussian distribution of the residuals. At least part of this effect can be attributed to galaxy mergers.

Merger-induced metallicity dilution in SDSS galaxies

In this chapter, we analyse the process of SFR enhancement and metallicity dilution in observed interacting galaxies from the SDSS. This work will be soon submitted for publication to the journal of the Monthly Notices of the Royal Astronomical Society.

7.1 Introduction

The cycle of life and death of stars leads to a steady enrichment of heavy elements in the interstellar medium (ISM), and together with processes such as accretion of low-metallicity gas from reservoirs around galaxies and gas outflows induced by stellar and AGN feedback, yields a correlation between the stellar mass (M_*) and the metallicity¹ of the star-forming gas (Tremonti et al., 2004). However, the scatter of the relation is significant (~ 0.1 dex; Tremonti et al., 2004), which means that galaxies, although building up their content of heavy elements gradually and steadily during most of their lifetime, are also evolving on diverse pathways through the stellar mass-metallicity plane.

If the role of stellar feedback is important in regulating the metal content of the ISM, and gas infall drives star formation activity, a secondary dependence on the SFR is expected

¹Throughout this chapter, the term *metallicity* will be employed to refer to the gas-phase metallicity, unless otherwise stated.

7. MERGER-INDUCED METALLICITY DILUTION IN SDSS GALAXIES

in the mass-metallicity relation. This was first discovered by [Ellison et al. \(2008a\)](#), where a weak dependence on the specific SFR (SSFR) was found for SDSS galaxies. This relation is often dubbed the *fundamental metallicity relation* (FMR). More recent studies have also confirmed the presence of the FMR, both in observations ([Mannucci et al., 2010](#); [Lara-López et al., 2010](#); [Belli et al., 2013](#); [Stott et al., 2013](#); [Yabe et al., 2015](#)) and simulations ([Lagos et al., 2016](#); [De Rossi et al., 2017](#); [Davé et al., 2017](#); [Torrey et al., 2019](#); [Bustamante et al., 2018](#)). However, it is still debated whether the FMR is *fundamental*, i.e. whether it is redshift independent and universal. Several observations at $z \sim 2.3$ have revealed differences from the FMR in the local Universe ([Salim et al., 2015](#); [Grasshorn Gebhardt et al., 2016](#); [Brown et al., 2016](#); [Sanders et al., 2018](#)). [Sanders et al. \(2018\)](#) suggest that the redshift-dependence of the FMR can be explained by an evolution of the metallicity of infalling gas and the mass-loading factor at fixed stellar mass. [Ellison et al. \(2011\)](#) find that barred galaxies have both high SFRs and high metallicities, which is opposite to the FMR expectations. This suggests that there are at least some galaxy populations that do not follow the FMR.

Although the FMR might have a redshift-dependence, [Dayal, Ferrara & Dunlop \(2013\)](#) have proposed a simple analytical model to explain its overall shape. Specifically, they find that the local FMR is driven by star formation, inflow of metal-poor gas from the intergalactic medium, and outflow of gas from the interstellar medium. Interestingly, the shape of the FMR predicts that galaxies, at a fixed stellar mass, exhibit lower metallicities for higher SFRs. This is qualitatively in good agreement with observations of galaxy pairs, in which systematic offsets towards lower gas-phase metallicities and higher SFRs with respect to control samples of isolated galaxies have been previously reported ([Ellison et al., 2008b](#); [Scudder et al., 2012](#); [Cortijo-Ferrero et al., 2017](#); [Thorp et al., 2019](#)). This is also supported by numerical studies, in which metallicity dilution and SFR enhancement have been shown to take place in interacting galaxies as a result of merger-induced nuclear inflows ([Torrey et al., 2012](#); [Hani et al., 2018](#); [Bustamante et al., 2018](#)).

Nevertheless, a more careful statistical analysis of SDSS galaxies has revealed an overabundance of low-metallicity outliers in the FMR compared to a Gaussian distribution of residuals. For example, [Grønnow et al. \(2015\)](#) conclude that interacting galaxies might be at the origin of this population of outliers, as strong merger-induced nuclear inflows might cause substantial metallicity dilutions that are largely underestimated by the FMR. [Bustamante et al. \(2018\)](#) (B18 henceforth) have used a set of cosmological zoom-in simulations to show that the FMR does not describe the evolutionary phases of merging galaxies,

including post-merger stages. All of this further supports the idea that the FMR is not fundamental in general, and that mergers in particular may be outliers.

In this chapter, we study the metallicity dilution and SFR enhancement of galaxy pairs and post-merger galaxies from the Sloan Digital Sky Survey Release 7 (SDSS DR7; [Abazajian & et al. 2009](#)). We use the galaxy pairs compiled by [Patton et al. \(2016\)](#) and the post-merger galaxies compiled by [Ellison et al. \(2013\)](#). We construct statistical control samples following the procedure proposed by [Patton et al. \(2016\)](#), i.e. matching simultaneously in stellar mass, redshift, local density and isolation. This allows us to quantify differences between pairs and post-mergers and their respective control samples over a wide range of mass ratios, projected separations and environments. Additionally, we fit a FMR to our whole galaxy sample in order to compare the predicted metallicity dilution and SFR enhancement to the observed values in galaxy pairs and post-mergers.

This chapter is structured as follows. In Section 7.2, we present our sample selection and the matching algorithm for the control galaxies. In Section 7.3, we fit a FMR to our galaxy sample and quantify the differences between the predicted and observed values of the metallicity dilution and the SFR enhancement for galaxy pairs and post-merger galaxies. Furthermore, we study the dependence of these processes on the stellar mass ratio and the local environment. Finally, we discuss our results and conclude in Section 7.4 and 7.5, respectively. Throughout this work, we adopt a concordance cosmology with $\Omega_\Lambda = 0.7$, $\Omega_M = 0.3$ and $H_0 = 70 \text{ km s}^{-1} \text{ Mpc}^{-1}$.

7.2 Sample selection

7.2.1 Galaxy sample

In the following, we describe the selection criteria applied to construct our general sample of galaxies, from which we also compile the samples of galaxy pairs, post-merger galaxies and controls. Our starting point is the spectroscopic pool of galaxies in the SDSS DR7. Following [Patton et al. \(2013\)](#), we select galaxies with reliable spectroscopic redshifts (redshift confidence of $z\text{Conf} > 0.7$) and extinction-corrected r -band Petrosian apparent magnitudes in the range of $14.0 \leq m_r \leq 17.77$. The redshift range is limited to $0.005 < z < 0.2$ in order to avoid spurious effects from the extremes of the redshift distribution. Each galaxy must have a reliable estimate of the total stellar mass from [Mendel et al. \(2014\)](#).

Due to our interest in studying merger-induced effects on the SFR and the metallicity,

7. MERGER-INDUCED METALLICITY DILUTION IN SDSS GALAXIES

we focus on those galaxies with reliable measurements of these quantities. For the SFR, we further select galaxies that are included in the MPA catalogue, which is calculated according to the [Brinchmann et al. \(2004\)](#) work. Additionally, we select only galaxies that are classified as star-forming using the criteria defined by [Kauffmann et al. \(2003\)](#). For the metallicities, we use the values reported by [Scudder et al. \(2012\)](#), which are computed using the adaptation of the [Kewley & Dopita \(2002\)](#) method presented in [Kewley & Ellison \(2008\)](#). An additional redshift cut of $z > 0.02$ is performed in order to guarantee that all the emission lines used in the metallicity calibration are within the spectral range of the SDSS. We refer the reader to [Scudder et al. \(2012\)](#) for more details. Finally, we use the method presented in [Brinchmann et al. \(2004\)](#) to correct the Sloan 3 arc-second fibre quantities to total values. The method is based on a fit to the photometry of the galaxy outside the fibre, thus taking into account light that is not contained within the region mapped by the fibre. We use total quantities throughout this work.

For a given galaxy, the effects caused by the interaction with a close companion are in clear competition with environmental effects induced by the galaxy surroundings. Due to this reason, if one wants to understand the influence that the close companion has on the SFR and the metallicity, it is important to properly characterise both, the galaxy's closest companion and its host environment. In order to do so, we characterise the closest potential companion of each galaxy by using the projected physical separation r_p , the rest-frame line-of-sight relative velocity Δv and the stellar mass ratio (companion-to-main galaxy stellar mass ratio) μ . For the environment, we follow the approach presented in [Patton et al. \(2016\)](#), i.e. we use two different metrics to characterise a galaxy's environment: first, the total number of detected spectroscopic companions within a projected separation of $2 h^{-1} \text{ Mpc}$, N_2 . The second metric is the projected separation to the galaxy's second closest companion, r_2 . All the relevant galaxy's companions must satisfy that their rest-frame line-of-sight velocity Δv is within 1000 km s^{-1} relative to the galaxy in question and that their corresponding stellar mass ratio is $\mu > 0.1$, i.e. the total stellar mass of the companion is at least 10% of the stellar mass of the main galaxy. The combination of these two metrics allows us to distinguish between different types of environments. We roughly classify them into four categories: compact groups ($N_2 < 15$ and $r_2 < 150 h^{-1} \text{ kpc}$), galaxy clusters ($N_2 \geq 15$ and $r_2 < 150 h^{-1} \text{ kpc}$), loose groups ($N_2 \geq 15$ and $r_2 \geq 150 h^{-1} \text{ kpc}$) and low density fields ($N_2 < 15$ and $r_2 \geq 150 h^{-1} \text{ kpc}$). We refer the reader to [Patton et al. \(2016\)](#) for more technical details and a through discussion on environment classification. After applying all the previous criteria, we end up with 68942 galaxies in our general sample.

7.2.2 Pair sample

Although each galaxy in our general sample has a detected closest companion, if one wants to build a sample of galaxy pairs, it would be ideal that each companion has an appreciable physical influence on the galaxy in question, i.e. the pairs are not a projection artifact. In order to minimise the presence of projection artifacts, we impose the following conditions: the stellar mass of the companion is at least 10% of the stellar mass of the main galaxy, i.e. $\mu > 0.1$; less massive companions are likely to exert effects that are too small to be observed. Note that this criterion also allows companions that are more massive, i.e. $\mu > 1$. The second condition restricts the relative rest-frame line-of-sight velocity Δv to be within 300 km s^{-1} of the main galaxy, thereby excluding galaxies with unrelated background and foreground companions (Patton et al., 2000). This velocity cut is fairly standard and has been used in previous studies of galaxy pairs (Ellison et al., 2008b; Scudder et al., 2012; Patton et al., 2016).

Another observational artifact that needs to be accounted for is fibre collisions. This effect is originated by the finite size of the SDSS fibres, which causes an underselection of galaxy companions with angular separations below 55 arcsec . We follow the approach presented by Patton et al. (2002), i.e. a statistical weight of $w_\theta = 3.08$ is applied to close angular pairs ($< 55 \text{ arcsec}$) to compensate for the sample incompleteness. Another method commonly adopted to correct for this is a random culling of 67.5% of the pairs with separations $> 55 \text{ arcsec}$ (see for example Ellison et al. (2008b)); however, this drastically reduces the sample size. After applying all the previous criteria, our sample of pairs comprises 7514 main galaxies.

7.2.3 Post-merger sample

For the post-merger galaxies, we use the sample presented in Ellison et al. (2013). This sample is compiled from the post-merger catalogue of Darg et al. (2010), which comprises 358 galaxies. The catalogue is based on a visual classification performed by the Galaxy Zoo project on SDSS galaxies and takes into account the presence of tidal features, strong irregularities, and signs of recent interaction. Ellison et al. (2013) applied additional criteria to filter out irregular galaxies without signs of a recent interaction and galaxies that are undergoing a merger, but have not fully coalesced, e.g. a companion can still be detected. The final filtered sample comprises 97 galaxies.

7. MERGER-INDUCED METALLICITY DILUTION IN SDSS GALAXIES

7.2.4 Control samples

Our main objective is to study the influence of mergers on the metallicity and star formation rate of SDSS galaxies. Given that for individual system observations can only probe a single point in time, we must adopt a statistical approach to the problem. To this end, we use two control samples of isolated galaxies as a comparison point to quantify deviations in galaxy pairs and post-merger galaxies, respectively. In order to construct the control samples, we follow the procedure presented by [Patton et al. \(2016\)](#), i.e. 10 control galaxies are simultaneously matched in stellar mass, redshift and environment for every merger and post-merger galaxy.

Star forming galaxies follow two relationships that have been extensively studied and are now well-established; namely, the mass-metallicity relation ([Tremonti et al., 2004](#); [Ellison et al., 2008a](#)) and the SFR-stellar mass main sequence ([Noeske & et al., 2007](#); [Speagle et al., 2014](#)). These relations show that galaxies build up their heavy elements content and stellar component in a steady fashion (as it is e.g. modelled in various analytical galaxy evolution models; [Lilly et al., 2013b](#); [Mitra et al., 2015](#)) as they grow in mass. In addition, the relations also exhibit a redshift dependence, meaning that galaxies at different epochs behave differently. From the technical side, some aspects of the surveys such as sample depth, survey volume and spatial resolution also depend on redshift. All of the above highlights the importance of matching the controls in stellar mass and redshift in order to reduce selection effects.

Although the influence of a close companion on a galaxy's properties is dominant at small projected separations, at larger separations the influence exerted by other neighbouring galaxies might be comparable or even larger ([Park et al., 2007](#); [Moreno et al., 2013](#); [Sabater et al., 2013](#); [Patton et al., 2016](#)), constituting thus another source of selection effects. This is why we also match the controls in environment, i.e. local density N_2 and isolation. For the latter, we use two different conditions depending on the sample for which we want to build the controls. In the case of galaxy pairs, we require that the projected separation to the closest galaxy (r_p) of each of the controls is similar to the projected separation to the second closest companion (r_2) of the main member of the pair in question. In the case of post-mergers, we match directly in the separation to the closest galaxy (r_p) as, by definition, these systems have already coalesced.

The tolerances for each of the quantities that is being matched are taken from [Patton et al. \(2016\)](#). For the stellar mass we use 0.1 dex, which is consistent with the statistical uncertain-

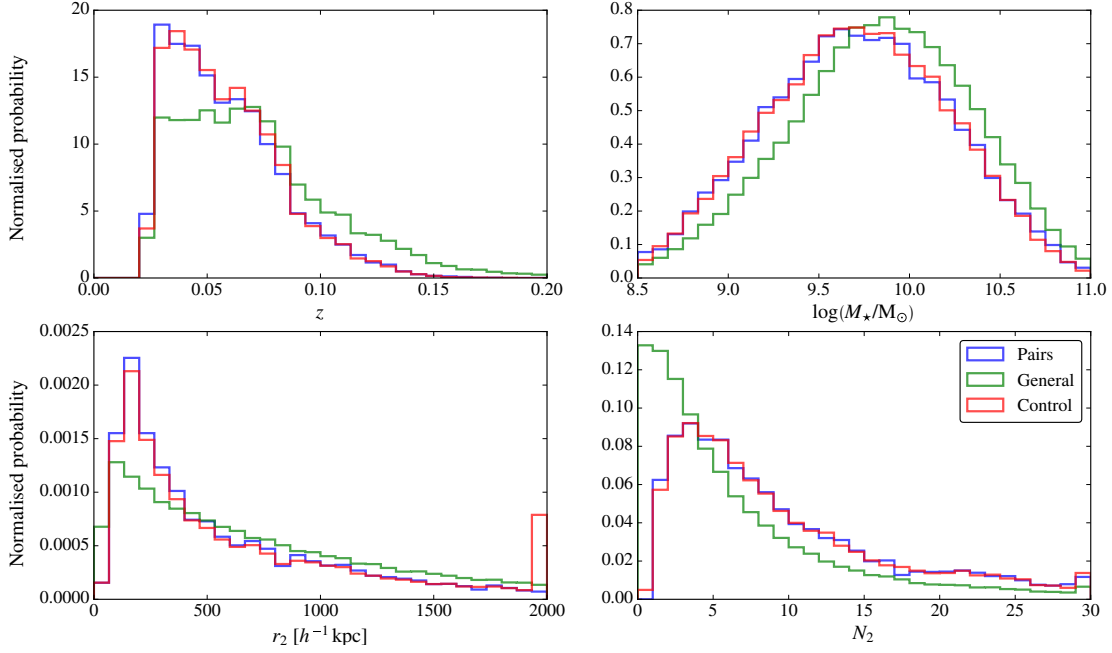


Figure 7.1: Normalised histograms of redshift (*top left*), stellar mass (*top right*), r_2 (*bottom left*) and N_2 (*bottom right*) for the galaxy pairs (blue). We also show the histograms for the general sample (green) and the controls (red). The distributions of the matching properties for galaxy pairs and their weighted controls are very well in agreement, with the only exception occurring at the high-end of the distribution of r_2 . The reason for this is explained in the text. In the *bottom left* panel, the histograms for the general sample and the controls denote r_p (rather than r_2), since this is the quantity that is matched to the paired galaxy r_2 values.

ties from measurements. For the redshift, the controls are required to agree to within 0.01 with respect to the reference sample. Finally, for matching controls in environment, both quantities, N_2 and r_p , are required to be within 10% of the value of the reference sample – r_2 for galaxy pairs and r_p for post-mergers when matching in isolation. This procedure gives at least 10 control galaxies for 62% of the galaxy pairs and 45% of the post-merger galaxies. We increase iteratively all the tolerances by a factor of 1.5 until we match at least 10 control galaxies for each of the remainders of the samples. Note that we are not excluding the case in which a galaxy might qualify as a control for multiple pairs and/or post-mergers.

In order to select the best 10 matches for each galaxy, we adopt the weighting scheme used by [Patton et al. \(2016\)](#). For example, for the redshift of the i -th control galaxy, we define the corresponding weight as:

$$w_{z_i} = 1 - \frac{|z - z_i|}{z_{\text{tol}}}, \quad (7.1)$$

7. MERGER-INDUCED METALLICITY DILUTION IN SDSS GALAXIES

where z corresponds to the redshift of the galaxy for which the control is being matched. Analogous weights are defined for stellar mass, N_2 and r_p . The global statistical weight is then given by:

$$w_i = w_{z_i} w_{M_i} w_{N_{2i}} w_{r_{2i}}. \quad (7.2)$$

We select the 10 galaxies with the highest weights as the control set of a given pair or post-merger. In Figure 7.1, we show the histograms of the sample of galaxies, galaxy pairs and their controls. In general, there is a very good agreement between the pairs and their controls, with only a deviation at the high-end of the distribution of r_2 . The disagreement comes from the fact that r_2 and r_p are capped at $2 h^{-1}$ Mpc due to limited survey boundaries, and the metric N_2 that takes into account only companions within $2 h^{-1}$ Mpc of the galaxy in question (Patton et al., 2016). In order to circumvent potential selection issues coming from this, we discard galaxy pairs for which $r_2 > 1800 h^{-1}$ kpc. This only reduces the sample size by 7%. For the post-mergers, we also find a very good agreement with their controls, and the sample size is reduced by 15% when applying the cut-off in r_p .

In consideration of the above, the statistical mean of any quantity of interest x for the control sample of a given galaxy can be computed as:

$$\bar{x} = \frac{\sum_{i=1}^{N_c} \omega_i x_i}{\sum_{i=1}^{N_c} \omega_i}, \quad (7.3)$$

where x_i is the measured quantity in the i -th control galaxy and N_c the size of the control sample.

Once the control samples have been built, we can proceed to compute the relative differences of metallicity and SFR in galaxy pairs and post-mergers. Nonetheless, there is a last issue that has to be accounted for before proceeding, i.e. spectroscopic incompleteness due to fibre collisions. This observational artifact arises as a consequence of the finite size of optical fibres used in the survey, which creates a selection effect that disfavours the detection of companions within 55 arcsec from any given galaxy. As the cosmological angular separation between two objects varies with cosmological time, this effect impacts a different range of projected separations at any given redshift. In order to correct for this, we follow the approach developed by Patton et al. (2013), in which an additional statistical weight of $\omega_\theta = 3.08$ is assigned to galaxy pairs with projected separation smaller than 55 arcsec; otherwise, $\omega_\theta = 1$. Using this scheme, the mean offset of any quantity x for a given set of N_g

galaxies with respect to their controls can be computed as:

$$\Delta x = \frac{\sum_{j=1}^{N_g} \omega_{\theta_j} (x_j - \bar{x}_j)}{\sum_{j=1}^{N_g} \omega_{\theta_j}}. \quad (7.4)$$

In Figure 7.2 we compute weighted and unweighted distributions of redshift, stellar mass, N_2 and r_2 as a function of r_p for galaxy pairs and their controls. Weighted distributions exhibit noticeable more homogeneous trends in the range $25 h^{-1} \text{ kpc} < r_p < 125 h^{-1} \text{ kpc}$, showing thus that fibre weights compensate for the deficit of close pairs.

7.3 Data Analysis

7.3.1 Fundamental metallicity relation

Our main goal is to investigate how galaxy pairs and post-mergers are positioned with respect to the FMR. In this subsection we proceed to characterise the FMR relation in our data. In order to do so, we take the general sample of SDSS galaxies, in which galaxy pairs, post-mergers and their respective controls are included, and fit a second-order polynomial in M_* and SFR to the metallicity values. The polynomial represents the FMR. There are two different approaches to fit the data: the first one consists in binning the galaxies in M_* and SFR and then computing the metallicity median value in each bin; those values are subsequently used for fitting the FMR (Mannucci et al., 2010). This approach reduces sampling issues as every bin is given the same statistical weight. The second approach is simpler and consists in fitting the FMR directly to the *raw* data (Grønnow et al., 2015). We adopt the latter, with little difference when the former is used instead. It yields:

$$12 + \log(\text{O}/\text{H})_{\text{FMR}} = 8.96 + 0.28m - 0.12s - 0.12m^2 + 0.085ms - 0.001s^2, \quad (7.5)$$

where $m \equiv \log(M_*/M_\odot) - 10$ and $s \equiv \log(\text{SFR}/M_\odot \text{yr}^{-1})$. In Figure 7.3 we show two different projections of the distribution of SDSS galaxies along with the fitted FMR. Note that for stellar masses $M_* \lesssim 10^{10} M_\odot$, the relation predicts that for lower SFRs, higher metallicity values are encountered at a fix stellar mass. Nevertheless, going along the axis of stellar mass, there is a turnover point of the relation at about $10^{10.5} M_\odot$ and an opposite trend is displayed. This is a numerical artifact that comes from the fact that galaxies with

7. MERGER-INDUCED METALLICITY DILUTION IN SDSS GALAXIES

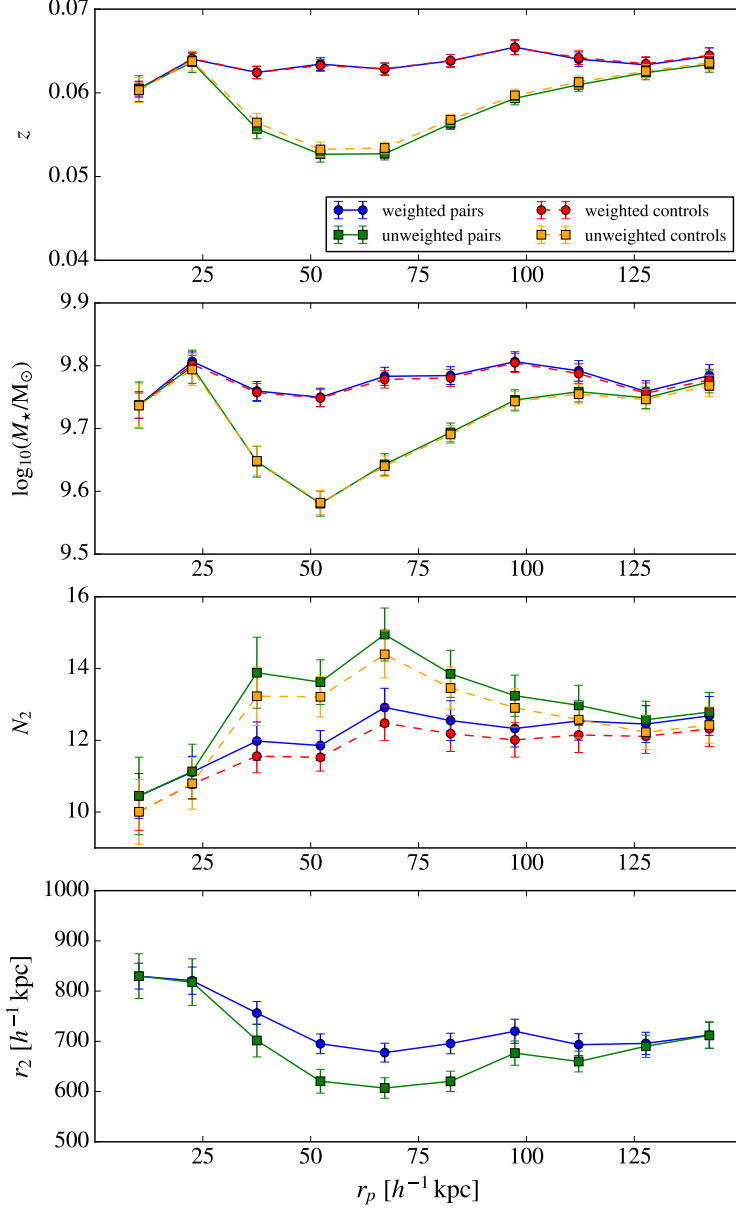


Figure 7.2: Mean redshift, stellar mass, N_2 and r_2 as a function of r_p for galaxy pairs (solid lines) and their controls (dashed lines). Error bars denote the standard error in the mean. Note that we do not show the distribution of r_2 for the controls as we match them in r_p . When comparing the weighted (circles) and unweighted (squares) distributions, the former exhibit more homogeneous trends in the range $25 h^{-1} \text{ kpc} < r_p < 125 h^{-1} \text{ kpc}$. This shows that incompleteness due to fibre collisions is properly compensated.

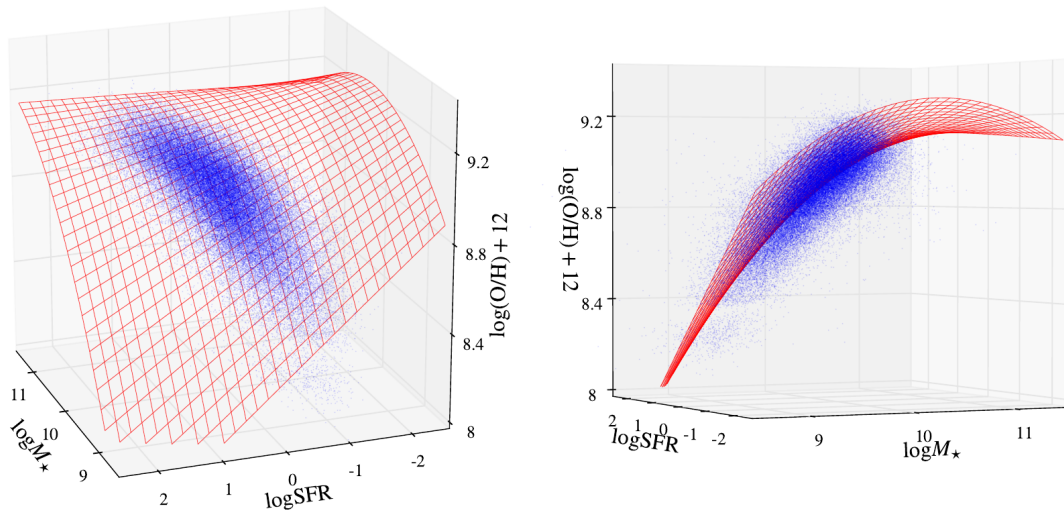


Figure 7.3: Two projections of the distribution of SDSS galaxies in the three-dimensional space of stellar mass – SFR – metallicity. The red wireframe corresponds to the second-order polynomial fitted to the data and represents the FMR.

stellar masses of $\sim 10^{10.5} - 10^{11} M_{\odot}$ show no secondary dependence on the SFR and a negative concavity of the polynomial is needed to capture this behaviour as well. This opposite trend occurs in a region that is not sampled and therefore is a mere extrapolation with no physical interpretation and does not affect our analysis. A similar numerical effect can be seen in the FMR fitted in [Mannucci et al. \(2010\)](#), shown in their figure 2.

With the aim of testing the goodness of fit of our model, represented by equation 7.5, we compute in Figure 7.4 the distribution of residuals, defined as $r \equiv \log(\text{O}/\text{H})_{\text{data}} - \log(\text{O}/\text{H})_{\text{FMR}}$. We use 100 bins with a width of 0.05 dex. Additionally, we fit a Gaussian distribution function using least squares. This yields an offset $\mu = 0.004$ dex and a standard deviation $\sigma = 0.093$ dex. Comparing with previous observational studies such as [Mannucci et al. \(2010\)](#) and [Grønnow et al. \(2015\)](#), where standard deviations $\sigma = 0.053$ dex and $\sigma = 0.048$ dex are respectively computed, we find that our standard deviation is somewhat larger. This is explained by the fact that we use the metallicity calibration of [Kewley & Dopita \(2002\)](#), whereas [Mannucci et al. \(2010\)](#) and [Grønnow et al. \(2015\)](#) use the calibration of [Maiolino & et al. \(2008\)](#) and [Marino & et al. \(2013\)](#), respectively. As shown by [Kewley & Ellison \(2008\)](#), different calibrations can lead to different values of metallicity, being discrepancies such as the one we encounter within the range of what is expected. For the sake of consistency, we also compute the stellar mass - metallicity relation for the general sample. We find, for the distribution of residuals, a standard deviation of $\sigma = 0.16$ dex, which is lar-

7. MERGER-INDUCED METALLICITY DILUTION IN SDSS GALAXIES

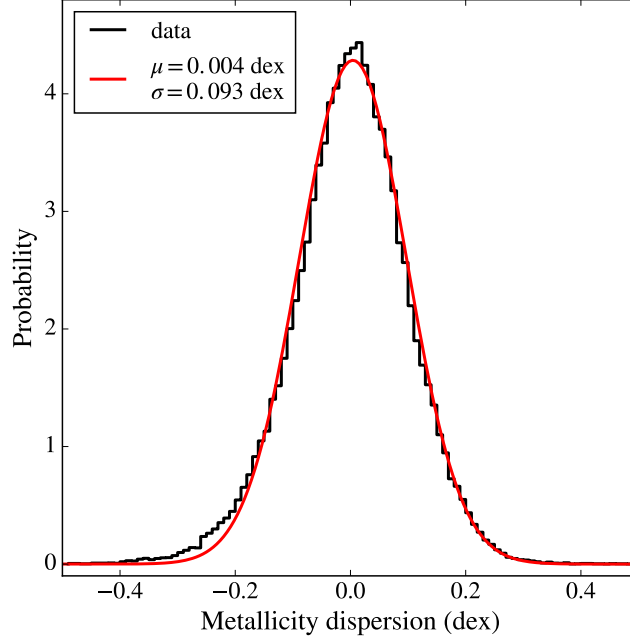


Figure 7.4: The black line represents the normalised residuals of metallicity of SDSS galaxies around the fitted FMR. The red line is a Gaussian fit with a standard deviation $\sigma = 0.093$. A clear overabundance of outliers occurs at the low-end of the distribution, approximately between -0.4 dex and -0.2 dex.

ger than the value for our fitted FMR. This demonstrates the secondary dependence of the metallicity on the SFR.

Finally, it is worth noting that the distribution of residuals in Figure 7.4 exhibits a clear overabundance of outliers with respect to the Gaussian fit between -0.4 dex and -0.2 dex. This finding is consistent with previous studies and its origin has been hypothesised to be due to the presence of interacting systems in the galaxy sample (Mannucci et al., 2010). Bearing this in mind, a direct comparison with previous works regarding the extent of the deviation from the Gaussian distribution is difficult, since the exact fraction of interacting systems in a given galaxy sample can vary significantly or even be unknown.

7.3.2 Metallicity dilution and SF enhancement

Instead of directly quantifying the overabundance of outliers in the distribution of residuals, B18 adopt an alternative approach. From a sample of simulated mergers of the Auriga project (Grand et al., 2017), the distribution of residuals and the time evolution of metallicity and SFR for isolated and interacting galaxies are directly computed and compared with

each other. This reveals that, at fixed SFR and stellar mass, interacting galaxies exhibit systematically lower metallicities compared to what is predicted by the FMR. By using the measured values of SFR, stellar mass, metallicity and projected separation of our sample of galaxy pairs and their respective controls, we follow a similar approach.

In Figure 7.5, we compute SFR and metallicity offsets for galaxy pairs as a function of projected separation. Median values, represented by blue solid lines, show a dependence of SFR enhancement and metallicity dilution on projected separation, with close pairs exhibiting larger offsets. Our trends are consistent with those previously reported by Scudder et al. (2012), e.g. metallicity dilution becomes increasingly significant at separations $r_p \lesssim 60 h^{-1} \text{ kpc}$. Our offsets at small separations are, however, somewhat weaker, i.e. 0.13 dex compared to 0.25 dex for SFR, and 0.035 dex compared to 0.048 dex for metallicity. This discrepancy might have its origin in the dependence of SFR enhancement and metallicity dilution on the pair mass ratio (see subsection 7.3.3 and Scudder et al., 2012), hence galaxy pair samples with different distribution of pair mass ratios yield different results. Furthermore, we use slightly different criteria for control matching.

Using the FMR described in equation 7.5 and the measured values of stellar mass and SFR for each galaxy pair, we compute the respective FMR-predicted metallicities. The median offsets for different bins of projected separation are shown as a green dashed line in the bottom right panel of Figure 7.5, with error bars denoting the standard error of the mean. The FMR qualitatively predicts lower metallicities for close pairs since they also have large positive SFR offsets with respect to the controls. Nevertheless, a closer inspection reveals that, at small separations, the FMR-predicted metallicity offsets are smaller than measured offsets. At intermediate projected separations $60 h^{-1} \text{ kpc} < r_p < 100 h^{-1} \text{ kpc}$, we observe an opposite trend, i.e. FMR-predicted offsets tend to be more negative than measured offsets. This implies that, at fixed stellar mass *and* SFR, galaxy pairs have slightly higher metallicities than isolated galaxies¹. We repeat the same procedure for the SFR, i.e., we invert the FMR in equation 7.5 to use stellar mass and metallicity in order to compute FMR-predicted values of SFR for galaxy pairs. The median offsets are shown as a dashed line in the top right panel of Figure 7.5. Similar results are obtained when comparing with measured SFR offsets, e.g. opposite trends at small and intermediate projected separations, and an overall discrepancy with FMR predictions, except at large separations, where the offsets converge.

¹The FMR is fitted to our general sample of galaxies, in which only about 10% are potentially interacting galaxies. Therefore, the FMR encodes, on average, the behaviour of isolated galaxies.

7. MERGER-INDUCED METALLICITY DILUTION IN SDSS GALAXIES

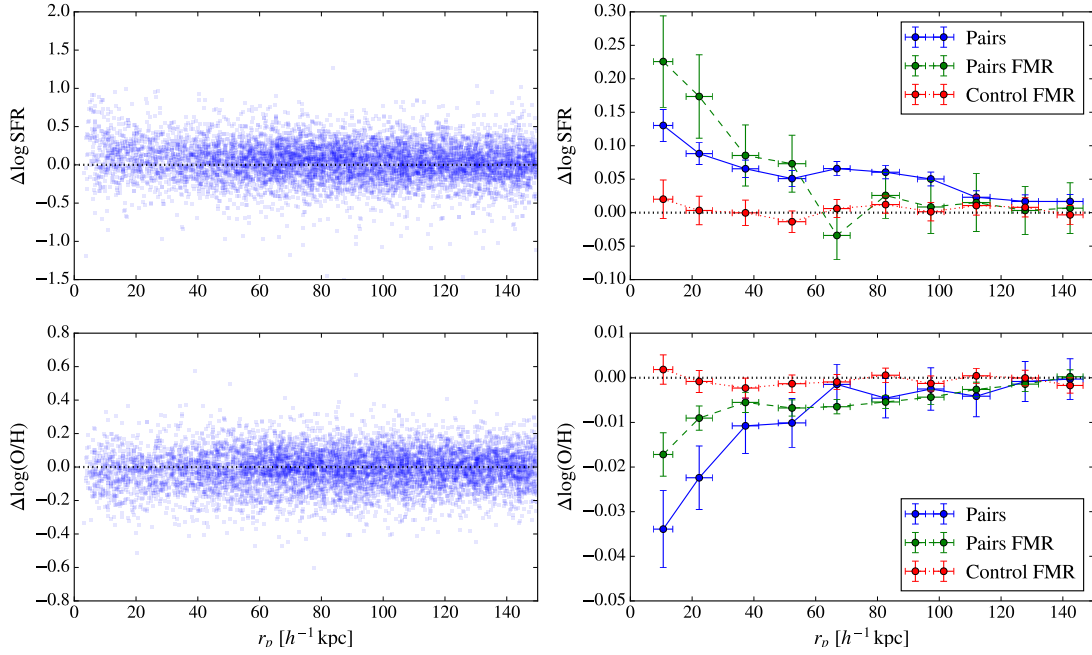


Figure 7.5: Individual offset values (*left panels*) and the respective medians (*right panels*) of SFR (*top panels*) and metallicity (*bottom panels*) for all 7514 galaxy pairs as a function of projected separation. Error bars denote standard error of the median. Blue solid lines correspond to median values of the measurements, green dashed lines to medians of FMR-predicted values, and red dotted lines to medians of FMR-predicted values for the control galaxies. At low projected separations, galaxy pairs deviate from the FMR-predicted values, exhibiting thus stronger SFR enhancement and metallicity dilution. At separations $r_p > 100 h^{-1}$ kpc, galaxy companions exert small effects, and both measured and FMR-predicted values converge.

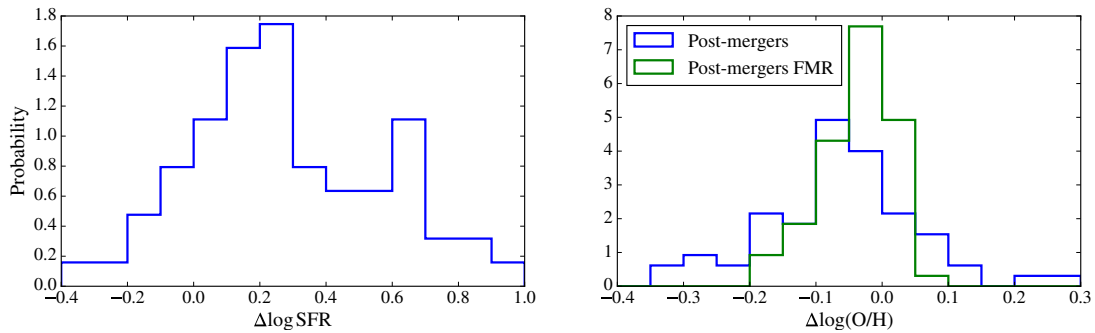


Figure 7.6: Distribution of offsets of SFR (*left panel*) and metallicity (*right panel*) for the sample of post-merger galaxies. Blue histograms represent measured values, whereas the green histogram represents the FMR-predicted metallicities. Post-merger galaxies exhibit SFR enhancements and metallicity dilutions that are consistent with the trends of galaxy pairs, showing thus that those processes are still ongoing after coalescence. The FMR under-predicts the strength of the dilution.

All offsets, including those of FMR-predicted quantities, are calculated with respect to the statistical mean of measured values of control galaxies, i.e. by using equation 7.4. For the sake of consistency, we also compute the offsets of the FMR predictions for control galaxies. The corresponding medians are shown as red dotted lines in Figure 7.5. Deviations of metallicity offsets from the zero line are within a sensible range according to the fitted Gaussian distribution of residuals. This shows that the FMR encodes the behaviour of isolated galaxies remarkably well.

Finally, we show in Figure 7.6 the distribution of offsets of SFR and metallicity for post-merger galaxies. The median offsets are 0.26 dex and -0.064 dex, for SFR and metallicity, respectively. These values are consistent with the slope of the relations for galaxy pairs at close projected separations, thereby suggesting that SFR enhancement and metallicity dilution still continue during post-merger stages. Although the FMR also predicts metallicity dilution in this case, i.e. a median of value of -0.024 dex, measured offsets are still on average lower than the measured values. After applying a Kolmogorov-Smirnov test to compare the distributions of observed metallicities vs FMR-predicted values, the hypothesis of both sets of values being drawn from the same distribution can be rejected at a confidence level of $\alpha = 2\%$. This implies that the population of post-merger galaxies is not well described by the FMR. B18 obtain similar results in simulated galaxies, in which SFR enhancement and metallicity dilution can last up to 300 Myr after coalescence and the FMR under-predicts the strength of the dilution.

7. MERGER-INDUCED METALLICITY DILUTION IN SDSS GALAXIES

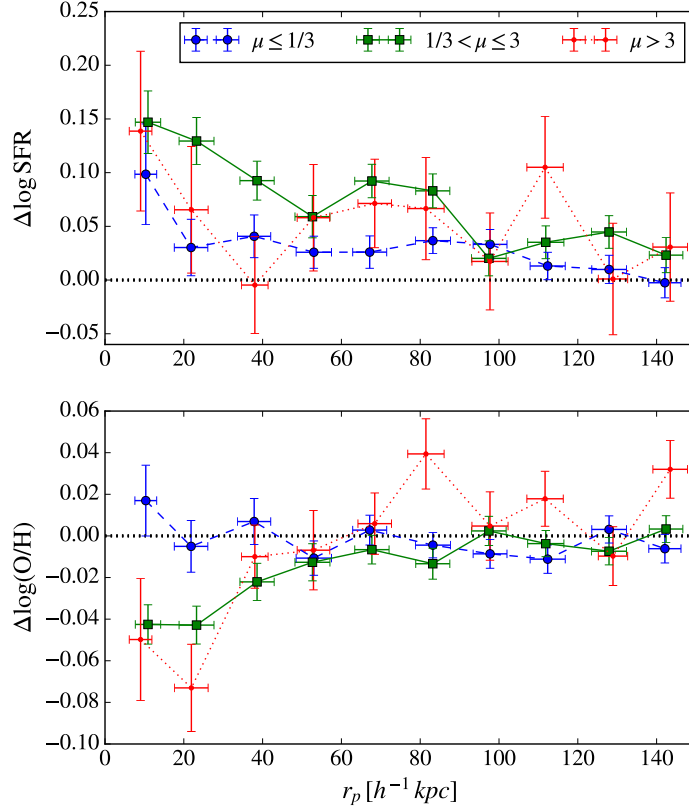


Figure 7.7: Median offsets of SFR (*top panel*) and metallicity (*bottom panel*) as a function of projected separation for different bins of merger mass ratio. We define three different bins as follows: a first bin of low mass companions of minor mergers $\mu \leq 1/3$ (dashed lines and blue circles), a second bin of both members in major mergers $1/3 < \mu \leq 3$ (solid lines and green squares), and third bin of main galaxies in minor mergers $\mu > 3$ (dotted lines and red dots).

7.3.3 Stellar mass ratio dependence

Although both major and minor mergers have an important contribution to the galaxy assembly process, they are very different in nature. For example, whereas major mergers are much more disruptive, minor mergers are much more frequent. Owing to this, it is interesting to study the difference in SFR and metallicity trends for major versus minor mergers. In order to do so, we define three different bins of merger mass ratio for the galaxy pair sample. A first bin of low mass companions in minor mergers ($\mu \leq 1/3$), with 3566 galaxies (47% of the sample); a second bin of major mergers, both members included ($1/3 < \mu \leq 3$), with 3374 galaxies (45% of the sample); and a third bin of main galaxies in minor mergers ($\mu > 3$), with 574 galaxies (8% of the sample). The same bins are also adopted by [Scudder et al. \(2012\)](#).

We plot the median offsets of SFR and metallicity with respect to the control sample as function of projected separation in Figure 7.7. We notice that SFR enhancement occurs in all cases, with major mergers expectedly exhibiting the higher offsets. Interestingly, the smaller companions in minor mergers experience significant SFR enhancements only at small separations $r_p \lesssim 20 h^{-1}\text{kpc}$, while main companions, with the exception of the bin at $40 h^{-1}\text{kpc}$, show relatively higher SFR enhancements in a wider range of separations. For metallicity offsets, we see that dilution only occurs appreciably in major mergers and massive companions in minor mergers, with the latter exhibiting slightly stronger dilutions at close separations. Smaller companions in minor mergers exhibit comparatively flatter profiles and lower offsets, implying thus that no significant dilution takes place. As a caveat, we note that the statistical significance of the bin of massive companions in minor mergers is weak as it has very few galaxies compared to the other two bins.

The median masses of galaxies in the bins are: $10^{9.6} M_{\odot}$, $10^{9.9} M_{\odot}$ and $10^{10.1} M_{\odot}$ for the bins 1, 2 and 3, respectively. A trend between galaxy mass and mass ratio is expected as minor mergers are more common in low and high mass galaxies. Likewise, intermediate mass galaxies are more often involved in major mergers. By randomly culling galaxies in bins 1 and 2, we match the mass distribution of galaxies in bin 3. We use these sub-samples in order to recompute the median offsets as function of projected separation. Comparable trends to those in Figure 7.7 are obtained, i.e. major mergers and massive companions in minor mergers exhibit stronger offsets than small companions. This demonstrates that the strengths of the SFR enhancement and the metallicity dilution are less dependent on galaxy mass and indeed driven mostly by the mass ratio.

7.3.4 Environmental effects

Considering galaxy mergers as ideal isolated systems has proven to be an accurate approximation as the effects exerted by close companions are, in most cases, more significant than cosmological effects; nevertheless, in dense environments and compact groups, other neighbouring galaxies might also play an important role in the evolution of galaxy properties (Park et al., 2007; Ellison et al., 2010; Moreno et al., 2013; Sabater et al., 2013; Patton et al., 2016; Sparre & Springel, 2016, B18). In this subsection, we study the effects of the environment on the SFR enhancement and the metallicity dilution processes. In order to do so, we use the metrics N_2 and r_2 to define four different samples (see Figure 7.8). Sample 1 and sample 2 have different ranges of neighbour density, i.e. $N_2 < 15$ and $N_2 \geq 15$, which

7. MERGER-INDUCED METALLICITY DILUTION IN SDSS GALAXIES

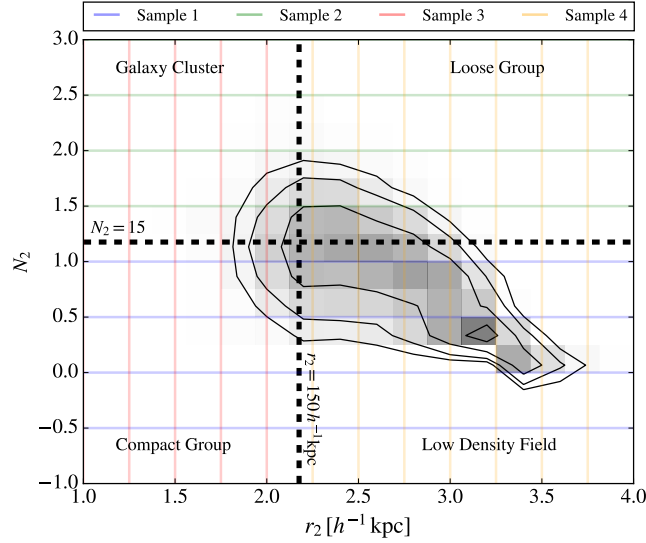


Figure 7.8: Environmental classification of galaxy pairs. Four different type of environments are defined in terms of r_2 and N_2 , namely: compact groups, galaxy clusters, loose groups and low density field. The defining conditions are listed in subsection 7.2.1. The 2D histogram represents the galaxy number count in each bin. Contour levels show galaxy number counts of 50, 100, 200 and 400. The majority of the galaxy pair sample is detected in low density fields. In order to quantify environmental effects on SFR enhancement and metallicity dilution, we define four samples represented by horizontal/vertical coloured lines.

include galaxies in compact groups and low density fields (73 % of galaxy pairs), and galaxies in galaxy clusters and loose groups (27 % of galaxy pairs), respectively. Sample 3 and sample 4 have different ranges of relative distance to a third neighbour, i.e. $r_2 < 150 h^{-1} \text{ kpc}$ and $r_2 \geq 150 h^{-1} \text{ kpc}$, which include galaxies in galaxy clusters and compact groups (15 % of galaxy pairs), and galaxies in loose groups and low density fields (85 % of galaxy pairs), respectively.

In Figure 7.9, we compute the median offsets of SFR and metallicity for galaxies in sample 1 (low N_2) and sample 2 (high N_2). By comparing the different trends, we are able to assess the relative importance of the neighbour density. We see no statistically significant differences in the median metallicity offsets. For SFR offsets, at projected separations $r_p > 40 h^{-1} \text{ kpc}$, galaxies in more dense environments have slightly lower values, i.e. providing evidence for environmental suppression of the SFR. At smaller separations $r_p < 20 h^{-1} \text{ kpc}$, the trend is opposite and galaxies in less dense environments have smaller offsets; nevertheless, the differences are not statistically significant.

We also compute median offsets for sample 3 and sample 4 in Figure 7.10. In this case,

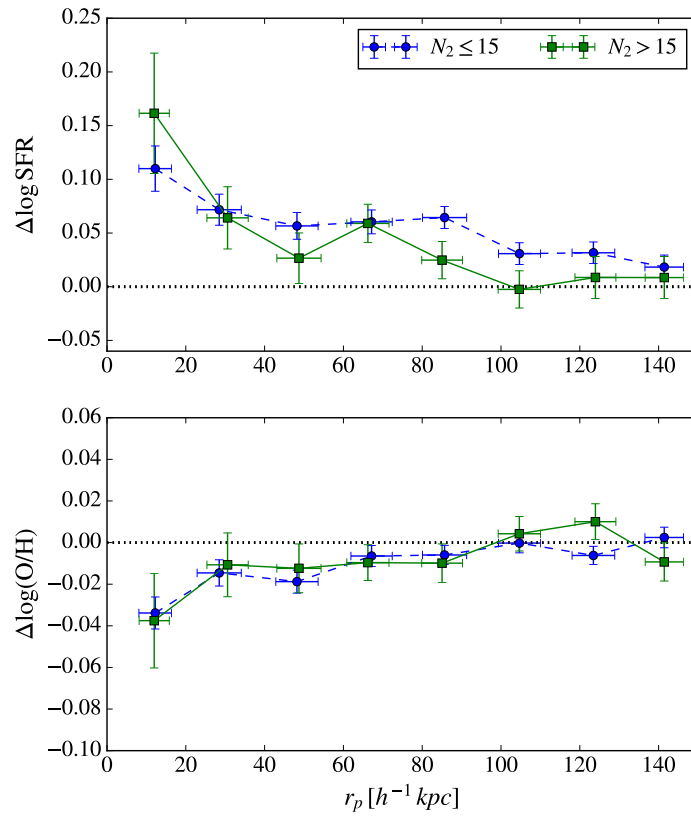


Figure 7.9: Median offsets of SFR (*top panel*) and metallicity (*bottom panel*) as a function of projected separation for sample 1 (low N_2) and sample 2 (high N_2). The use of these samples allows us to quantify the relative importance of the neighbour density N_2 . We do not see an appreciable difference between the trends.

7. MERGER-INDUCED METALLICITY DILUTION IN SDSS GALAXIES

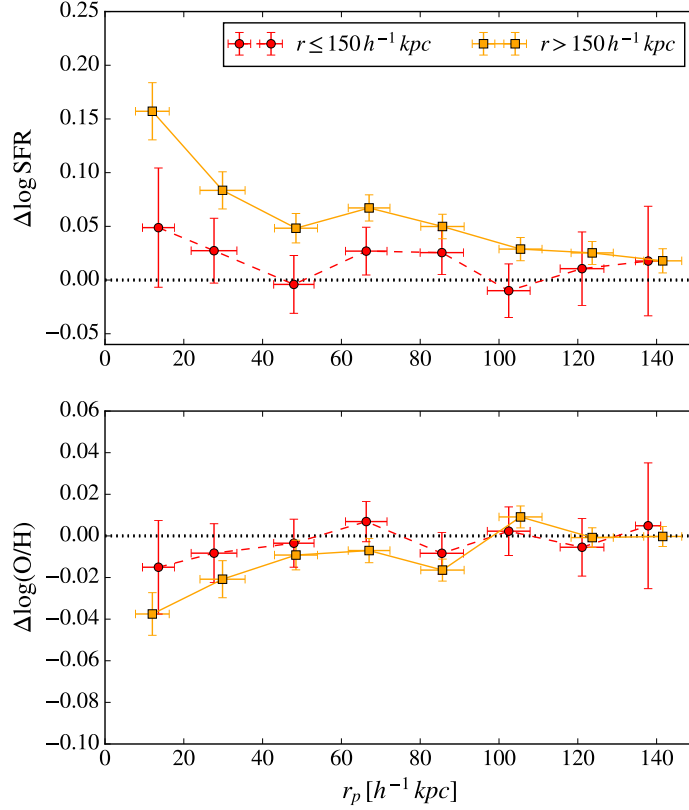


Figure 7.10: Median offsets of SFR (*top panel*) and metallicity (*bottom panel*) as a function of projected separation for sample 3 and sample 4. The use of these samples allow us to quantify the relative importance of a third companion, i.e. through its projected separation r_2 . SFR offsets of galaxies with a close third companion are, on average, lower than those of relatively isolated galaxies pairs. A weaker difference is also seen in metallicity offsets.

we want to assess the importance of a third companion in the SFR enhancement and the metallicity dilution in galaxy pairs. For the SFR, galaxy pairs with a close third companion exhibit smaller offsets than more isolated pairs. Likewise, metallicity offsets in isolated pairs are also slightly larger.

The mass distributions of galaxies in sample 3 and sample 4 are very similar, with median values of $10^{9.62} M_{\odot}$ and $10^{9.68} M_{\odot}$, respectively. Selection effects between galaxy mass and projected separation of the second closest companion are therefore small or nonexistent in the galaxy pair sample, showing thus that the differences in the trends are indeed caused by the presence of a close third companion. The median masses of galaxies in sample 1 and sample 2 differ more appreciably, i.e. $10^{9.78} M_{\odot}$ and $10^{9.52} M_{\odot}$, respectively. This reveals the presence of a selection effect in which more massive galaxies are more likely to be detected

in less dense environments. Nevertheless, the small statistical significance of the differences between the corresponding trends of these two samples –particularly for metallicity– shows that galaxy mass does not play an important role. This is in agreement with the results of subsection 7.3.3 regarding the more relevant role of the mass ratio compared to the galaxy mass.

For all the samples, the offsets have a strong dependence on the projected separation to the closest galaxy, thereby demonstrating that the interaction with a close companion is what drives the SFR enhancement and metallicity dilution processes. The environmental effects become relevant only through the presence of a close third companion. The local density of neighbouring galaxies does not seem to play an appreciable role.

7.4 Discussion

The connection between low metallicities and high SFRs in the FMR reflects the fact that quiescent star formation is more efficient in galaxies with a high content of pristine gas, and hence low metallicities. At first glance, this connection seems to be supported by observations of galaxy pairs in which systematic positive SFR offsets and negative metallicity offsets are measured with respect to a control sample of isolated galaxies (Ellison et al., 2008b; Scudder et al., 2012; Cortijo-Ferrero et al., 2017; Thorp et al., 2019). Likewise, simulations of galaxy mergers show that, during a close pericenter passage or final coalescence, strong nuclear gas inflows can dilute the metallicity and enhance star formation activity (e.g. Torrey et al., 2012; Hani et al., 2018, B18). Nevertheless, we have shown in this chapter that the offsets of SFR and metallicity in SDS galaxy pairs are not consistent with FMR predictions. We conjecture that the active role of strong nuclear inflows in diluting the gas is not accounted for in the FMR as this process is sub-dominant in quiescent, isolated galaxies, especially at low redshift. This explains the underestimated FMR-predicted offsets at low projected separations. At intermediate projected separations, galaxy companions are generally on their way to a first passage, or to final coalescence after a passage, i.e. close to the apocenter. Simulations also show that, close to the apocenter after a close passage, gas inflows rapidly decrease and metallicity dilution cannot be sustained. Enhanced star formation activity can, however, linger and cause metal enrichment. This results in galaxy pairs in the intermediate separation range exhibiting enhanced SFRs and high metallicities compared to the predictions of the FMR.

The small offsets of metallicity and SFR for the less massive galaxy companions in

7. MERGER-INDUCED METALLICITY DILUTION IN SDSS GALAXIES

minor mergers can be caused by a strangulation mechanism described by [Peng et al. \(2015\)](#). In this scenario, the supply of cold gas in the galaxy is halted as a result of tidal stripping by the massive companion, thereby preventing a boost in star formation activity. Only at small separations comparable to the tidal radius of the small companion, the SFR is enhanced as gas accretion from the massive companion is possible.

7.5 Conclusions

In this chapter, we study the processes of metallicity dilution and SFR enhancement in galaxy pairs and post-merger galaxies from the SDSS DR7 survey. We contrast our measurements with those predicted by the FMR. In order to do so, we fit the general pool of galaxies to a second-order polynomial in stellar mass, metallicity and SFR that represents the FMR. We also construct control samples for galaxy pairs and post-merger galaxies by matching in redshift, stellar mass and environment. We find that the offsets of metallicity and SFR measured with respect to the control samples increase for closer pairs and larger stellar mass ratios. Although this is in qualitative agreement with the expectations of the FMR, a closer inspection shows that the FMR under-predicts the strength of these processes. A similar scenario occurs with post-merger galaxies. Therefore, we conclude that interacting galaxies constitute a well-defined outlier population and that the FMR is not universal. Finally, we find that the SFR enhancement process in merging galaxies is affected by the presence of a close third companion. On the other hand, other environmental conditions such as the local density of neighbouring galaxies do not seem to play an appreciable role.

Part III

Modelling supermassive black holes in a cosmological context

Spin evolution of supermassive Black Holes

In this chapter, we present a new sub-grid model of black hole spin evolution in cosmological simulations of galaxy formation. This work has been submitted for publication to the journal of the Monthly Notices of the Royal Astronomical Society.

8.1 Introduction

It is remarkable finding that most, quite possibly all, galaxies host a supermassive black hole (BH) at their centres (e.g. [Greene et al., 2010](#)). The origin of these black holes (i.e. the “seeds” that subsequently grew) in the high redshift universe is still unclear, but it appears relatively certain that much of the mass of the black hole population was accumulated through gas accretion ([Soltan, 1982](#)). The accretion processes themselves are accompanied by a substantial release of energy, which is most dramatically seen in the emission of powerful quasars ([Lynden-Bell, 1969](#)).

The relatively tight scaling relations between galaxy properties and the masses of the central supermassive BH ([Magorrian et al., 1998](#); [Ferrarese & Merritt, 2000](#); [Häring & Rix, 2004](#)) suggest that the BHs are not merely spectators in the galaxy formation process, but rather influence it in decisive ways. This view has motivated the incorporation of black hole evolution and feedback processes in modern theories of galaxy formation ([Kauffmann &](#)

8. SPIN EVOLUTION OF SUPERMASSIVE BLACK HOLES

Haehnelt, 2000). In particular, many simulation models explain the quenching transition of galaxies from the star forming blue cloud to the red sequence of elliptical galaxies as a result of BH feedback (Di Matteo et al., 2005; Springel et al., 2005; Sijacki et al., 2007). In large clusters of galaxies, the BHs can furthermore offset radiative cooling losses through sporadically going through phases of active galactic nuclei (AGN) activity, thereby preventing excessive cooling flows. Another importance of this AGN feedback lies in its ability to expel baryons even from deep potential wells of galaxy groups and clusters, helping to understand the observed trends of the baryon content in these objects (McCarthy et al., 2007; Puchwein et al., 2008).

The recent discovery of gravitational waves from stellar-mass black holes (Abbott et al., 2016) has additionally fuelled the interest in the merger processes of supermassive black holes, which are inevitable events during hierarchical structure formation. In the future, coalescing BH binaries in the relevant mass range should become detectable by pulsar timing arrays and the Laser Interferometer Antenna (LISA). These unprecedented experiments will shed light on the BH assembly process, but they also require theoretical predictions for the expected merger rates and a characterisation of the precursors of BH binaries. The BH mergers will emit copious amounts of gravitational waves, leading to a recoil of the merger remnant. As a result, they may be even ejected from the host galaxy in certain situations. In any case, the timescale of return of the remnant BH to the centre of the galaxy is important as during this phase the regulation of a quasi-static hot atmosphere in the halo may temporarily be interrupted, allowing star formation to resume and potentially impact the evolution of massive galaxies.

Supermassive black holes are therefore a key element of any modern theory of galaxy formation and evolution, and they are now routinely incorporated both in semi-analytic (e.g. Croton et al., 2006; Henriques et al., 2015) and hydrodynamical simulation models (e.g. Vogelsberger et al., 2014; Schaye et al., 2015). Despite this central importance of supermassive BHs, the physical processes governing their evolution, especially with respect to the gas accretion and the associated feedback processes, are only poorly understood. The modelling in cosmological hydrodynamic simulations is hence very sketchy, and typically encapsulated in heuristic sub-grid models. Commonly, black holes are simply treated as sink particles of a given mass, and all modelling of the physics neglects the one other important parameter characterising the black holes, namely their angular momentum. This is a significant limitation, because the BH spin affects the radiative efficiency of accretion processes decisively. In fact, while it is believed that typically of order 5% of the accreted rest mass energy of a

non-spinning BH is released as radiation, this can go up to about 40% for highly spinning black holes (Blandford & Znajek, 1977; Tchekhovskoy et al., 2011). In addition, the spin of merging BHs has a strong influence on the gravitational wave emission, and thus also on the expected recoil velocity of the merger remnant (Campanelli et al., 2007).

For all these reasons, modelling BH spins appears to be a promising extension of current treatments of black hole physics. Corresponding simulations would then not only yield predictions for the BH mass function and its evolution over time, for the lifetimes and activity patterns of quasars, their clustering, and for their overall influence on the galaxy formation process, they would also be able to make predictions for the statistics of BH spin, including for the typical spin configurations expected in supermassive BH mergers. This in turn would inform attempts to forecast gravitational wave signals and their frequency, and elucidate the importance of spin for the energy release through gas accretion. It is therefore timely to go beyond the first generation of BH models and implement more detailed physical models for BH spin in the current cosmological codes for galaxy formation.

At first sight, it may seem conceptually simple to relate the BH growth to the specific angular momentum content of the accreted gas, but the huge range of scales that are in reality still unresolved in cosmological simulations can not simply be ignored easily. In fact, the accretion flows that actually develop close in to the BH can give rise to angular momentum transport, in addition to an important coupling between a preexisting BH spin and the surrounding gas, causing phenomena such as Lense-Thirring precession. This necessitates the construction of explicit sub-grid models for the BH spin evolution which are guided by analytic theory, and which respond to the larger-scale boundary conditions set by the cosmological simulation. A few such models have already been constructed. Fanidakis et al. (2011) pioneered such treatments in the context of semi-analytic modelling of galaxy formation. Dubois et al. (2014) study the BH spin evolution in hydrodynamical cosmological simulations in a post-processing fashion. Recently, and independently from our work, Fiacconi et al. (2018) presented a first effort using the moving-mesh code AREPO, which we also employ here. Our model is similar in spirit to theirs, but differs in a number of details. Importantly, we consider the back-reaction on the feedback efficiency and couple the spins to the black hole feedback mode. In particular, we conjecture to relate the transition in feedback modes, introduced in the IllustrisTNG black hole treatment in an ad-hoc fashion by Weinberger et al. (2017), to the spin evolution, and test the impact this has.

This chapter is structured as follows. In Section 8.2, we begin by reviewing the basic problem of how BH spin evolves through gas accretion and BH binary coalescence. In

8. SPIN EVOLUTION OF SUPERMASSIVE BLACK HOLES

Section 8.3, we detail our black hole growth and feedback model, as well as its coupling to the spin evolution. We then discuss our numerical implementation of these processes and our simulation set in Section 8.4. Our results for the statistics of BH spin in cosmological simulations are presented in Section 8.5, while results for the impact of our spin modelling through a novel feedback switch on the Section 8.6. Finally, we summarise our findings and give our conclusions in Section 8.7.

8.2 Spin evolution of Black Holes

In this section, we present a model for the evolution of the BH spin. Besides its mass, the spin of a BH is an important property as it affects the efficiency with which a BH can process parts of the matter in an accreted disc into radiation; it impacts the strength and emission direction of radio jets; it possibly regulates the radio-loudness of the host galaxy; and it determines both the detailed gravitational wave emission signal and the distribution of recoil velocities in BH-BH mergers, which is important for forecasting these events and the subsequent evolution of the BH remnant.

The spin is simply defined as the BH angular momentum with respect to the centre-of-mass frame, and is commonly expressed as:

$$J_{\text{bh}} = |a| \frac{GM_{\text{bh}}^2}{c}, \quad (8.1)$$

where a is the dimensionless spin parameter ($0 \leq |a| \leq 1$), M_{bh} the black hole mass, G the gravitational constant and c the vacuum speed of light. This parametrisation results from assuming a Kerr metric for rotating bodies, in which the maximum allowed spin is GM_{bh}^2/c . In what follows, we assume two main channels through which BHs can be spun up or down, namely gas accretion and BH mergers.

8.2.1 Gas accretion

BHs in galactic centres process matter into radiation through a surrounding accretion disc that is fed by cold gas inflows from galactic scales. If a BH is accreting above 1% of its Eddington rate, we assume that a classical thin, optically thick Shakura-Sunyaev α -disc (Shakura & Sunyaev, 1973) settles around it (Fanidakis et al., 2011). On the other hand, for accretion rates below this value, the α -disc model is no longer appropriate and advec-

tion dominated disc models (ADAF) would have to be considered. However, given that in this case the gas does not carry enough angular momentum to modify the spin of the BH significantly, we simply turn off the gas channel under these conditions.

Once an accretion disc is formed, the orbiting gas loses its angular momentum through viscous torques caused by magnetic fields (Lynden-Bell, 1969) and radiates away the binding gravitational energy, moving thus inwards and reaching the radius of the innermost stable circular orbit (ISCO) of the BH. After this point, further angular momentum and energy losses are no longer required as the gas will then be accreted on a very short timescale.

The radius of the ISCO can be expressed in terms of the BH spin as (Bardeen et al., 1972):

$$\hat{r}_{\text{isco}} = \frac{r_{\text{isco}}}{R_g} = 3 + Z_2 \pm [(3 - Z_1)(3 + Z_1 + 2Z_2)]^{1/2}, \quad (8.2)$$

where the negative sign is taken if the disc is counter-rotating with respect to the BH spin (i.e. $a < 0$). The positive sign corresponds to the case of co-rotation. For the sake of simplicity, a normalisation with the gravitational radius R_g is used here, which is defined as half of the Schwarzschild radius:

$$R_g = \frac{R_{\text{Schw}}}{2} = \frac{GM_{\text{bh}}}{c}. \quad (8.3)$$

The quantities Z_1 and Z_2 depend on the BH spin, and are defined as:

$$Z_1 \equiv 1 + (1 - a^2)^{1/3} [(1 + a)^{1/3} + (1 - a)^{1/3}], \quad (8.4)$$

$$Z_2 \equiv (3a^2 + Z_1^2)^{1/2}. \quad (8.5)$$

Once a parcel of gas of mass dM_0 reaches the ISCO, it will be eventually accreted and its energy and angular momentum per unit mass, \tilde{e}_{isco} and \tilde{l}_{isco} , will add to the total BH mass and angular momentum, respectively:

$$dM_{\text{bh}} = \frac{\tilde{e}_{\text{isco}}}{c^2} dM_0, \quad dJ_{\text{bh}} = \tilde{l}_{\text{isco}} dM_0. \quad (8.6)$$

Combining these expressions with equation (8.1) yields the following differential equation:

$$\frac{da}{d \ln M_{\text{bh}}} = \frac{1}{M_{\text{bh}}} \frac{c^3 \tilde{l}_{\text{isco}}}{G \tilde{e}_{\text{isco}}} - 2a. \quad (8.7)$$

Integrating this equation, Bardeen (1970) obtained a solution for the evolution of the

8. SPIN EVOLUTION OF SUPERMASSIVE BLACK HOLES

spin magnitude:

$$a^f = \frac{1}{3} \hat{r}_{\text{isco}}^{1/2} \frac{M_{\text{bh}}}{M_{\text{bh}}^f} \left[4 - \left\{ 3 \hat{r}_{\text{isco}} \left(\frac{M_{\text{bh}}}{M_{\text{bh}}^f} \right)^2 - 2 \right\}^{1/2} \right], \quad (8.8)$$

where a^f and M_{bh}^f correspond to the final spin and BH mass after an accretion episode of mass

$$M_d = \frac{M_{\text{bh}}^f - M_{\text{bh}}}{1 - \epsilon_r}. \quad (8.9)$$

Here, ϵ_r is the radiative efficiency of the accretion disc, which measures the fraction of gravitational binding energy released by gas spiralling in towards the BH. In the case of a Kerr BH, the radiative efficiency depends on the spin as follows (Novikov & Thorne, 1973):

$$\epsilon_r \equiv 1 - \sqrt{1 - \frac{2}{3} \frac{1}{\hat{r}_{\text{isco}}(a)}}. \quad (8.10)$$

Note that equation (8.8) can be used to update the BH spin only if $M_{\text{bh}}^f/M_{\text{bh}} \leq \hat{r}_{\text{isco}}^{1/2}$. In the case of $M_{\text{bh}}^f/M_{\text{bh}} > \hat{r}_{\text{isco}}^{1/2}$, a single accretion episode is able to spin up the BH to its maximum value $a = 1$; however, we cap the maximum spin to $a = 0.998$ to account for the absorption of photons with angular momentum opposite to the BH spin (Thorne, 1974).

Accreting gas in misaligned discs

The previous analysis led us to a formula to compute the evolution of the BH spin once a mass M_d has fallen in towards the accretion disc. However, this analysis provides no information about the accretion process and on how much mass is ultimately accreted, i.e. we do not know the value of M_d . In order to estimate this, we assume a general case in which an accretion disc settles around the BH and lies initially misaligned with respect to the BH equatorial plane. Under this configuration, the orbiting gas experiences a torque caused by the Lense-Thirring effect of the spinning BH, which is given by:

$$\frac{\partial \mathbf{L}}{\partial t} = \boldsymbol{\omega}_{\text{prec}} \times \mathbf{L}, \quad (8.11)$$

where $\boldsymbol{\omega}_{\text{prec}} = (2G/c) \mathbf{J}_{\text{bh}}/R^3$ is the precession rate, \mathbf{L} is the angular momentum per unit area of the disc and R the distance from the BH (Pringle, 1992). This torque causes the

gas orbits to become unstable and evolve into lower energy states, which in turn makes the plane of the disc precess around the BH spin axis at a frequency ω_{prec} . If the viscosity of the gas is sufficiently high, the innermost part of the disc aligns with the equatorial plane of the spinning BH, giving rise to a warped disc.

In the α -disc solution, the kinematic viscosity of the gas is split into two components, ν_1 and ν_2 , which act along velocity gradients parallel and perpendicular to the disc plane, respectively. This allows us to introduce two characteristic timescales: an accretion timescale $t_{\text{acc}} \equiv R^2/\nu_1$, during which gas drifts inwards and angular momentum is transported outwards through radial viscous dissipation; and a warp timescale $t_{\text{warp}} \equiv R^2/\nu_2$, during which any vertical disturbance propagates across the disc, e.g. the warp.

Introducing the precession timescale $t_{\text{prec}} \equiv 2\pi/\omega_{\text{prec}}$, it is possible to estimate the size of the warped region by imposing the condition $t_{\text{prec}}(R) \lesssim t_{\text{warp}}(R)$, i.e. if restoring viscous forces are overcome by frame-dragging torques the disc cannot retain its original shape. Using the following parametrisation of the radial viscosity $\nu_1 = \alpha H^2 \Omega_k$, where H is the disc semi-thickness and Ω_k the Kepler frequency, the following expression for the warp radius R_{warp} is obtained (Volonteri et al., 2007):

$$\frac{R_{\text{warp}}}{R_{\text{Schw}}} = 3.6 \times 10^3 a^{5/8} \left(\frac{M_{\text{bh}}}{10^8 M_{\odot}} \right)^{1/8} f^{-1/4} \left(\frac{\nu_2}{\nu_1} \right)^{-5/8} \alpha^{-1/2}, \quad (8.12)$$

where $f \equiv L/L_{\text{Edd}}$ is the Eddington ratio, $L = \epsilon_r \dot{M} c^2$ and $L_{\text{Edd}} = 4\pi G M_{\text{bh}} m_p / \kappa$ are the disc and Eddington luminosities, respectively, \dot{M} is the total accretion rate of the system, m_p the proton mass, and $\kappa \approx 0.3 \text{ cm}^2 \text{ g}^{-1}$ denotes the electron scattering opacity.

The warp radius is an important quantity as it provides a characteristic length scale of the accretion disc. Besides, only the material inside it can effectively transfer angular momentum to the BH (Volonteri et al., 2007). The mass of the warped region can be readily estimated as $M_{\text{warp}} = \dot{M} t_{\text{acc}}(R_{\text{warp}})$, where:

$$t_{\text{acc}} = \frac{R_{\text{warp}}^2}{\nu_1} = 3 \times 10^6 a^{7/8} \left(\frac{M_{\text{bh}}}{10^8 M_{\odot}} \right)^{11/8} \times \lambda^{-3/4} \left(\frac{\nu_2}{\nu_1} \right)^{-7/8} \alpha^{-3/2} \text{ yr}. \quad (8.13)$$

One of the main uncertainties of the α -disc solution is the relation between the two viscosities ν_1 and ν_2 , which ultimately determines which process, warp alignment or mass

8. SPIN EVOLUTION OF SUPERMASSIVE BLACK HOLES

accretion, occurs in a shorter timescale. In the thin disc regime, i.e. $H/R < \alpha \ll 1$, the condition $\nu_2/\nu_1 \approx 1/\alpha^2$ has to be fulfilled (Papaloizou & Pringle, 1983). We use the relation $\nu_2/\nu_1 = 2(1 + 7\alpha)/(\alpha^2(4 + \alpha^2))$ proposed by Ogilvie (1999) that satisfies this condition. Under these assumptions, we obtain that $t_{\text{warp}} < t_{\text{acc}}$, which means that the innermost disc aligns with the equatorial plane of the BH quicker than the timescale of mass and angular momentum accretion. This allows us to use M_{warp} as a proxy of the accreted mass of a single accretion episode, i.e. $M_{\text{d}} \approx M_{\text{warp}}$. Finally, using equation (8.9), we calculate the final BH mass M_{bh}^f needed for evolving the BH spin through equation (8.8).

Alignment/Counter-alignment condition

We have previously concluded that before the content of the innermost disc is accreted, it settles on the equatorial plane of the BH. Additionally, King et al. (2005) established that the warped region, once settled, can align or anti-aligned with respect to the BH spin depending on the initial configuration of the disc angular momentum and the BH spin. In order to highlight the importance of determining the sense of rotation of the gas at the ISCO, we analyse equation (8.2). For a disc counter-rotating with respect to a maximum spinning BH, the radius of the ISCO is $\hat{r}_{\text{isco}} = 9$. In the case of co-rotation, $\hat{r}_{\text{isco}} = 1$. This means that counter-rotating gas needs to lose less energy and angular momentum than co-rotating gas before being ultimately accreted and, therefore, adds up more to the BH mass and spin. On the other hand, co-rotating gas also increases the energy output of the BH, favouring feedback processes.

In what follows, we inspect what condition determines alignment/anti-alignment. We denote the angular momentum of the innermost warped disc as \mathbf{J}_{d} . The total angular momentum is then given by:

$$\mathbf{J}_{\text{tot}} = \mathbf{J}_{\text{bh}} + \mathbf{J}_{\text{d}}. \quad (8.14)$$

This vector is constant in magnitude and orientation during the whole accretion episode due to conservation of angular momentum in the BH-disc system. In Figure 8.1 we illustrate the relative orientations of the vectors for different phases of an accretion episode. King et al. (2005) derived a set of equations that describes the evolution of \mathbf{J}_{bh} and \mathbf{J}_{d} during the precession phase:

$$\frac{d}{dt} J_{\text{bh}}^2 = 0, \quad \frac{d}{dt} J_{\text{d}} \leq 0, \quad \frac{d}{dt} \cos \theta_t \geq 0, \quad (8.15)$$

where θ_t is the angle subtended between \mathbf{J}_{tot} and \mathbf{J}_{bh} . This shows that during this phase,

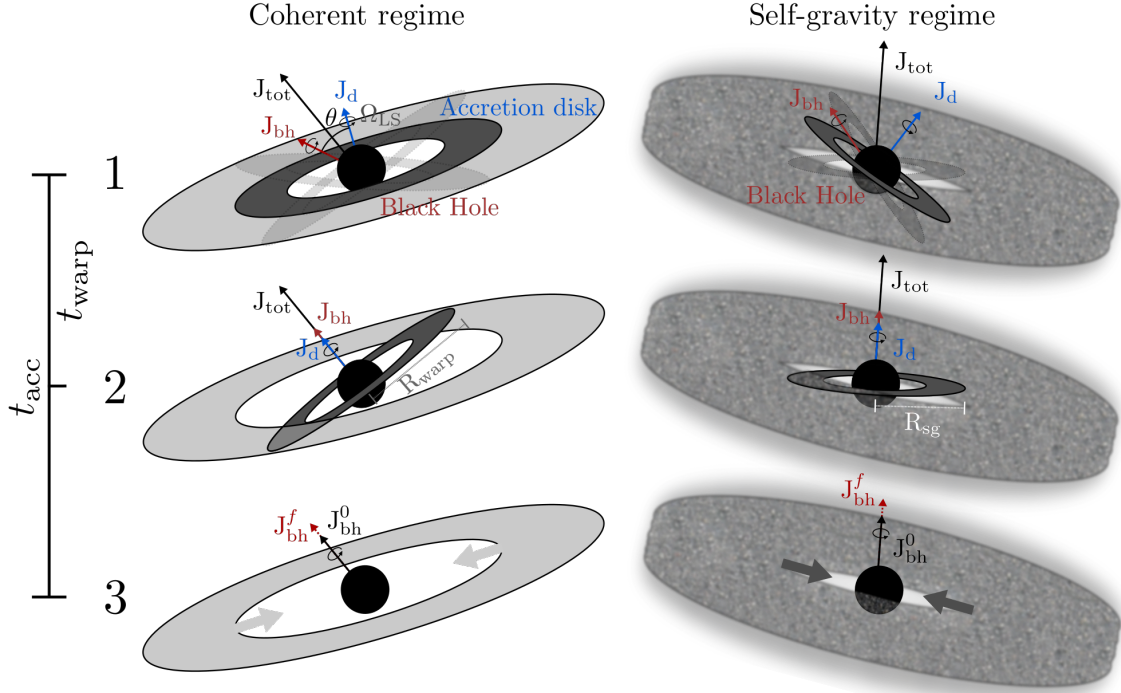


Figure 8.1: Schematic illustration of the spin evolution model. The evolution steps in the coherent (*left*) and self-gravity (*right*) regimes are shown. *Step 1* corresponds to the beginning of the accretion episode, when the innermost disc is precessing about the BH spin due to the Lense-Thirring effect. In the coherent regime there is an outer disc, whereas in the self-gravity regime the outer gas is fragmented and not settled in a disc. In *step 2*, the Lense-Thirring torque eventually aligns/anti-aligns the innermost disc and aligns the BH spin in the direction of the total angular momentum, giving rise to a warped disc. This occurs on the warp timescale t_{warp} . In the coherent regime, the warped disc has a radius R_{warp} . In the self-gravity regime the radius is smaller, and is given by R_{sg} . In *step 3* the warped disc has been already consumed by the BH, and a new accretion episode is already setting in. Given that the accretion timescale is longer, i.e. $t_{\text{warp}} < t_{\text{acc}}$, this is the last step of the accretion episode. In the coherent regime, the new accretion episode inherits the orientation of the outer disc. In the chaotic regime, the direction of the innermost disc angular momentum follows a von Mises distribution function.

8. SPIN EVOLUTION OF SUPERMASSIVE BLACK HOLES

the magnitude of the BH spin remains constant, while the disc angular momentum is continuously decreasing. The direction of the BH spin eventually aligns with the total angular momentum, while the disc will either counter-align or align depending on whether or not the following condition is satisfied (King et al., 2005):

$$\cos \theta < -\frac{J_d}{2J_{\text{bh}}}, \quad (8.16)$$

with θ the angle subtended between \mathbf{J}_{bh} and \mathbf{J}_d .

Considering that the angular momentum of the innermost disc is advected inwards, passing through R_{warp} , its magnitude can readily be computed as (King et al., 2008):

$$J_d \approx M_d \Omega_k(R_{\text{warp}}) R_{\text{warp}}^2 = M_d (GM_{\text{bh}} R_{\text{warp}})^{1/2}. \quad (8.17)$$

We have assumed that the gas has circularised on its way to the centre. This leads to the following expression for the ratio of disc to BH angular momentum:

$$\frac{J_d}{2J_{\text{bh}}} \approx \frac{M_d}{aM_{\text{bh}}} \left(\frac{R_{\text{warp}}}{R_{\text{Schw}}} \right)^{1/2}. \quad (8.18)$$

By evaluating this expression at the beginning of every accretion episode, we can determine whether alignment or counter-alignment occurs before the disc is accreted.

The last aspect to be determined is the orientation of \mathbf{J}_d . To do so, we assume that it coincides with that of the angular momentum of the neighbouring gas that ultimately feeds the BH-disc system. Although there is a large gap between the physical scale of the gas reservoir in the galactic centre and the scale of the accretion disc, it is reasonable to assume that during the feeding process, when the gas is on its way towards the disc, its angular momentum orientation is preserved.

Self-gravitating discs

When the mass accretion rate of the system is sufficiently large, the accretion disc becomes very massive and the effects of self-gravity are no longer negligible. This makes the disc become unstable and fragment into small gas clumps. In order to assess this more quantitatively, we use Toomre's stability criterion which balances rotational support of the disc against its own gravity:

$$Q \equiv \frac{c_s \Omega_k}{\pi G \Sigma_d}, \quad (8.19)$$

where Q is the Toomre parameter and c_s is the speed of sound in the gas. For $Q \leq 1$ the disc is unstable, which leads to the definition of a characteristic self-gravity radius R_{sg} at which $Q(R_{\text{sg}}) = 1$. For the α -disc solution, the following expression is derived (Fanidakis et al., 2011):

$$\frac{R_{\text{sg}}}{R_{\text{Schw}}} = 1.5 \times 10^3 \epsilon^{8/27} \left(\frac{M_{\text{bh}}}{10^8 M_{\odot}} \right)^{-26/27} f^{-8/27} \alpha^{14/27}. \quad (8.20)$$

As the parameter Q is a monotonically decreasing function of radius, the disc outside R_{sg} is subject to fragmentation whereas the inner disc remains stable. Nevertheless, as only the material within the warp radius can effectively transfer its angular momentum to the BH (Volonteri et al., 2007), we include self-gravity effects only when $R_{\text{sg}} \leq R_{\text{warp}}$ (Dubois et al., 2014). This is the defining condition of what we call the *self-gravity regime*. As opposed to this, we define the *coherent regime* when self-gravity is negligible. In Figure 8.1 we illustrate both regimes and the evolution steps in every accretion episode.

Note that during the self-gravity regime, the innermost disc still aligns with the equatorial plane of the BH and its mass is now given by (Fanidakis et al., 2011):

$$M_{\text{sg}} = 2.13 \times 10^5 \epsilon^{-5/27} \left(\frac{M_{\text{bh}}}{10^8 M_{\odot}} \right)^{23/27} f^{5/27} \alpha^{-2/27} M_{\odot}. \quad (8.21)$$

Using M_{sg} and R_{sg} instead of M_{d} and R_{warp} in equations (8.9) and (8.18), we can still evolve the magnitude of the BH spin.

Due to the intrinsic complexity of the self-gravity regime, the orientation of the disc angular momentum, or equivalently the material feeding the disc, has been a matter of debate. For instance, King et al. (2008) argued that low cooling times of the gas beyond the self-gravity radius provides an ideal scenario for star formation, which can occur in about a dynamical timescale. This would have disturbing effects on the fragmented disc that most likely will induce random motion of the clumps of gas. King et al. (2008) assumed that the direction of the angular momentum of the gas clumps feeding the inner disc follows an isotropic distribution over 4π steradians. This corresponds to what is dubbed *chaotic accretion*.

On the other hand, Volonteri et al. (2007) proposed the so-called *coherent accretion*, in which the angular momentum of consecutive accretion episodes is aligned with one another. In the same fashion, Dubois et al. (2014) always align, in every accretion episode, the disc angular momentum with that of the surrounding gas. We follow this approach only in the coherent regime.

8. SPIN EVOLUTION OF SUPERMASSIVE BLACK HOLES

[Dotti et al. \(2013\)](#) assumed a somewhat intermediate approach, in which they assigned two probabilities, F and $1 - F$, for an accretion event to have its angular momentum pointing towards the northern or the southern hemisphere as defined by the galactic reference frame, respectively. Following this line of reasoning, we assume that the angular momentum imparted by the gas accreted from large scales is not completely erased. Nevertheless, considering that self-gravity is indeed a stochastic and complex process, the disc angular momentum should not be exactly aligned with the surrounding gas either. This is why we propose a novel approach in which the degree of anisotropy of the fuelling process can be varied, allowing its effects to be studied. In order to do so, we use the von Mises distribution function, a circular analogous of the normal distribution:

$$f(\theta|k) = \frac{e^{k \cos \theta}}{2\pi I_0(k)}, \quad (8.22)$$

where θ is the polar angle, k is the concentration parameter that quantifies the anisotropy degree and $I_0(k)$ gives the Bessel function of zeroth-order. The z -axis is still defined by the direction of the angular momentum of the surrounding gas.

In [Figure 8.2](#), we show different parameter choices for k . For instance, $k = 0$ corresponds to an isotropic distribution that recovers chaotic accretion. For $k = 10$, the distribution is very concentrated within the cone $\theta < \pi/4$ around the direction of the surrounding gas. For k sufficiently large, we recover the coherent accretion as well.

8.2.2 Coalescence of BH binaries

The second channel of evolution for BH spin corresponds to mergers of BHs. This is a common event in the hierarchical structure formation process, in which two merging galaxies ultimately form a deeper common potential well. After this, the two central BHs approach each through dynamical friction, form a binary, and finally coalescence. During the final inspiral phase, when the orbital angular momentum and energy are driven away by gravitational waves, we track the spin of BH remnants by using the analytical fit of [Rezzolla et al. \(2008\)](#), which is obtained from relativistic numerical simulations of coalescing binary Kerr BHs. The spin of the BH remnant can be expressed as:

$$\mathbf{a}^f = \frac{1}{(1+q)^2} (\mathbf{a}_1 + \mathbf{a}_2 q^2 + \ell q), \quad (8.23)$$

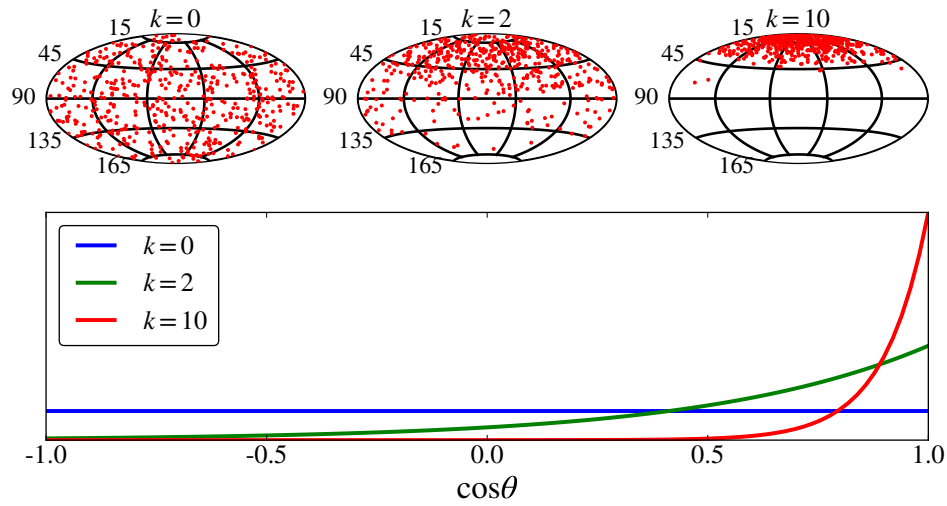


Figure 8.2: *Top panels:* Sky projections of the von Mises distribution for three different anisotropy degrees, ranging from complete isotropy ($k = 0$) to a more coherent distribution ($k = 10$). *Bottom panel:* PDF of the polar angle for the three choices of the anisotropy degree parameter illustrated in the upper panels.

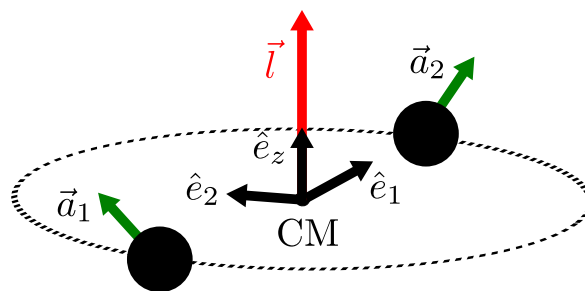


Figure 8.3: Reference system used in the calculation of the spin of the BH remnant and the recoil kick velocity imparted at coalescence time due to asymmetrical emission of gravitational waves.

8. SPIN EVOLUTION OF SUPERMASSIVE BLACK HOLES

where \mathbf{a}_1 and \mathbf{a}_2 correspond to the spin parameter vectors¹ of the more massive and less massive BHs, respectively; $q = M_2/M_1 \leq 1$ is the mass ratio of the BH binary; $\ell \equiv \ell'/(M_1M_2)$, with ℓ' corresponding to the difference between the orbital angular momentum \mathbf{l} when both BHs are widely separated from each other; and \mathbf{j}_{rad} is the angular momentum carried away by gravitational waves before coalescence, i.e. $\ell' = \mathbf{l} - \mathbf{j}_{\text{rad}}$.

We use the analytical expression derived by [Rezzolla et al. \(2008\)](#) for the norm of ℓ :

$$\begin{aligned} \ell = & \frac{s_4}{(1+q^2)^2} (a_1^2 + a_2^2 q^4 + 2\mathbf{a}_1 \cdot \mathbf{a}_2 q^2) \\ & + \left(\frac{s_5 \mu + t_0 + 2}{1+q^2} \right) (a_1 \cos \phi_1 + a_2 q^2 \cos \phi_2) \\ & + 2\sqrt{3} + t_2 \mu + t_3 \mu^2, \end{aligned} \quad (8.24)$$

where ϕ_1 and ϕ_2 are the angles subtended by the vectors \mathbf{a}_1 and \mathbf{a}_2 with respect to ℓ , respectively. The adopted numerical parameters are: $s_4 = -0.129$, $s_5 = -0.384$, $t_0 = -2.686$, $t_2 = -3.454$ and $t_3 = 2.353$.

In the same fashion as [Rezzolla et al. \(2008\)](#), we assume the orientation of ℓ to coincide with that of the total angular momentum of the BH binary before coalescence, i.e. $\mathbf{l} = \mathbf{l}_1 + \mathbf{l}_2$. This is computed directly from the positions and velocities of the two BHs, i.e. $\mathbf{l}_i = M_{\text{BH},i}(\mathbf{r}_i - \mathbf{r}_{\text{CM}}) \times (\mathbf{v}_i - \mathbf{v}_{\text{CM}})$, with $i = 1, 2$ and CM referring to the centre of mass of the binary.

Additionally, we also compute the recoil kick velocity imparted to the remnant due to the asymmetrical emission of gravitational waves at coalescence. We use the numerical fitting formula proposed by [Campanelli et al. \(2007\)](#):

$$\begin{aligned} \mathbf{v}_{\text{recoil}} &= v_m \hat{\mathbf{e}}_1 + v_{\perp} (\cos \xi \hat{\mathbf{e}}_1 + \sin \xi \hat{\mathbf{e}}_2) + v_{\parallel} \hat{\mathbf{e}}_z, \\ v_m &= A \eta^2 \sqrt{1 - 4\eta(1 + B\eta)}, \\ v_{\perp} &= \frac{H \eta^2}{(1+q)} (a_1^{\parallel} - q a_2^{\parallel}), \\ v_{\parallel} &= K \cos(\Theta - \Theta_0) \frac{\eta^2}{1+q} (a_1^{\perp} - q a_2^{\perp}), \end{aligned} \quad (8.25)$$

where $\hat{\mathbf{e}}_1$, $\hat{\mathbf{e}}_2$ are orthogonal unit vectors lying on the orbital plane, and $\hat{\mathbf{e}}_z$ is perpendicular to it, i.e. in the direction of the orbital angular momentum (see [Figure 8.3](#)). \perp and \parallel refer

¹This is a vector pointing in the direction of the BH spin, but with a magnitude given by the dimensionless spin parameter.

to vector components perpendicular and parallel to \hat{e}_z , Θ measures the angle between the vector $\mathbf{a}_1 - q\mathbf{a}_2$ and \hat{e}_1 , and $\eta \equiv q/(1+q)^2$ is the symmetric mass ratio. The adopted numerical parameters in these equations are: $A = 1.2 \times 10^4$ km/s, $B = -0.93$, $H = 7.3 \times 10^3$ km/s, $K = 6 \times 10^4$ km/s, $\xi = 1.536$ (88°) and $\Theta_0 = 0.184$.

8.3 Black Hole model

Modelling BHs in a cosmological context is a challenging task due to many fundamental uncertainties, including the nature of the non-linear coupling between galaxy formation and black hole properties; poorly understood and constrained models of mass accretion onto BHs and AGN-gas interactions; the inherent multi-scale physics of the problem, in which a comparatively small region around the BH impacts significantly larger scales in the host galaxy. These difficulties make an ab-initio treatment of small-scale BH physics within computational models of galaxy formation impossible with current numerical techniques and resources. Consequently, sub-grid approximations have to be adopted. Specifically, we use the fiducial BH model developed by [Weinberger et al. \(2017\)](#) and references therein. This BH model was adopted in the IllustrisTNG project as well.

8.3.1 Fiducial model

Our fiducial default model (based on [Weinberger et al., 2017](#)) comprises different aspects of BH physics that are crucial for modelling BH-galaxy co-evolution, namely BH growth, seeding of BHs in newly formed proto-galaxies, and feedback associated with BH accretion. In what follows, we describe the modelling of each of these aspects in turn.

Black hole growth

BHs gain mass and angular momentum through gas accretion from the ISM and mergers with other BHs. For gas accretion, we adopt the standard Bondi-Hoyle-Lyttleton formula ([Hoyle & Lyttleton, 1939](#); [Bondi & Hoyle, 1944](#); [Bondi, 1952](#)):

$$\dot{M}_{\text{Bondi}} = \frac{4\pi G^2 M_{\text{bh}}^2 \rho}{c_s^3}, \quad (8.26)$$

where ρ and c_s are the density and sound speed of the gas near the BH, respectively. When the accretion rate of the BH-disc system exceeds the Eddington rate, its value is capped as

8. SPIN EVOLUTION OF SUPERMASSIVE BLACK HOLES

follows:

$$\dot{M} = \min(\dot{M}_{\text{Bondi}}, \dot{M}_{\text{Edd}}), \quad (8.27)$$

where $\dot{M}_{\text{Edd}} \equiv L_{\text{Edd}}/\epsilon_r c^2$ and L_{Edd} is the Eddington luminosity as defined in the spin evolution model. For BH mergers, the masses of the two BHs in the coalescing BH binary are simply added up in the remnant, neglecting mass loss due to gravitational wave emission.

Black hole orbits

Due to our inability to resolve the local environment of each BH, it is not possible to accurately capture dynamical friction exerted by the background dark matter, gas and stars on the BHs. However, accounting for this process would be important for the correct computation of the BH orbits and the BH binary coalescence timescale. To circumvent this problem, the position of each BH is simply fixed to the local gravitational potential minimum of the host galaxy and its velocity is set to the mean mass-weighted velocity of the region. This has as a consequence that BH binary coalescence cannot be treated in a realistic fashion and a “numerical” coalescence must be implemented instead, i.e. two BHs merge once their relative separation is smaller than two softening lengths. Although this approach is simplistic and leads to underestimated BH coalescence timescales and fractions of free floating BHs, it is also numerically robust and prevents BHs to unrealistically migrate out of the centres of their host galaxies.

Note that we have provided an estimate of the recoil velocity in a BH binary coalescence in equation (8.25), however, this has no real impact on the BH population in the present set of simulations due to our special BH positioning scheme, i.e. BHs cannot recoil by construction. Therefore, we adopt the same approach as [Sijacki et al. \(2009\)](#), i.e. we compare the recoil velocity at coalescence time with the escape velocity of the host halo in order to assess the impact of our spin evolution model on the fraction of escaping BHs, which are the result of strong gravitational recoils. Mild gravitational recoils might not be powerful enough to expel a BH from its galaxy, but they can lead to off-centred BHs. As highlighted by [Sijacki et al. \(2011\)](#) and [Blecha et al. \(2011\)](#), BHs wandering off the galactic centre have a sizeable impact on the BH growth, increasing thus the scatter in the BH mass – host galaxy relationships. In future work we intend to include a sub-grid model of dynamical friction in order to study the impact of off-centred BHs more realistically (see also [Tremmel et al., 2015](#)).

Black hole seeding

Although virtually every galaxy hosts a supermassive BH, there is a significant theoretical uncertainty about the origin and early growth of these objects (e.g. [Volonteri 2010](#)). This makes it difficult to physically motivate models of BH seeding in simulations. Many recent hydrodynamical simulations of galaxy formation employ heuristic approaches, where a halo is seeded with an already massive BH upon fulfilment of a given condition, circumventing thus the phase of early growth. For instance, [Bellovary et al. \(2011\)](#) and [Tremmel et al. \(2017\)](#) seed BHs in locations where the local gas becomes dense, cold and has a low metal content. In the fiducial model of [Weinberger et al. \(2017\)](#) and in other previous works, a BH of mass M_{seed} is placed at the position of the potential minimum of any halo that exceeds a total mass M_{FOF} and does not contain a BH yet. Despite its simplicity, this method is relatively insensitive to the details of the early BH growth physics. It only assumes that this process is efficient enough to populate all halos with a low-mass supermassive black hole, whether or not this then grows further is a matter of the local conditions around it.

Black hole feedback

There is widespread theoretical consensus that there exist at least two types of accretion flows onto BHs (e.g. [Begelman 2014](#), and references therein). One type operates in BHs with high accretion rates and is associated with the formation of classical accretion discs ([Shakura & Sunyaev, 1973](#)). The second type occurs only in BHs with low accretion rates and produces a more spherical and hotter accretion flow ([Shapiro et al., 1976](#); [Ichimaru, 1977](#)). [Weinberger et al. \(2017\)](#) associate these types of accretion with two different BH feedback modes, namely a thermal quasar feedback mode that is activated during the high accretion state, and a kinetic feedback mode that operates in BHs with low-accreting BHs.

In the quasar mode, the energy liberated by the BH is injected thermally into the surrounding gas and is given by ([Springel et al., 2005](#)):

$$\Delta \dot{E}_{\text{high}} = \epsilon_{\text{f, high}} \epsilon_r \dot{M} c^2, \quad (8.28)$$

where, as previously defined, \dot{M} is the accretion rate of the BH-disc system and ϵ_r the radiative efficiency, which is spin-dependent in our case whereas in the fiducial model a fixed value $\epsilon_r = 0.1 - 0.2$ is commonly adopted. Finally, the parameter $\epsilon_{\text{f, high}}$ quantifies the efficiency of the energy coupling process to the local environment.

8. SPIN EVOLUTION OF SUPERMASSIVE BLACK HOLES

For the kinetic mode, the liberated energy is

$$\Delta \dot{E}_{\text{low}} = \epsilon_{\text{f, kin}} \dot{M} c^2, \quad (8.29)$$

where $\epsilon_{\text{f, kin}}$ is the coupling efficiency. Unlike the thermal quasar mode, the coupling process is mechanical, i.e. pure kinetic energy is injected into the gas without changing its temperature. This injection is isotropic when averaged in time, which yields a net conservation of linear momentum. Note that there is no dependence on the BH spin through ϵ_r as the low accretion state is thought to be radiatively inefficient. A direct spin dependence might, however, be present in reality, depending on the mechanism responsible of delivering the feedback energy in the kinetic mode. For instance, if small-scale jets produced by the Blandford-Znajek mechanism take place, the jet power has a direct dependence on the BH spin (Blandford & Znajek, 1977; Yuan & Narayan, 2014):

$$L_{\text{jet}} \propto B_{\text{pol}}^2 M_{\text{bh}}^2 a^2, \quad (8.30)$$

where B_{pol} is the poloidal magnetic field at the BH horizon. This scenario might also provide a third spin evolution channel as the rotational energy of the BH is drained by the jet. Nevertheless, in the fiducial model the kinetic feedback mode is assumed to be independent on the BH spin. In future work, we intend to return to this point and explore the consequences of including such a dependence, and also of injecting the kinetic feedback in the direction of the BH spin instead of using a random direction.

A remaining issue is the transition between the high and the low accretion modes, or equivalently, between the thermal quasar mode and the kinetic mode. Given the inability to resolve the small-scale accretion onto a BH, such transition cannot be self-consistently accounted for in cosmological simulations. Therefore, more effective approaches must be adopted instead. For instance, Sijacki et al. (2015) and other previous works have used a fixed threshold value of the fraction $\chi \equiv \dot{M}/\dot{M}_{\text{Edd}}$, i.e. when $\chi \lesssim \chi_{\text{th}}$ the low accretion mode is adopted, otherwise the BH is assumed to be in a high accretion state. This idea is extended in the fiducial model, and the threshold value is scaled with BH mass (Weinberger et al., 2017):

$$\chi_{\text{th}} = \min \left[\chi_0 \left(\frac{M_{\text{bh}}}{10^8 M_{\odot}} \right)^{\beta}, 0.1 \right], \quad (8.31)$$

with χ_0 and β free parameters that are calibrated to reproduce observational trends.

8.3.2 Self gravity in the accretion disc as a switch of BH kinetic feedback

The implementation of a kinetic BH feedback mode in the IllustrisTNG simulations has proven to be extremely important to simultaneously account for quenching of star formation and correct gas abundances in high mass galaxies (Weinberger et al., 2017, 2018). Nevertheless, apart from the notion that the kinetic BH feedback mode occurs in massive galaxies, the exact conditions under which it operates remain unknown. This uncertainty is addressed in the fiducial model by adopting an *ad hoc* feedback switch (equation 8.31) that is calibrated to reproduce observational trends. An important example for the outcome of this is the strong galaxy colour bimodality in IllustrisTNG, which is remarkably consistent with observations (Nelson et al., 2018). This represents a major improvement with respect to the first generation of Illustris simulations, in which the galaxy colour bimodality was much weaker (Nelson et al., 2015).

In spite of many encouraging successes, there are still some tensions between IllustrisTNG and observations. For example, Rodriguez-Gomez et al. (2019) report a galaxy morphology – colour relation that is inconsistent with observations, i.e. there is an excess of red discs and blue spheroids in the simulations. This discrepancy might be caused by the limited mass resolution of the simulations, which seems to be insufficient to produce starbursts (Sparre & Springel, 2016). Given that galaxy mergers trigger starbursts and drive morphological changes, and that post-merger galaxies tend to have a quiescent star forming activity, the inability to produce starbursts might naturally lead to a lacking connection between galaxy morphology and colour. Rodriguez-Gomez et al. (2019) suggest that the missing link is BH gas accretion during galaxy mergers. They argue that the limited mass resolution likely causes an underestimation of merger-induced gas inflows that feed central BHs. This would ultimately lead to an under-powered BH feedback and a potential excess of blue spheroids due to poor quenching. Nevertheless, we note that the BH mass – stellar mass relation is well reproduced in IllustrisTNG (Weinberger et al., 2018), which means that BHs are not significantly underfed. Therefore, gas accretion is not likely the source of the problem.

An alternative explanation of the tension in the morphology – colour relation could lie in the use of an inadequate BH feedback switch. Recall that the colour bimodality is well reproduced in IllustrisTNG (Nelson et al., 2018), demonstrating that the kinetic BH feedback mode is an efficient quenching mechanism. However, the inconsistent morphology means that the BH feedback switch is selecting the wrong galaxy population to quench. Thus,

8. SPIN EVOLUTION OF SUPERMASSIVE BLACK HOLES

spheroids that should be quenched but are not, become blue, and discs that are quenched but should not, become red. The origin of this problem might be related to the *ad-hoc* nature of the fiducial BH feedback switch, and its lack of a physical connection to the galaxy morphology. In this case it would be very difficult, if not impossible, to calibrate equation (8.31) to also reproduce the morphology – colour relation in the simulations.

In order to construct a more physically motivated BH feedback switch, we start from the notion that there are two different BH accretion modes (Begelman, 2014). A high accretion mode, in which a radiatively efficient thin disc develops; and a low accretion mode, in which the accretion flow is spherical, hot, and radiatively inefficient. We note that these modes closely resemble the coherent and self-gravity regimes of the accretion disc in the BH spin evolution model (see Section 8.2). The coherent accretion regime is compatible with the formation of a classical Shakura-Sunyaev disc in the high accretion mode, whereas the fragmentation of the disc in the self-gravity regime provides an ideal scenario for the spherical hot accretion flow in the low accretion mode. Following Weinberger et al. (2017), we associate the quasar thermal feedback mode with the coherent regime (high accretion mode), and the kinetic feedback mode with the self-gravity regime (low accretion mode). Therefore, we can use the self-gravity condition $R_{\text{sg}} \leq R_{\text{warp}}$ as a BH feedback switch. A similar scenario is proposed by Garofalo et al. (2010), in which merger-induced retrograde accretion onto a BH is much more efficient in producing non-thermal jet outflows. Note that our argument is a mere working hypothesis, meant to explore the still poorly understood physical connection between BH accretion and BH feedback. Nonetheless, our approach does not require calibration, and self-consistently predicts the activation of the kinetic feedback mode based only on the physical properties of BHs, which represents a big improvement with respect to previous *ad-hoc* schemes.

Starting from the condition $R_{\text{sg}} \leq R_{\text{warp}}$, we can derive a parametric equation for the mass threshold $M_{\text{bh,th}}(\dot{M}, a)$ at which the transition from the coherent regime to the self-gravity regime occurs. In order to do so, we use equations (8.12) and (8.20) for the warp radius $R_{\text{warp}}(M_{\text{bh}}, \dot{M}, a)$ and the self-gravity radius $R_{\text{sg}}(M_{\text{bh}}, \dot{M}, a)$, respectively. In Figure 8.4, we show the BH mass – Eddington ratio diagram with two different mass thresholds for two extreme values of the spin parameter, i.e. $M_{\text{bh,th}}(\dot{M}, a = 0.998)$ and $M_{\text{bh,th}}(\dot{M}, a = 0.001)$. For comparison purposes, we also show the mass threshold associated to the BH feedback switch of the fiducial model (we use $\chi_0 = 0.002$ and $\beta = 2.0$ as in Weinberger et al., 2017).

In this figure, we also sketch the evolutionary path of a maximum spinning BH of mass

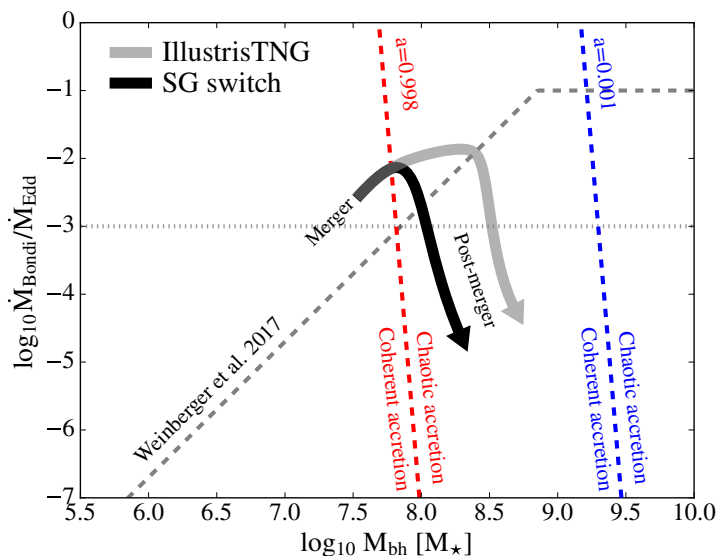


Figure 8.4: Diagram of Eddington ratio vs BH mass illustrating different BH feedback switches. The dashed red ($a = 0.998$) and blue ($a = 0.001$) lines correspond to the transition between coherent and chaotic accretion based on the self-gravity of the accretion disc, as proposed here. The grey dashed line corresponds to the switch between the quasar and kinetic BH feedback modes adopted by [Weinberger et al. \(2017\)](#).

$\sim 10^8 M_{\odot}$ ¹ during a galaxy merger. The grey arrow represents what happens if the fiducial BH feedback switch is adopted. Likewise, the black arrow represents the BH evolution if the self-gravity switch is used instead. Considering that, during a galaxy merger, the central BH experiences a boosted growth due to gas accretion and/or coalescence with a second BH, both quantities, BH mass and Eddington ratio, will unavoidably increase. This sets a specific direction of evolution in the diagram. Adopting the self-gravity switch will clearly favour quenching of post-merger galaxies compared to the fiducial switch. This, in conjunction with merger-induced morphological changes, might help recovering the colour-morphology relation in the simulation. We also note that galaxies hosting BHs with lower spin values will be quenched at higher stellar masses.

Some high redshift quasars exhibit extremely large BH masses ($M_{\text{bh}} \gtrsim 10^9 M_{\odot}$) and high accretion rates. The kinetic feedback mode should clearly not be operating under these conditions as it would expel most of gas content of the host galaxy, so the thermal quasar

¹According to the BH mass – stellar mass relation ([Kormendy & Ho, 2013](#)), a BH mass of $\sim 10^8 M_{\odot}$ corresponds to a galaxy stellar mass of $\sim 10^{10} M_{\odot}$, which is roughly the mass scale above which quenching becomes efficient and galaxies migrate to the red sequence.

8. SPIN EVOLUTION OF SUPERMASSIVE BLACK HOLES

mode must be operating instead. The fiducial model solves this by specifying an upper limit for the Eddington rate ($\dot{M}/\dot{M}_{\text{Edd}} = 0.1$) for the kinetic feedback mode to operate.

For the self-gravity switch, a self-consistent solution might instead emerge out of the spin evolution model. Once the self-gravity regime is reached, the kinetic feedback mode is activated and most of the central gas is heated and/or pushed away. This results in a significant decrease of the BH accretion rate and a suppression of the gas evolution channel. After this, only BH binary coalescence can alter the spin. Nevertheless, if a gas-rich event manages to substantially increase the BH accretion rate again, the BH will quickly be spun down, thereby increasing the BH mass threshold of the self-gravity switch and activating again the thermal quasar mode. Additionally, if a spin dependent kinetic feedback based on the Blandford-Znajek mechanism were operating (equation 8.30), a BH with a decreasing spin would weaken the feedback energy as $L_{\text{jet}} \propto a^2$, thereby aiding further accretion. The feasibility of this scenario is yet to be tested in full; the low abundance of these objects demands simulations of large cosmological volumes at at least moderate resolutions, which is out of the scope of this work.

8.4 Numerical Set-up

8.4.1 Simulation Code

We run cosmological simulations to self-consistently track the spin evolution of supermassive black holes along with other quantities of interest such as BH mass accretion rate, BH feedback and properties of the host galaxies. We use the N -body magneto-hydrodynamics moving-mesh code AREPO (Springel, 2010) to solve the non-linear system of differential equations describing gas hydrodynamics and gravitational interactions of dark matter and baryons in such simulations. One of the unique features of AREPO is that the mesh continuously transforms and flows along with the fluid, unlike in standard grid-based methods. This is achieved through a dynamic unstructured mesh that is constructed as the Voronoi tessellation of a set of mesh-generating points that move with the local fluid velocity. This ensures that every cell approximately maintains a given target mass, and in this fashion, regions of high density are resolved automatically with smaller cells than low density regions, which is crucial for modelling processes such as gas accretion onto BHs residing in high density galaxy centres. Furthermore, because the mesh moves with the fluid, the advection errors inherent in Eulerian mesh codes are strongly reduced. In fact, a discretization that is

manifestly Galilean invariant is achieved in this way. Also, there are no preferred coordinate directions in this scheme, avoiding potential spurious alignments of gas structures with the grid, as it can happen in Cartesian mesh codes when the resolution is low. This helps in accurately tracking the co-evolution of the spin of BHs and the angular momentum of the gas surrounding BHs in an isotropic way.

Gravitational forces in AREPO are calculated using the Tree-PM scheme (Xu, 1995), in which long-range forces are computed with a particle-mesh method and short-range forces are followed via a hierarchical octree algorithm (Barnes & Hut, 1986). Apart from gravitational interactions and hydrodynamics, the code incorporates a complete physics model that includes: gas cooling of primordial and metal lines; a sub-resolution ISM model based on the two phase medium (Springel & Hernquist, 2003), in which stars are formed in a stochastic fashion above a density threshold of 0.13 cm^{-3} ; stellar evolution; chemical enrichment; gas recycling; kinetic stellar feedback driven by SNe and black hole physics (section 8.3).

8.4.2 Numerical implementation of spin evolution

As discussed in Section 8.2, the BH spin parameter a can be computed in an iterative fashion through equation (8.8); however, an initial condition a_0 is still required. Hence, we assign an initial spin value a_0 to every BH seed. Once initialised, if a BH seed accretes gas above 1% of its Eddington rate, the gas evolution channel is activated. In what follows, we discuss how to integrate BH spin evolution through gas accretion into the AREPO code.

The density and the direction of the angular momentum of the gas around BHs are needed to compute the mass accretion rate (equation 8.26) and the direction of the BH spin (equation 8.14). In order to estimate these properties, we use a spherical SPH kernel $w(r; h)$ around each BH that encloses a prescribed number of gas cells n_{ngb} in a radius h :

$$n_{\text{ngb}} \approx \sum_i \frac{4\pi h^3 m_i}{3 m_{\text{baryon}}} w(r_i). \quad (8.32)$$

Here, m_{baryon} is the target mass of a gas cell and i runs over the cells within the kernel radius.

One important issue that needs to be addressed concerns the time integration of the spin evolution. On the one hand, gravitational interactions and gas hydrodynamics fix the evolution time step Δt for every particle/gas cell of the simulation (Springel, 2010). For

8. SPIN EVOLUTION OF SUPERMASSIVE BLACK HOLES

BHs, this time step determines how often properties such as M_{bh} , \dot{M} and the direction of the angular momentum of neighbouring gas are updated. On the other hand, the BH spin is updated after an accretion timescale t_{acc} has elapsed in the coherent regime, or after the disc has accreted a mass M_{sg} in the self-gravity regime. This implies that processes such as BH growth and BH feedback, which are governed by Δt in the code, are not necessarily synchronised with the evolution of BH spin. This leads to four different cases:

- (i) *BH in coherent regime, $t_{\text{acc}} < \Delta t$* : in this case, several accretion episodes occur within the same time step. At the beginning of the time step, we store the BH properties needed for the spin model, and they are used for every accretion episode occurring within that time step. We also set a cumulative time counter that keeps track of how many accretion episodes have been completed. We stop once the counter equals Δt and proceed to the next time step.
- (ii) *BH in coherent regime, $t_{\text{acc}} > \Delta t$* : in this case, several time steps elapse in the same accretion episode. We set a time counter at the beginning of the accretion episode that keeps track of how many time steps have been completed. We stop once the counter equals t_{acc} and proceed to the next accretion episode. The input BH properties for the spin model are averaged over the elapsed time steps.
- (iii) *BH in self-gravity regime, $M_{\text{sg}} < \dot{M}\Delta t$* : this case is similar to *case (i)*, i.e. several accretion episodes occur within the same time step. Given that the BH spin must be updated once a mass M_{sg} is swallowed by the BH, we set, at the beginning of the time step, a cumulative mass counter that keeps track of how many times this has happened. We stop once the mass counter equals $\dot{M}\Delta t$ and proceed to the next time step. The BH properties are assumed constant for all the accretion episodes in this time step.
- (iv) *BH in self-gravity regime, $M_{\text{sg}} > \dot{M}\Delta t$* : this case is similar to *case (ii)*. At the beginning of the accretion episode, we set a cumulative mass counter that keeps track of how much mass is accreted in every time step. We stop once the mass counter equals M_{sg} and proceed to the next accretion episode. The BH properties are averaged over the elapsed time steps.

At the beginning of every accretion episode, we compute R_{warp} , R_{sg} , t_{acc} and M_{sg} . This allows us to assess which of the previous cases applies. At the end of an accretion episode, we update the BH spin.

Simulation	Spin model	k	Feedback switch
1	No	-	Fiducial
2	Yes	0	Fiducial
3	Yes	2	Fiducial
4	Yes	10	Fiducial
5	Yes	0	Self-gravity

Table 8.1: Overview of our primary cosmological simulation models. For all the simulations, we employ the physics model of IllustrisTNG with some modifications with respect to our new spin model and treatment of the BH feedback switch. Simulation 1 is used as a control for comparison purposes and corresponds to the unmodified IllustrisTNG model.

The second evolution channel, BH binary coalescence, can be easily integrated into the code as BH mergers are treated in an instantaneous fashion. This makes it straightforward to apply equation (8.23) to compute the spin of the BH remnants.

8.4.3 Simulation set

We run a set of 5 cosmological simulations in a periodic box with side length of $25 h^{-1}$ Mpc. This is a relatively small size compared to state-of-art cosmological simulations like Illustris (Vogelsberger et al., 2014), IllustrisTNG (Pillepich et al., 2018; Springel et al., 2018) or Eagle (Schaye et al., 2015); however, we still form around 1200 BHs, with roughly 60 of them being more massive than $10^8 M_{\odot}$. This makes our simulations suitable to sample the evolution of BH spin in the coherent and self-gravity regimes. For simulation 1, we do not use our BH spin evolution model as this is the control simulation used for comparison purposes. For simulations 2, 3 and 4, we use our self-consistent BH spin evolution model with different values of the parameter k . BH feedback and BH growth are affected by BH spin owing to the spin-dependent radiative efficiency of the accretion disc. Besides, we use the fiducial feedback switch as we want to isolate the effects of BH spin evolution. We show the results of these three simulations in Section 8.5. Finally, simulation 5 is run with the BH spin model as well, but additionally, we use our BH feedback switch based on the self-gravity of the accretion disc. The results of this simulation are discussed in Section 8.6. We summarise the model choices for our simulations in Table 8.1.

For all our simulations, we adopt a Λ CDM cosmology consistent with the Planck intermediate results (Planck Collaboration et al., 2016), given by $\Omega_M = 0.3089$, $\Omega_{\Lambda} = 0.6911$, $\Omega_b = 0.0486$, $h = 0.6774$ and $\sigma_8 = 0.8159$. Initial conditions are generated by using an Eisenstein & Hu (1998) power spectrum starting at redshift $z = 127$. The initial conditions

8. SPIN EVOLUTION OF SUPERMASSIVE BLACK HOLES

contain 512^3 dark matter particles and the same number of gas cells. This corresponds to a mass resolution of $8.4 \times 10^6 h^{-1} M_\odot$ and $1.5 \times 10^6 h^{-1} M_\odot$ for dark matter particles and gas cells, respectively, which is similar to the highest resolution of Illustris TNG100 (Pillepich et al., 2018). The softening length for gas cells, dark matter and star particles is 1 comoving kpc with a maximum value of 0.5 proper kpc. For the black hole model, we adopt the following parameters: $M_{\text{FOF}} = 5 \times 10^{10} h^{-1} M_\odot$, $M_{\text{seed}} = 8 \times 10^5 h^{-1} M_\odot$, $\epsilon_{\text{f, high}} = 0.1$, $\epsilon_{\text{f, kin}} = 0.2$, $\epsilon_r = 0.2$ (only for fiducial run), $\chi_0 = 0.002$, $\beta = 2.0$ and $n_{\text{ngb}} = 128$. For the spin evolution model, we use $\alpha = 0.1$ and $a_0 = 0$.

8.5 Black hole spin in cosmological simulations

8.5.1 Individual histories

Before discussing the main demographic results of the BH population in our simulations, it is instructive to examine individual BH histories and how they relate to the spin evolution. In Figures 8.5 and 8.6, we show two representative cases of the BH evolution. The first example is a very massive BH of mass $10^{8.8} - 10^9 M_\odot$ ¹ residing in a galaxy of stellar mass $1.1 \times 10^{11} M_\odot$. This BH is seeded at a redshift $z = 8.3$ (lookback time of 13.12 Gyr) when its host halo reaches the threshold mass M_{FOF} . The BH survives until $z = 0$, i.e. it does not merge with any more massive BH throughout its history.

The evolution of the spin parameter is shown in the top panel of Fig. 8.5. Once the BH is seeded, we find that gas accretion takes about 500 Myr to spin up the BH to the maximum spin value. Especially in the last 100 Myr of this period, from lookback time 12.8 Gyr to 12.7 Gyr, the spin parameter increases very quickly, which is due to the accretion disc being in the coherent regime and the BH reaching the Eddington accretion rate (bottom panel). This is also accompanied by a rapid increment of the radiative efficiency from $\sim 5\%$ to $\sim 30\%$ (third panel), which represents an enhancement of a factor of six in the supplied feedback energy per unit of accreted mass.

For this BH, the coherent accretion regime extends up to $z = 3.6$ (blue shade). During this time, every accretion episode is by construction aligned with the surrounding gas of the BH. Although this type of accretion is more stable than the chaotic counterpart, the orientation of the gas angular momentum can still fluctuate considerably, which is seen in the

¹We report a range of BH masses because the anisotropy degree k of the feeding process is varied in each simulation, which yields slightly different mass values even though we show the same black hole in each case.

8.5 Black hole spin in cosmological simulations

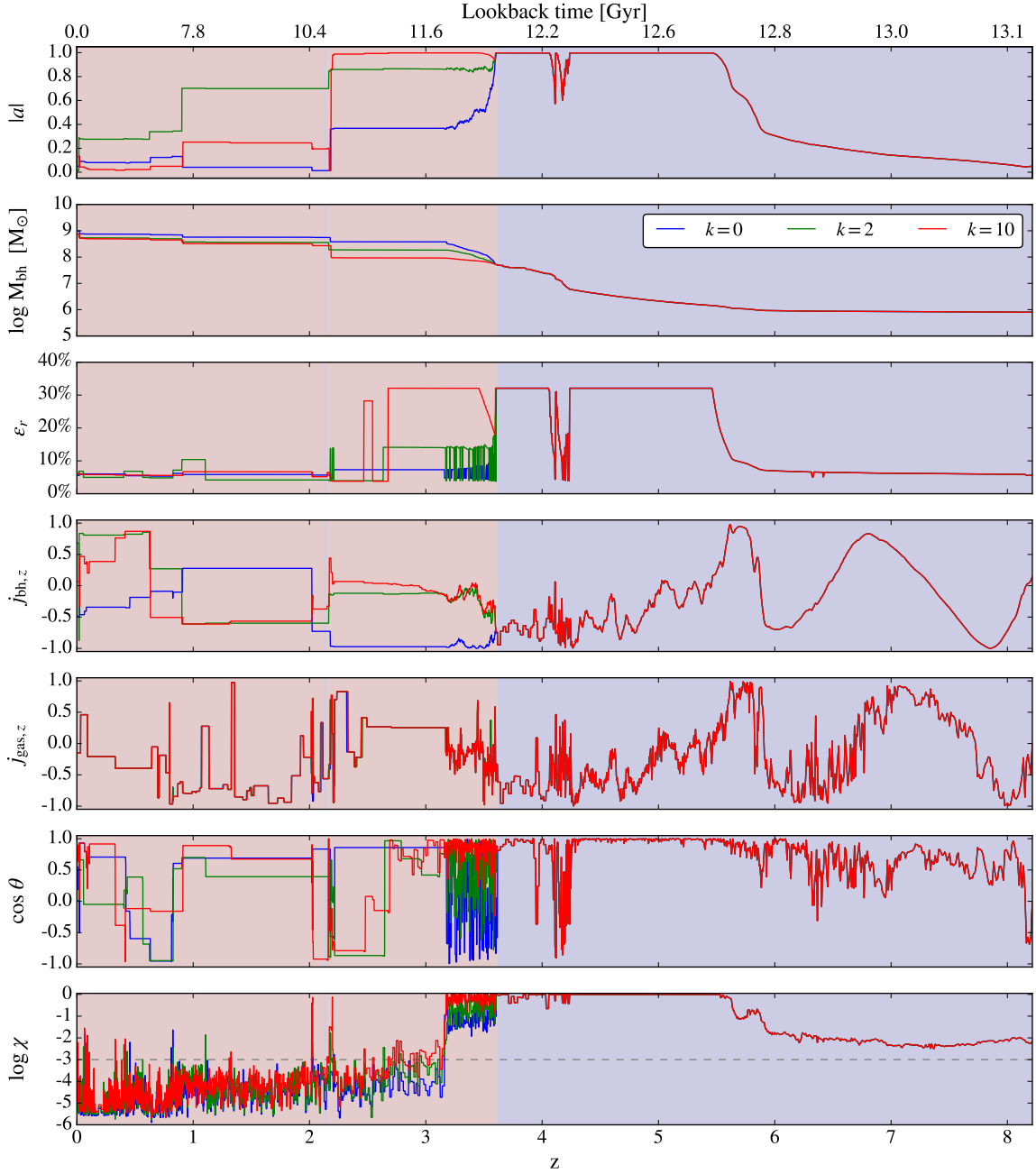


Figure 8.5: Example of the evolution of several BH properties for one of the BHs in our simulations. We track the evolution of this BH for different choices of the concentration parameter k , which quantifies the degree of anisotropy in the feeding process. The BH masses at $z = 0$ in the different models lie in the range $10^{8.8} - 10^9 M_{\odot}$. *From top to bottom:* BH spin evolution, BH mass evolution, radiative efficiency, Cartesian z -component of the normalised BH spin vector, Cartesian z -component of the normalised angular momentum vector of the surrounding gas, cosine of the angle between these two vectors, and finally, the Eddington ratio. The z -axis corresponds to the fixed reference frame of the simulation. The *blue shade* and the *red shade* represent the coherent and self-gravity accretion regimes, respectively.

8. SPIN EVOLUTION OF SUPERMASSIVE BLACK HOLES

evolution of the Cartesian z -component of the angular momentum $j_{\text{gas},z}$ (fifth panel). Owing to the high mass accretion rate of the disc in the coherent regime, the angular momentum transferred to the BH in every accretion episode is sufficient to keep the BH spin mostly oriented with the gas. This explains why the z -projection of the BH spin, $j_{\text{bh},z}$, mimics the global behaviour of $j_{\text{gas},z}$ (fourth panel), and why the angle θ is small (sixth panel). Small fluctuations in \dot{j}_{gas} cannot be followed up by the BH spin as they occur on timescales smaller than the accretion timescale t_{acc} , which in turn has a lower limit imposed by the Eddington rate at a given BH mass and spin, i.e. corresponding to $\lambda = 1$ in equation (8.13).

Between $z = 4.3$ and $z = 4$, the host galaxy experiences a merger with a smaller galaxy (stellar mass ratio 1:4). This event disturbs the central gas considerably and is reflected in the rapid and violent fluctuations in $j_{\text{gas},z}$ (Mayer et al., 2007). Although the BH is already accreting at its Eddington rate during this time, in this particular case the BH spin is not reoriented fast enough to keep up with the gas fluctuations. This creates an interesting situation in which the BH spin is suddenly misaligned, and counter-rotating accretion takes place even in the coherent regime, i.e. for $\cos\theta < 0$. The spin parameter drops to lower values as the BH is spun down, and thus the radiative efficiency decreases to 5% as well. Due to the self-consistent nature of our model, the BH mass is also impacted during this time and its growth is temporarily boosted (second panel). Note that this behaviour cannot be accounted for in a static model with constant ϵ_r . We remark that these fluctuations of the gas angular momentum are resolved in the simulation and driven by local turbulence (Dubois et al., 2014). Therefore, they are different than those produced by internal processes in the accretion disc during the self-gravity regime. Once the merger has completed, the central gas becomes stable again and the BH spin rapidly reaches the maximum value.

In general, during the coherent regime the orientation of the BH spin tends to be more stable over time than the angular momentum of the central gas, which allows to interpret the former as a time average of the latter. This might have interesting consequences for the alignment of the BH spin with the host galaxy and the cosmological environment as several processes funnel gas towards the galactic centre from galactic and extra-galactic reservoirs. We defer an analysis of this point to future work.

The self-gravity regime kicks in at $z = 4.6$ once the condition $R_{\text{sg}} \leq R_{\text{warp}}$ is satisfied. At this point, the concentration parameter k starts to considerably impact the evolution of the BH. For a fully chaotic accretion ($k = 0$), the BH spin does not follow the gas angular momentum anymore, and thus its magnitude rapidly decreases as counter-rotating accretion episodes become very frequent. This reduces the radiative efficiency of the disc and

enhances mass growth. For a very coherent accretion ($k = 10$), the BH behaves similarly as during the coherent regime. Medium concentrations (e.g. $k = 2$) yield a somewhat intermediate behaviour, i.e. the BH is fairly aligned with the gas angular momentum, but counter-rotating accretion episodes can still occur occasionally. At $z = 3.2$, the kinetic feedback mode is activated and the central gas is quickly heated up and swept away, hence the gas accretion channel is suppressed and only BH binary mergers can significantly alter the BH mass and spin. We note that during the self-gravity regime, $j_{\text{gas},z}$ appears to display a discontinuous behaviour. This is, however, a spurious effect due our recording of all relevant BH properties only when the BH spin is modified, which is done for computational reasons.

Finally, we show in Figure 8.6 a second example of a more quiescent BH of mass $10^{7.8} M_{\odot}$ formed at $z = 6.05$, residing in a galaxy of stellar mass $1.2 \times 10^{10} M_{\odot}$. The evolution of this BH is in part very similar to the previous one, e.g., during the coherent regime, the spin parameter eventually reaches the maximum allowed value while the BH spin is, with a few exceptions, mostly oriented with the gas angular momentum. Nevertheless, as this BH almost never reaches its Eddington rate, its whole evolution is considerably slower. A very interesting aspect is that a major galaxy merger at $z = 0.7$ (stellar mass ratio 1:2) triggers both the self-gravity regime and the kinetic feedback mode at the same time, hinting thus a possible connection between these two processes. We explore this hypothesis more thoroughly in Section 8.6.

8.5.2 Black Hole demographics

Black hole spin distribution

Having shown how the spin model works in individual BHs, we proceed to study the demographics of the BH population in our simulations. We start by analysing the distribution of the absolute value of the BH spin as a function of BH mass. We plot in Figure 8.7 the results for simulations 2, 3 and 4, which include the spin model, but which use different values for the concentration parameter k .

One common result is the initial monotonic growth of the spin for BHs with masses of $10^6 - 10^{6.5} M_{\odot}$, i.e. right after they are seeded. The small dispersion during this first phase indicates that all BHs follow the same path, i.e., at the beginning, BH spin evolution depends mainly on BH mass, no matter how fast the mass is accreted. This behaviour is explained by the explicit mass dependence in equation (8.8), and the ease with which the spin of a

8. SPIN EVOLUTION OF SUPERMASSIVE BLACK HOLES

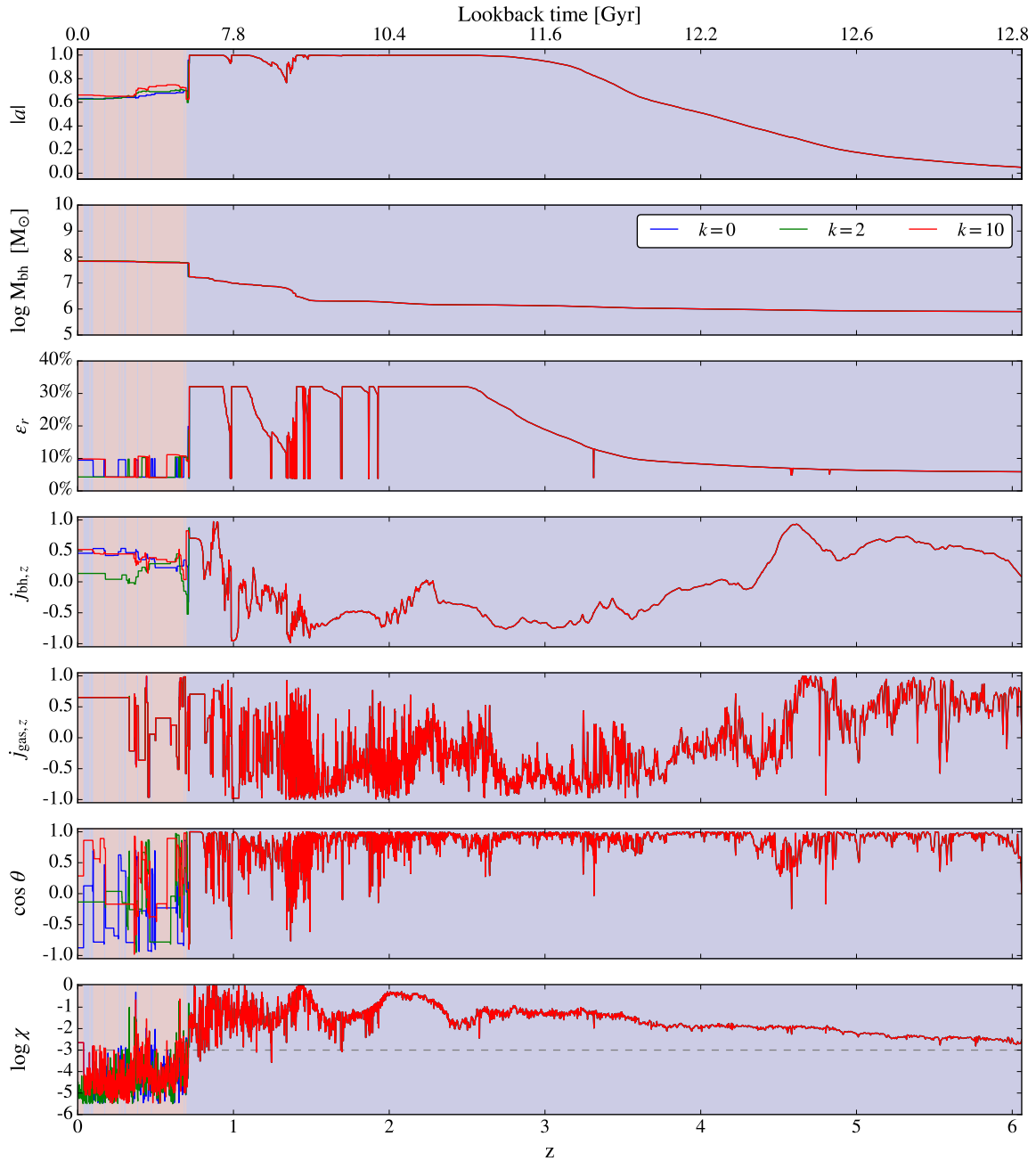


Figure 8.6: Illustrative evolution example of a BH of mass $10^{7.8} M_{\odot}$ with a more quiescent history. The properties shown are the same as in Fig. 8.5.

8.5 Black hole spin in cosmological simulations

low-mass BH can be reoriented during an accretion episode, i.e. counter-rotating accretion is very unlikely to occur and the BH always gets spun up. For masses larger than $10^{7.5} M_{\odot}$, the spin decreases to intermediate values and the distribution becomes more homogeneous. This is caused by BH binary coalescence and BHs entering the self-gravity regime, in which the frequency of counter-rotating accretion episodes is controlled by the concentration parameter. Approximately at this mass scale, the kinetic feedback mode kicks in as well, which limits gas accretion and leaves BH coalescence as the only effective spin evolution channel. This also explains why the different choices of the concentration parameter do not affect the spin distribution considerably, i.e. the gas evolution channel is briefly active during the self-gravity regime. From now on, we adopt for definiteness in all our analysis the chaotic accretion in the self-gravity regime as the default mode, i.e. we use only the simulations with $k = 0$.

Although direct observational measurements of BH spins are difficult and challenging to obtain, there have been several attempts made through X-ray spectroscopy of the iron fluorescence line of the accretion disc. [Reynolds \(2013\)](#) made a compilation and a quality assessment of the measurements, which is necessary due to several contradictory results. We include these data in Figure 8.7 (orange diamonds) and compare them with our BH spin distribution. We find a very good agreement, i.e. spins tend to have a high value at intermediate BH masses, but they decrease for more massive BHs. Our results are also consistent with previous numerical studies of spin evolution in a cosmological context (e.g. [Dotti et al., 2013](#); [Dubois et al., 2014](#)).

In order to test the robustness of our results, we have run simulations with different initial spin values, namely $a_0 = 0.5$ and $a_0 = 0.9$. In all cases, the spin distributions for masses larger than $10^{6.5} M_{\odot}$ were almost identical, thereby demonstrating the insensitivity of the model on the initial conditions. This can be easily explained by the fact that BH binary mergers become common for massive BHs, and thus they rapidly erase any trace of the initial conditions and introduce a large dispersion in the spin distribution. Counter-rotating accretion also aids this as it becomes increasingly more likely to occur and is a relatively stochastic process.

Black hole mass – stellar mass relation

Amongst the achievements of the IllustrisTNG project and its kinetic BH feedback mode is the reproduction of the BH mass – stellar mass relation ([Weinberger et al., 2017, 2018](#)).

8. SPIN EVOLUTION OF SUPERMASSIVE BLACK HOLES

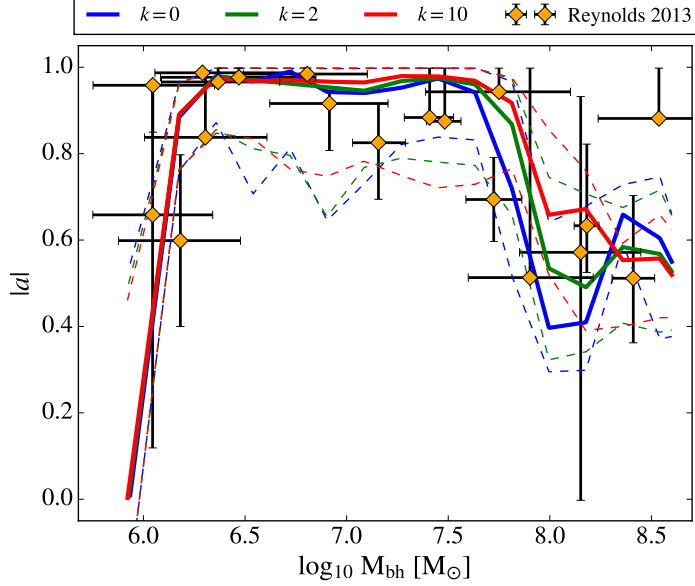


Figure 8.7: Median of the absolute BH spin value distribution as a function of BH mass at $z = 0$ (solid lines) for three different values of the concentration parameter k that quantifies the anisotropy of the feeding process. Dashed lines represent 25% and 75% percentiles. Orange diamonds with 1σ bars are observational data compiled by Reynolds (2013).

Given that our spin model has a direct impact on BH accretion and the associated feedback through the spin-dependent radiative efficiency, we investigate how it affects the BH mass – stellar mass relation and the BH mass function. These are shown in Figure 8.8, top and bottom panels, respectively. In order to more easily understand the effects of spin evolution alone, we do not consider the full model with the self-gravity feedback switch in this discussion (rightmost panels), i.e. we exclude simulation 5.

Using the fiducial model as a reference, we find that the BH mass – stellar mass function in our model follows the same trend and is consistent with the observational fit of Kormendy & Ho (2013). A pronounced change in the accretion rate in the BH population at BH masses of about $10^8 M_{\odot}$ appears in both simulations as consequence of the fiducial feedback switch (equation 8.31). Given that the radiative efficiency has a strong non-linear dependence on the spin parameter (equation 8.10), periods of chaotic accretion can alter the BH mass accretion history significantly. This is evinced in the larger dispersion in the relation for our model. However, we remark that gas accretion is still self-regulated correctly by feedback for BH masses smaller than $10^8 M_{\odot}$ since the global slope of the relation is preserved. For BH masses larger than $10^8 M_{\odot}$, gas accretion is suppressed and mass growth is driven by mergers with lower mass BHs, which naturally leads to a scaling relation.

For the BH mass function, both simulations exhibit similar trends that are consistent with the observational constraints compiled by [Shankar \(2009\)](#) from X-ray and optical measurements. The only obvious discrepancy with observations is the overabundance of BHs of masses of $10^{7.8} - 10^8 M_{\odot}$ present in both the fiducial model and our model. In order to check the validity of this finding, we recall the observational galaxy colour – stellar mass relation and the redshift independent transition from the blue to the red sequence at a stellar mass of about $10^{10} M_{\odot}$ ([Baldry et al., 2006](#); [Peng et al., 2010](#)). This stellar mass scale corresponds to a BH mass of $10^8 M_{\odot}$ according to the BH mass – stellar mass relation ([Kormendy & Ho, 2013](#)), which implies that the activation of an efficient quenching mechanism (e.g. our kinetic feedback mode) must occur precisely at the BH mass scale at which we find the BH overabundance in our simulations. We hypothesise that the origin of this feature is the suppression of gas accretion induced by kinetic feedback at this specific mass scale, which causes a “bottleneck” effect in BH growth as BH binary coalescence is abruptly left as the only active mass accretion channel.

We also compute separately the mass function of BHs that have been in the kinetic feedback mode at least once during their lifetime (red histograms) and BHs that have been always in the quasar feedback mode (blue histograms). We obtain again almost an identical result as in the fiducial model. For instance, we find that the red histograms extend over almost the entire BH mass range, which means that the kinetic feedback mode plays always a role in BH growth. However, for low mass BHs, this role is subdominant as this mode only fully kicks in for BHs more massive than $10^8 M_{\odot}$. We return to this result in [Section 8.6](#) as it represents one of the more significant differences when our full model with the self-gravity feedback switch is used.

8.5.3 Galaxy mergers and BH binary coalescence

In this subsection, we study the effects of our spin model on the population of coalescing BH binaries. We start by analysing the evolution of different BH properties during galaxy mergers. In order to do so, we centre every BH binary history at the BH coalescence time, with negative values indicating pre-merger stages. We finally stack all individual profiles to obtain general trends. For pre-merger stages, we restrict our analysis to the most massive BH of each binary, with the additional constraint of being in the quasar feedback mode before coalescence. This guarantees that gas accretion is still active. We show the results in [Figure 8.9](#).

8. SPIN EVOLUTION OF SUPERMASSIVE BLACK HOLES

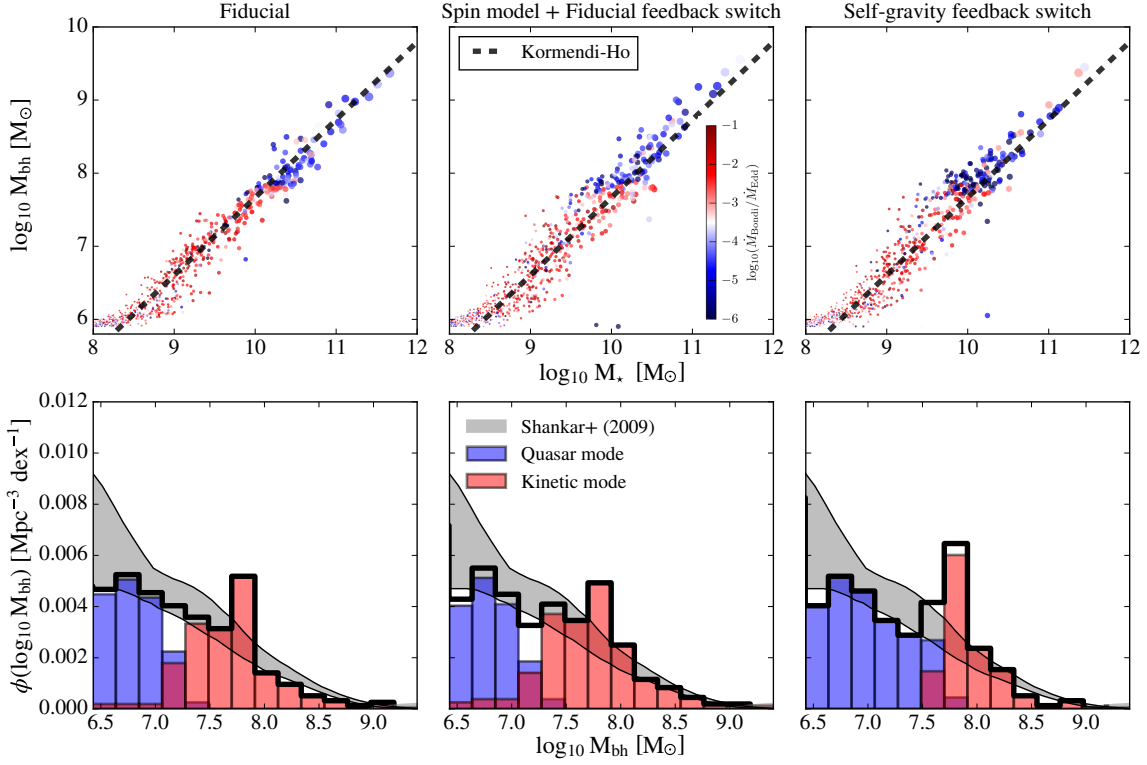


Figure 8.8: BH mass – stellar mass relation (*top panels*) and BH mass function (*bottom panels*) at $z = 0$ for three different models, namely the fiducial model (*left panels*), our spin model with the fiducial feedback switch (*central panels*) and our full model that includes the self-gravity feedback switch (*right panels*). For the *top panels*, colour encodes the Eddington rate and the size of the symbols is scaled with stellar mass to increase visibility. Stellar masses are computed from all star particles within twice the stellar half mass radius ($2 R_{1/2,\star}$). The *black dashed line* corresponds to an observational fit taken from [Kormendy & Ho \(2013\)](#). For the *bottom panels*, the blue histogram represents BHs that have been always in the quasar feedback mode while the red histogram represents BHs that are or have been in the kinetic feedback mode at some point during their history, even if they are currently in the quasar feedback mode. The *grey shade* corresponds to observational constraints derived by [Shankar \(2009\)](#).

8.5 Black hole spin in cosmological simulations

We compute the fraction of BHs with counter-rotating accretion in the first panel. This is done by counting how many BHs experience counter-rotating accretion in every time bin. At about 20 Myr before coalescence, we find that the fraction monotonically increases until a maximum of 20%, which is reached at about 40 Myr after coalescence. The fraction drops to pre-merger values after 300 Myr. Counter-rotating accretion becomes more likely to occur due to the rapid fluctuations in the central gas angular momentum induced by gas inflows and turbulence during galaxy mergers (Mayer et al., 2007). This situation was already encountered in the individual BH history analysed in Figure 8.5. In the second, third and fourth panels we plot the median trends for the magnitude of the spin parameter, the radiative efficiency and the angle between the gas angular momentum and the BH spin, respectively. There, we also find evidence of a rapid spin misalignment, i.e. the spin parameter drops to a median value of about 0.8, and with it, the radiative efficiency decreases from 20% to about 10%. In some cases, galaxy mergers are also able to trigger the self-gravity regime, which by construction leads to incoherent accretion episodes.

In the last panel, we follow the fractional change of the BH mass accretion rate with respect to the fiducial model, $\Delta \log \dot{M}_{\text{bh}} \equiv \log \dot{M}_{\text{bh}} - \log \dot{M}_{\text{bh, fid}}$. To do so, we match every BH binary with its counterpart in the fiducial simulation; then, we follow the merger in both simulations and compare the mass accretion rate histories centred on the respective coalescence times. For pre-coalescence times, we find that BH accretion in our simulations follows the same trend as in the fiducial model as the median radiative efficiency coincides with the fixed fiducial value ($\epsilon_r = 0.2$). For post-merger times, the drop in radiative efficiency has a twofold effect on BH accretion. On one hand, less radiated energy means more matter is available to the BH. Besides, a temporarily diminished BH feedback aids the global accretion onto the BH-disc system. On the other hand, some BHs are accreting at Eddington rates as we select only those in the quasar feedback mode before coalescence. The inverse proportionality of Eddington rate on radiative efficiency implies that mass accretion in those BHs is capped with a higher value. All this results in enhancements of up to 0.25 dex in BH accretion a few tens of Myr after coalescence with respect to the fiducial case.

We proceed by analysing the alignment of the two BH spins in BH binaries prior to coalescence as a function of binary mass. The results are shown in Figure 8.10. For almost the entire mass range, the spins in BH binaries tend to be slightly aligned as the trend goes towards positive values. The only exception appears in BHs of masses $10^8 - 10^{8.5} M_{\odot}$, in which we find a more isotropic distribution. In this mass range, the self-gravity regime also kicks in, and given that we adopted the chaotic accretion scenario (i.e. $k = 0$), the BH

8. SPIN EVOLUTION OF SUPERMASSIVE BLACK HOLES

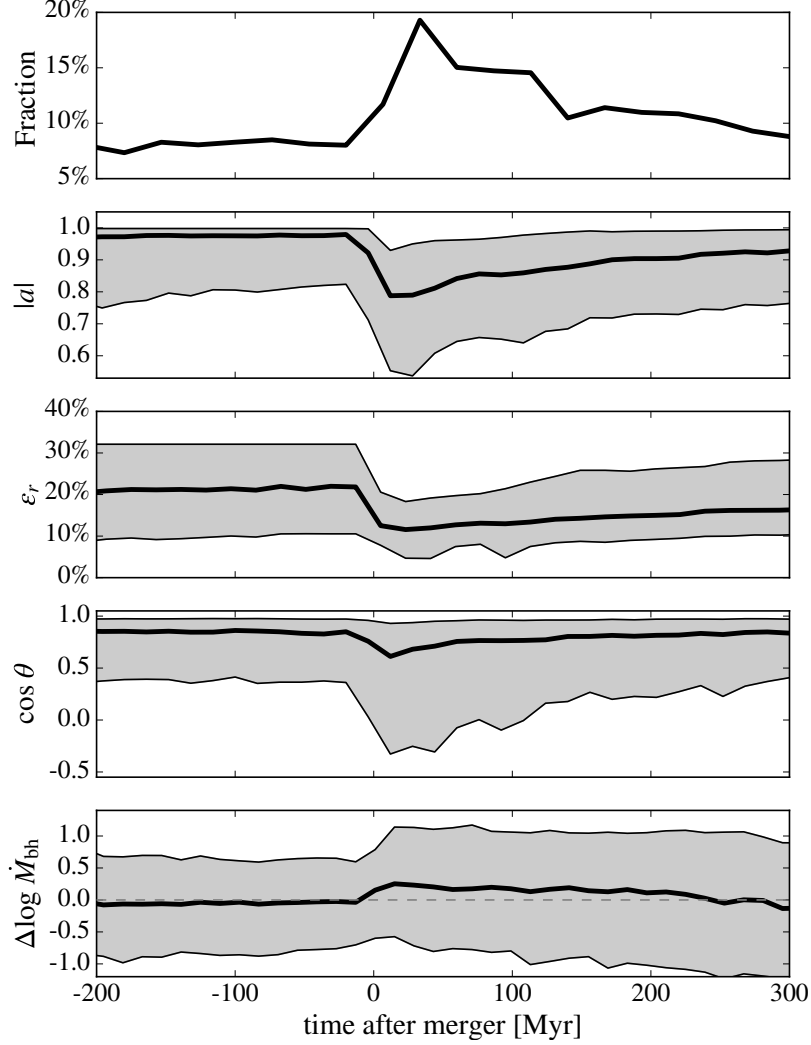


Figure 8.9: Average time evolution of different properties of merging BHs relative to the galaxy coalescence time. Negative time values indicate pre-merger stages, where only the more massive BH in the pair is shown. Also, we restrict our analysis to BHs that are in the coherent accretion regime before the merger. *From top to bottom:* Probability of a counter-rotating accretion episode, stacked median profiles of BH spin, radiative efficiency, angle between BH spin and angular momentum of surrounding gas, and fractional change of the mass accretion rate. For the last property, we normalise each individual profile with the mass accretion rate in the fiducial model 50 Myr before the merger time. The grey regions are enclosed by the 25% – 75% percentiles of the corresponding distributions.

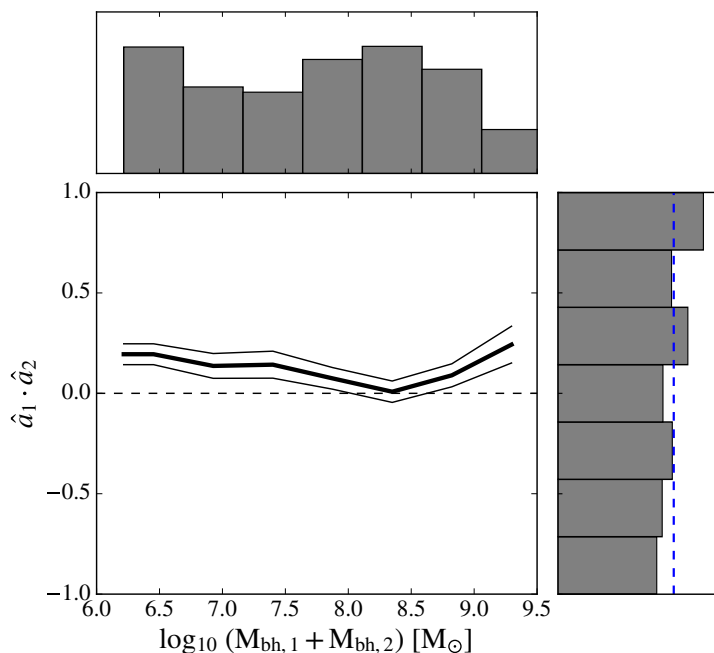


Figure 8.10: *Central panel:* median of the scalar product between the two normalised spin vectors of BH binaries prior to coalescence as a function of their total mass (*solid thick line*) and the standard error of the median (*solid thin lines*). *Top and right panels:* 1D histograms of BH binary masses and spin alignment, respectively. The *blue dashed line* represents an isotropic and uncorrelated distribution of the two spins.

spin orientation is randomised. For less massive BH binaries, their host galaxies are mostly gas rich, and therefore, galaxy mergers are frequently wet. This implies that the two BHs in a binary shared a common gas reservoir before coalescence, and through gas accretion, both spins can be orientated in a similar direction. For more massive binaries, gas accretion is already suppressed and most galaxy mergers are dry. Spin alignment in this case is somewhat unexpected and therefore arguably more interesting. We hypothesise that galaxy alignment with the cosmic web might play a role here. For instance, [Mesa et al. \(2018\)](#) find that the axis connecting SDSS galaxy pairs is aligned with the host cosmic filament, showing thus that the galaxy merger process is not isotropic and depends on environment. The positive spin alignment in BH binaries might then be an imprint of a large-scale galaxy alignment.

Finally, we plot in [Figure 8.11](#) the distribution of gravitational recoil velocities for remnants of coalescing BH binaries as a function of BH mass. We normalise with the local escape velocity of each host galaxy as derived from the central gravitational potential; therefore, individual systems with $v_{\text{recoil}}/v_{\text{esc}} > 1$ are BHs that can potentially escape their host

8. SPIN EVOLUTION OF SUPERMASSIVE BLACK HOLES

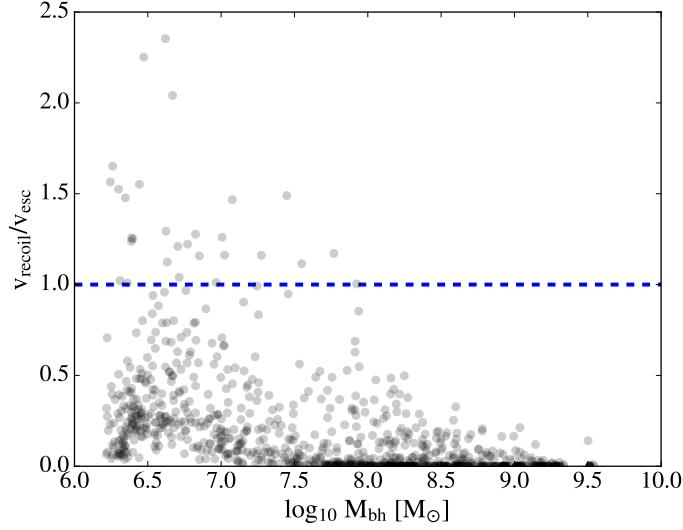


Figure 8.11: Recoil velocities of BH binary remnants normalised by the local escape velocity of the host galaxy as a function of BH mass. The *blue dashed line* represents the threshold above which free floating BHs can potentially form.

and form a population of free floating BHs (Favata et al., 2004; González et al., 2007). This is indeed the case for a few BHs with masses below $10^8 M_{\odot}$. For higher mass BHs, their host galaxies are massive enough to keep them gravitationally bound. The recoil produced by a gravitational wave burst depends on the mass asymmetry of the BH binary and the BH spins (see equation 8.25). The term depending on the mass asymmetry only accounts for a small fraction of the recoil velocity and is not enough to eject the BH remnant. Consequently, the configuration of the spins in a BH binary is what most likely drives the strong recoil that ultimately produces a free floating BH (Campanelli et al., 2007). Milder recoil kicks, which are more ubiquitous in almost the entire mass range, are also extremely important as they yield a population of off-centred BHs, which can impact lifetimes of AGNs, enhance central star formation, ease the formation of massive stellar cusp, and increase the intrinsic scatter of the $M_{\text{bh}} - \sigma_{*}$ relation (Sijacki et al., 2011; Blecha et al., 2011). Unfortunately, we cannot assess these effects self-consistently as BHs are artificially glued to the galaxy potential minima in our numerical model and thus the recoil velocity is not applied. Our result therefore merely demonstrates a capability of our model that has yet to be exploited self-consistently.

As a caveat, we also remind the reader that our treatment of BH coalescence is simplistic and does not account for processes such as dynamical friction, stellar hardening and circum-

binary discs, which can exert an important influence on BH binaries. For example, [Dotti et al. \(2010\)](#) show that large-scale nuclear discs, which are likely to form in gas-rich mergers, can orientate both BH spins perpendicular to the binary orbital plane in a relatively short time scale ($\lesssim 10$ Myr), which ultimately results in weaker gravitational recoil kicks compared to an isotropic spin distribution. The positive alignment of BH binaries in our simulation (Figure 8.10) reinforces this conclusion as it shows that spins are already mildly oriented, even without including a circumnuclear disc. In the light of this discussion, our estimates of the velocity recoil of BH binary remnants in gas rich mergers are likely overestimated, and we consequently interpret them as an upper limit case. A proper treatment in which dynamical friction and other dissipative processes are included along with a self-consistent model of spin evolution is essential to properly address the effects of off-centred and free floating BHs in a cosmological context. We plan to address this in future work.

8.6 Black hole spin and feedback

In this section, we explore the impact of our novel BH feedback switch, which is based on the self-gravity of the accretion disc, on the galaxy population. To this end, we plot in Figure 8.12 the morphology – colour relation (right panels), the colour – stellar mass relation (central panels), and the morphology – size relation (left panels), for the fiducial run (top panels) and for our full model with BH spin evolution and the self-gravity feedback switch (bottom panels). We quantify galaxy morphology with the disc-to-total mass ratio (D/T), which is computed from the total mass of stellar particles within one tenth of the virial radius ($0.1 R_{200,c}$) that have relatively high circularity ($\epsilon > 0.7$) and do not belong to the spheroidal component. For galaxy colour we use the $g - r$ index. Galaxy stellar mass is computed from all star particles within twice the stellar half mass radius ($2 R_{1/2,*}$), as in Figure 8.8. Finally, the stellar half mass radius is used as a proxy of galaxy size.

We recall that a strong galaxy colour bimodality consistent with observations is found in IllustrisTNG ([Nelson et al., 2018](#)). It is thus not surprising that in our fiducial run, which implements the same IllustrisTNG physics model, we also find a strong bimodality with a population transition at stellar masses of about $10^{10} M_{\odot}$. Interestingly, our new feedback switch produces an even stronger colour bimodality with a population transition also at $10^{10} M_{\odot}$. Specifically, our model yields a larger population of red sequence galaxies, but with a somewhat lower stellar mass, i.e. the average stellar mass of galaxies with $g - r > 0.6$ is $10^{10.3} M_{\odot}$ and $10^{10.6} M_{\odot}$ in our model and in the fiducial mode, respectively. Galaxies also

8. SPIN EVOLUTION OF SUPERMASSIVE BLACK HOLES

exhibit smaller sizes in our model.

An analogous result appears for the BH mass – stellar mass relation and the BH mass function in our full model (see right panels of Figure 8.8), in which BHs more massive than $10^8 M_{\odot}$ seem to have a somewhat stagnant growth. The “bottleneck” effect observed in the fiducial model and the model with BH spin and fiducial feedback switch is also present in the full model, and is even stronger. The fact that the BH mass – stellar mass relation is still followed demonstrates that the underlying mechanism responsible for this effect is also keeping host galaxies from growing their stellar content. Looking at the Eddington ratio vs BH mass diagram (Figure 8.4), we can deduce that a BH of mass $10^8 M_{\odot}$ and accretion rate $\dot{M} = 0.1 \dot{M}_{\text{Edd}}$, which is a common scenario at high redshift ($z \sim 2$), would be promptly put into the kinetic feedback mode in our model, whereas it would remain in the quasar mode if the fiducial switch was adopted instead. This means that stellar quenching and suppression of gas accretion by AGN feedback in massive galaxies are maintained for a longer time in our model.

As described in Section 8.4, we adopt the same set of numerical parameters used in IllustrisTNG, which includes the coupling efficiency of the kinetic feedback mode ($\epsilon_{\text{f, kin}} = 0.2$). Because this parameter quantifies how much energy is ultimately delivered to the gas in the form of kinetic energy, its specific value can in principle be set by tuning the simulation to reproduce specific observational trends related to BH-galaxy co-evolution. Given that we inject kinetic feedback energy to the gas at the same rate, but for more prolonged time periods than the fiducial model, we are likely overdoing AGN galaxy quenching in massive galaxies, which results in an atrophied BH and galaxy population. A potential solution to this problem is to scale down the value of $\epsilon_{\text{f, kin}}$ in order to deliver a similar amount of total kinetic energy as in the fiducial model, but in a more steady and prolonged fashion. A second, and perhaps more realistic alternative is to consider a spin dependent kinetic feedback (see equation 8.30). The feedback energy will be initially very powerful as a BH just entering the self-gravity regime should have a high spin value from the coherent regime. Nevertheless, once stochastic accretion in the self-gravity regime sets in, the BH will be rapidly spun down, and thus the feedback energy will diminish in a few hundreds of Myr. In this way, we could potentially produce a more consistent galaxy population at $z = 0$, while at the same time account for high redshift galaxy quenching.

Although no parameter re-calibration was carried out in our simulations for the purpose of this initial study, our results are in remarkably good agreement with the fiducial model. An interesting discrepancy arises in the morphology – colour relation, however. As

discussed in Section 8.3, galaxies in IllustrisTNG exhibit morphologies inconsistent with their colours, i.e. there is an excess of red discs and blue spheroids (Rodríguez-Gomez et al., 2019). This is indeed seen in our fiducial simulation, too, in which bluer galaxies ($g - r < 0.6$) do not exhibit a clear morphological trend, i.e. there is an almost equal fraction of spheroids and disc-like galaxies that are blue. In our model, however, a clearer trend towards disc-like morphologies appears for blue galaxies, which is more consistent with observations. The population of red galaxies is also clearly dominated by spheroids. This result is very interesting because, in spite of the somewhat stronger kinetic feedback in our simulation, our self-gravity feedback switch still manages to select the correct morphological type of galaxies to quench, even if done slightly too strongly.

With the aim of further investigating the previous result, we compute in Figure 8.13 the evolution of the fraction of BHs in the self-gravity regime that have masses between $10^{7.5} M_{\odot}$ and $10^{8.5} M_{\odot}$ and are hosted by merging galaxies. This specific mass range is where most BHs enter the self-gravity regime and, therefore, hosts galaxies which become quenched and red. We notice a significant increase in the BH fraction from 500 Myr before to 500 Myr after the merger time. This demonstrates that galaxy mergers speed up the onset of the self-gravity regime, because a boosted BH growth, either through gas accretion or BH coalescence or both, facilitates the transition from the coherent regime (see Figure 8.4). For our model, this has the consequence that the kinetic feedback mode is activated predominantly in merging galaxies, in which major morphological changes take place as well. This explains why we recover the galaxy morphology – colour relation in our simulations, while still reproducing the colour bimodality and the BH mass – stellar mass relation.

8.7 Summary and Conclusions

We have implemented a new sub-grid model for BH spin evolution in the N -body magnetohydrodynamical moving-mesh code AREPO. We account for two different channels of spin evolution, namely gas accretion and BH binary coalescence. Additionally, we test a hypothesis in which the self-gravity of the BH accretion disc regulates the transition from a quasar BH feedback mode to a kinetic BH feedback mode. We have run several cosmological simulations to explore the new models, including a fiducial run with the original IllustrisTNG physics that is used as a comparison reference. Our main findings can be summarized as follows:

- Gas accretion in low and intermediate mass BHs ($M_{\text{bh}} \lesssim 10^8 M_{\odot}$) occurs in a coherent

8. SPIN EVOLUTION OF SUPERMASSIVE BLACK HOLES

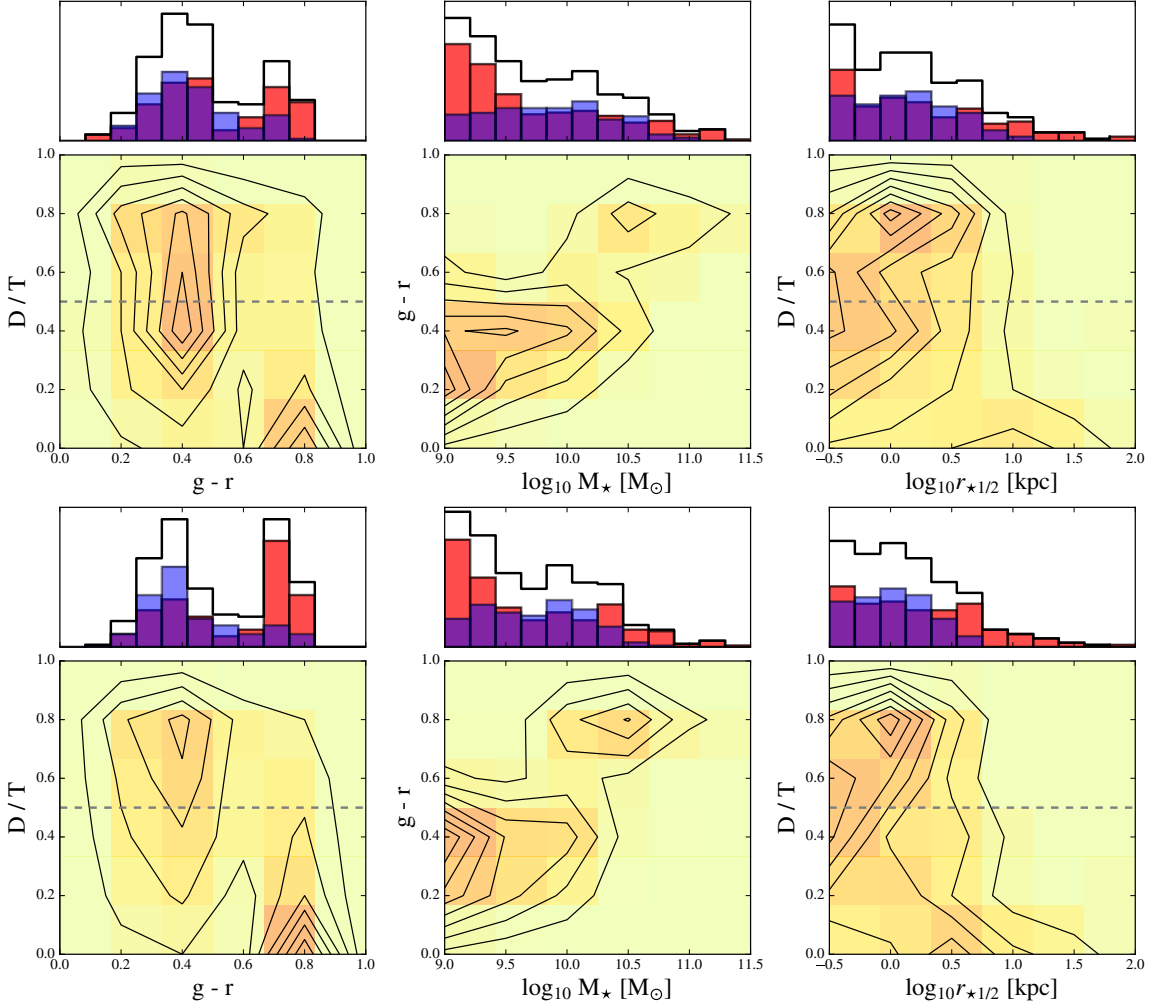


Figure 8.12: Morphology – colour (*right panels*), colour – stellar mass (*central panels*) and morphology – size (*left panels*) relations at $z = 0$ for the fiducial model (*top panels*) and our full model assuming chaotic accretion in the self-gravity regime (*bottom panels*). For each property, we take 6 bins in the shown ranges which are used to compute the 2D histograms and the contours. In the top 1D histograms of each panel, the blue histograms correspond to galaxies with $D/T \geq 0.5$, which we vaguely associate with early-type morphologies. The red histograms correspond to galaxies with $D/T < 0.5$, which exhibit late-type morphologies.

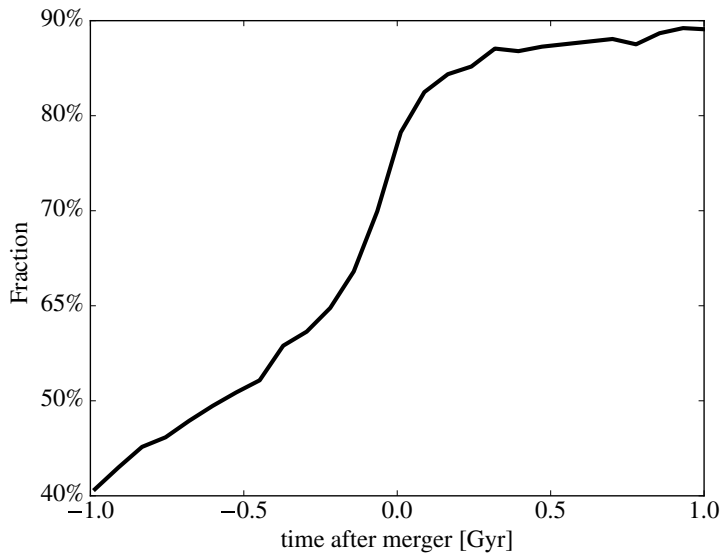


Figure 8.13: Fraction of BHs of masses $10^{7.5} - 10^{8.5} M_{\odot}$ hosted by merging galaxies that are in the self-gravity regime as a function of time. Negative time values indicate pre-merger stages, where the merger time is defined as the coalescence of the two involved central BHs. Note that only mergers of galaxies massive enough to host BHs in the selected mass range are considered.

fashion as small-scale turbulence induced by a self-gravitating disc is negligible. For higher redshift ($z \gtrsim 2$), the angular momentum of the central gas reservoir around the BH can fluctuate considerably. However, low-mass BHs can be easily reoriented, and thus, although the BH spin direction can fluctuate, the net effect is an increase of the spin magnitude. An exception occurs in galaxy mergers, in which strong gas inflows can cause rapid fluctuations in the gas angular momentum that cannot be followed up by the BH, even if it is accreting already at its Eddington rate. This results in a decrease of both the spin parameter and the radiative efficiency, because counter-rotating accretion becomes more likely. A consequence of this is a boost in BH growth of up to 0.25 dex during the merger phase. A few hundreds of Myr after the merger, accretion becomes coherent again, and the BH is quickly spun up. In some intermediate mass BHs, a galaxy merger can trigger the self-gravity regime due to the boosted BH growth.

- More massive BHs ($M_{\text{bh}} \gtrsim 10^8 M_{\odot}$) can develop massive accretion discs in which self-gravity effects become important and counter-rotating accretion occurs frequently. This leads to a drop of the BH spin magnitude that depends on the degree of aniso-

8. SPIN EVOLUTION OF SUPERMASSIVE BLACK HOLES

tropy of the incoming directions of accretion episodes that replenish the inner disc. Nevertheless, these BHs usually reside in massive, early-type galaxies in which star formation activity must be promptly quenched. Therefore, most of them are in the kinetic BH feedback mode, and thus, gas accretion is drastically suppressed. This implies that spin evolution is mainly driven by BH binary coalescence, while gas accretion in the self-gravity regime plays only a weak role in shaping the BH spin evolution. Our predicted BH spin distribution is in very good agreement with the observational data compiled by [Reynolds \(2013\)](#), and with previous studies of BH spin evolution in a cosmological context (e.g. [Dotti et al., 2013](#); [Dubois et al., 2014](#)).

- Due to the non-linear dependence of the radiative efficiency on the BH spin, even short periods of incoherent accretion can significantly impact BH growth. This is seen in the larger scatter of the BH mass – stellar mass relation in our simulation compared to the fiducial TNG model, in which a calibrated fixed value for the radiative efficiency is adopted. The fact that our relation still follows the same trend as the fiducial model, and is consistent with the observational fit of [Kormendy & Ho \(2013\)](#), reveals however that self-regulated gas accretion still operates in a broadly similar fashion if BH spin evolution is accounted for.
- The spins of BH binaries are mildly aligned prior to coalescence, with the only exception occurring in BH binaries of masses $10^8 M_{\odot}$ to $10^{8.5} M_{\odot}$, which exhibit a more isotropic distribution due to incoherent accretion induced by the disc self-gravity. For low-mass BH binaries, their coalescence occurs usually in gas-rich environments, in which a common gas reservoir can orient, through gas accretion, both spins in a similar direction. Further alignment can be reached by the action of a circumnuclear disc ([Dotti et al., 2010](#)). For more massive BHs, gas accretion is already suppressed by the strong BH feedback. Therefore, spin alignment in this case might presumably reflect a large-scale alignment of galaxies with their environment. An alignment of BH spins can weaken gravitational wave bursts from BH binary coalescence and the subsequent recoil kick of the BH remnant, and has thus potentially direct consequences for the population of off-centred and free floating BHs, as well as for the predicted gravitational wave background.
- We propose a novel scheme for activating the kinetic BH feedback mode that is based on the self-gravity of the accretion disc. In this scenario, massive accretion discs, in

which self-gravity becomes significant, get fragmented outside their self-gravity radius R_{sf} . As the disc gets more massive, the self-gravity radius shrinks, and so does the radiatively efficient innermost disc. This leads to a natural shut down of the quasar feedback mode. On the other hand, incoherent accretion induced by disc fragmentation provides favourable conditions for a spherical hot accretion flow. Furthermore, counter-rotating accretion becomes more frequent, in which case the production of non-thermal jet outflows is highly efficient (Garofalo et al., 2010). Our conjecture is therefore to activate the kinetic feedback mode once $R_{\text{sg}} \leq R_{\text{warp}}$. We compare with the warp radius R_{warp} as only the material inside the warped disc can effectively transfer angular momentum to the BH (Volonteri et al., 2007), i.e. self-gravity does not significantly impact mass and angular momentum accretion if $R_{\text{sg}} > R_{\text{warp}}$. For a highly spinning BH ($a = 0.998$), the feedback transition occurs at a BH mass of about $10^8 M_{\odot}$, which, according to the BH mass – stellar mass relation (Kormendy & Ho, 2013), corresponds to a host galaxy of stellar mass $\sim 10^{10} M_{\odot}$. This stellar mass coincides surprisingly well with the mass scale at which galaxies enter the red sequence (Peng et al., 2010), thereby making our proposed scenario a plausible explanation for the onset of star formation quenching in massive galaxies.

- In order to test our new feedback switch, we analyse different properties of the galaxy population and compare them with the fiducial TNG model. We find a bimodality in the galaxy colour relation that is consistent with the fiducial model, although being somewhat more pronounced. Our high mass galaxies are in general less massive and have smaller sizes, which indicates a stronger kinetic feedback in our simulations. Our proposed feedback switch activates the kinetic feedback mode in massive BHs earlier than in the fiducial model. Considering that we adopted the same set of parameters as in IllustrisTNG, including the coupling efficiency of the kinetic feedback mode $\epsilon_{\text{f, kin}}$, we are consequently delivering more kinetic energy to the central gas. A possible solution to this problem would be to scale down the efficiency, either by simply adopting a lower value, or by implementing a spin-dependent kinetic feedback (e.g. equation 8.30), in such a way that the kinetic feedback energy is injected to the gas in a more prolonged fashion.
- Rodriguez-Gomez et al. (2019) reported a tension between IllustrisTNG and observations with respect to the galaxy morphology – colour relation, with red discs and blue spheroids appearing to be in excess in the simulations. As expected, our fidu-

8. SPIN EVOLUTION OF SUPERMASSIVE BLACK HOLES

cial run displays a similar trend, as it is based on the original IllustrisTNG physics model. When we use our new model with BH spin evolution and the kinetic feedback switch, galaxies exhibit morphologies more consistent with their colours, i.e. blue galaxies are predominantly disc types, while red galaxies are mostly spheroids. We find that galaxy mergers are efficient triggers of self-gravity in the accretion discs as a boosted BH growth facilitates the transition from the coherent accretion regime (see Figure 8.4). Considering that we activate the kinetic feedback mode at the onset of the self-gravity regime, and that merging galaxies undergo significant morphological changes, this explains why our approach succeeds in recovering the missing relation between morphology and colour.

Our implementation of a self-consistent BH spin evolution model into realistic hydrodynamical cosmological simulations is an important advance with respect to the first generation of BH models in which BHs were simply treated as massive sink particles, ignoring the spin. Our results demonstrate the importance of coupling the spin to the physics of BH accretion and feedback, especially during galaxy mergers. The potential role of the BH spin, through the self-gravity of the accretion disc, in shaping the galaxy colour bimodality and a correct morphology – colour relation is a further tantalising finding, suggesting that future simulation campaigns should include refined models of BH spin evolution in order to yield more realistic results.

Part IV

Conclusions and outlook

Gas metallicity and star formation in galaxy mergers

The metal content of the interstellar medium is regulated by several competing processes. On the one hand, the process of star formation produces heavy elements, thereby increasing the metal budget of the ISM. On the other hand, accretion of pristine gas from extragalactic reservoirs can dilute the gas metallicity, and at the same time boost star formation, especially at the galactic centre. Additionally, metal enriched gas cools down and collapses faster than pristine gas, and thus, it is locked up in the stellar phase, resulting in a reduction of the gas metallicity. Finally, gas outflows driven by stellar processes such as supernovae and winds from AGB stars expel and redistribute metals in galaxies. In isolated, quiescently star forming galaxies, these processes lead to a self-regulated steady cycle of metal enrichment as the galaxy stellar mass is assembled. This is evinced by tight observational relations such as the mass-metallicity relation ([Lequeux et al., 1979](#); [Tremonti et al., 2004](#)) and the fundamental metallicity relation (FMR; [Ellison et al., 2008a](#); [Mannucci et al., 2010](#)), in which a secondary dependence on the star formation rate (SFR) is included. In contrast, the evolution of the gas metallicity in merging galaxies is still an open question, partly due to the violent nature of these events. Recent observational studies suggest that these galaxies might constitute a population of outliers in the FMR ([Grønnow et al., 2015](#)).

In chapter 6, we use for the first time high-resolution zoom-in simulations of Milky-Way like galaxies in a fully cosmological context to study the problem of star formation enhance-

9. GAS METALLICITY AND STAR FORMATION IN GALAXY MERGERS

ment and metallicity dilution in merging galaxies. Unlike idealised simulations of merging galaxies, in which the orbital parameters and the initial metallicity profiles of the galaxy pairs are set *a priori*, our galaxy pairs are self-consistently evolved within a cosmological setup. We find that periods of very high star formation activity ($\Delta \log \text{SFR} \sim 1 \text{ dex}$) and metallicity dilution ($\Delta \log Z_{\text{SFR}} \sim -0.2 \text{ dex}$) triggered by strong gas inflows take place at the galactic centre of the main galaxy in major mergers. Minor mergers exhibit weaker but still visible SFR enhancements and metallicity dilutions. In some cases, the presence of a second galaxy companion further enhances the strength of the SFR enhancement, demonstrating thus the importance of including realistic environments. The consumption timescale of the star-forming gas is shown to correlate with the stellar mass ratio of mergers, with major mergers displaying the shortest times and thus, the most bursty star formation.

In order to facilitate a direct comparison with observations, we compute the SFR enhancement and metallicity dilution as a function of the projected separation of galaxy pairs. The magnitudes of these processes are found to decrease as a function of the projected separation, and become negligible at separations of $r_p > 100h^{-1} \text{ Mpc}$, which is in good agreement with the observational results of [Scudder et al. \(2012\)](#). Finally, a second-order polynomial in stellar mass, metallicity and SFR that represents the FMR is fitted to our sample of simulated galaxies. We find that ongoing mergers and post-merger galaxies are well differentiated outliers in the relation, with much lower metallicity values than predicted. This suggests that the metal enrichment of the ISM works very differently in mergers and that the FMR only describes the evolution of isolated and quiescent star-forming galaxies.

In chapter 7, we follow a similar procedure on observed galaxy pairs and post-merger galaxies of the SDSS, i.e. we fit a FMR to the data and compare the residual metallicity distributions of isolated galaxies and galaxy pairs. This comparison reveals that galaxy pairs and post-merger galaxies constitute an outlier population in the relation, thereby confirming our theoretical predictions. Additionally, the environment of galaxy pairs is characterised through two parameters, the number of neighbours within $2h^{-1} \text{ Mpc}$ (N_2), and the distance to the second closest companion (r_2). We find that only the presence of a second companion has a considerable impact on the SFR enhancement, while the metallicity dilution appears to be unaffected by environmental effects other than the merger.

A better understanding of the relative importance and the interplay between the processes involved in the evolution of gas metallicity in merging galaxies can be achieved through the use of tracer particles in simulations. This would allow us to trace the exact origin of metals and the accreted pristine gas that ultimately dilutes the central metallicity.

CHAPTER
10

Spin evolution of supermassive black holes

Supermassive black holes are a key ingredient of modern theories of galaxy formation (Kauffmann & Haehnelt, 2000). Apart from being present in virtually all galaxies in the Universe, BHs can drive important transformations in the properties of host galaxies due to the extremely efficient mechanisms of mass-energy conversion that operate in the accretion discs around them. They are completely characterised by two physical parameters, namely their mass and spin (Heusler, 1996). Nonetheless, most modern simulations of galaxy formation treat black holes simply as massive sink particles, ignoring the spin.

In chapter 8, we implement a sub-grid model for BH spin evolution in the code AREPO. Two different channels of spin evolution are considered, gas accretion and BH binary coalescence. Using this model, we find that gas accretion in black holes with masses $M_{\text{bh}} \lesssim 10^8 M_{\odot}$ occurs in a coherent fashion as small-scale turbulence induced by a self-gravitating disc is negligible, resulting thus in highly spinning BHs. In more massive BHs of masses $M_{\text{bh}} \gtrsim 10^8 M_{\odot}$, the accretion discs grow significantly, and as a consequence, self-gravity effects become important and counter-rotating accretion occurs frequently, thereby leading to a drop of the BH spin magnitude. However, BHs in this mass range usually reside in massive, early-type galaxies in which gas accretion is drastically suppressed. In that regime, the spin evolution is mainly driven by BH binary coalescence. Overall, our predicted BH

10. SPIN EVOLUTION OF SUPERMASSIVE BLACK HOLES

spin distribution is in very good agreement with the observational data compiled by Reynolds (2013), and with previous studies of BH spin evolution in a cosmological context (see e.g. Dotti et al., 2013; Dubois et al., 2014).

An interesting application of our BH spin evolution model is related to BH feedback. The use of a two-mode BH feedback prescription has been shown to be crucial to reproduce a bimodal galaxy colour distribution in simulations that is consistent with galaxy surveys (Weinberger et al., 2017). The two modes are a quasar mode in which thermal energy is injected in the surrounding gas of rapidly accreting BHs, and an efficient mode of kinetic energy injection in phases of low gas accretion. The activation of the kinetic BH feedback mode is set to occur approximately at stellar masses of $10^{10.5} M_{\odot}$. Above this stellar mass, the BH feedback energy is able to quench the star formation activity in host galaxies, allowing them to reproduce the red galaxy sequence. Nevertheless, the exact physical conditions under which this transition occurs are still widely debated. We test a new hypothesis in which the activation of the kinetic mode is determined by the onset of self-gravity fragmentation in accretion discs. In this scenario, massive self-gravitating accretion discs are disrupted outside their self-gravity radius R_{sf} . As the disc gets more massive, the self-gravity radius shrinks, and so does the radiatively efficient innermost disc. This leads to a natural shut down of the quasar feedback mode. At the same time, incoherent accretion induced by disc fragmentation provides favourable conditions for a spherical hot accretion flow and the efficient production of non-thermal jet outflows (Garofalo et al., 2010). With this new approach, we find that the kinetic feedback mode is activated in highly spinning BHs ($a = 0.998$) once they reach a mass of about $10^8 M_{\odot}$, which, according to the BH mass – stellar mass relation (Kormendy & Ho, 2013), corresponds to a host stellar mass of about $10^{10-10.5} M_{\odot}$. Considering that the implemented kinetic mode does not have any explicit dependence on BH spin, a feedback transition occurring at this specific stellar mass guarantees the creation of a galaxy colour bimodality like IllustrisTNG does.

A tension in the galaxy morphology – colour relation between IllustrisTNG and observations has been recently reported in Rodriguez-Gomez et al. (2019). Specifically, red discs and blue spheroids appear to be over-abundant in the simulation. With our model, this tension seems to be alleviated, i.e. blue galaxies are predominantly disc types, while red galaxies are mostly spheroids. A plausible explanation is that the boosted BH growth during a galaxy merger facilitates the transition from a coherent to a chaotic accretion regime. As a result, the kinetic feedback mode is activated and star formation is subsequently quenched. In addition to this, major morphological changes in galaxies are known to be driven by

merger events. Hence, a relation between galaxy morphology and colour is expected.

With the advent of the gravitational wave era by the discovery of gravitational waves from stellar-mass BHs ([Abbott et al., 2016](#)) and the ever-improving observational techniques to measure supermassive BHs (see e.g. the first image of a supermassive BH taken by the Event Horizon Telescope; [Event Horizon Telescope Collaboration et al., 2019](#)), the interest in the merger process of supermassive BHs and the role of BH spin has drastically increased. During the final inspiral phase of two coalescing BHs, the relative configuration of the spins has important effects on the final gravitational wave burst and the recoil of the BH remnant (see e.g. [Rezzolla et al., 2008](#)). Therefore, the use of a BH spin evolution model in a cosmological context is key to predict the gravitational wave background from coalescing supermassive BHs.

A second key process that needs to be modelled in cosmological simulations is the dynamical friction that stars and gas exert on central super massive BHs ([Just et al., 2011](#)). This determines the formation timescale of BH binaries after galaxy mergers, and the return timescale of off-centred BHs. In spite of its importance, this aspect has been neglected in the simulations used in this thesis in order to avoid spurious orbital heating effects originating from the coarse mass resolution of the stellar and gas components. Different approaches to solve BH dynamical friction have been implemented in previous simulations. For instance, [Dubois et al. \(2013\)](#) employ an effective drag force to model gas dynamical friction. [Tremmel et al. \(2015\)](#) estimate the stellar dynamical friction from the Chandrasekhar's formula ([Chandrasekhar, 1943](#)) and the local velocity distribution of stellar particles. [Khan et al. \(2012\)](#) use a re-simulation technique on hydrodynamical simulations of merging galaxies to study the hardening process of BH binaries with N-body methods. Future work will include realistic prescriptions of stellar and gas dynamical friction couple to the current BH spin evolution model. This will allow us to investigate the role of BH spin in off-centred and free floating BHs that are the result of coalescing BH binaries, as well as to predict the gravitational wave background from these events.

List of publications

First author

- * **S. Bustamante**, S. Ellison, M. Sparre, D.R. Patton., Galaxy pairs in the Sloan Digital Sky Survey – XIV. Galaxy mergers do not lie on the Fundamental Metallicity Relation, *In preparation*
- * **S. Bustamante**, V. Springel., Spin evolution and feedback of supermassive black holes in a cosmological context, 2019, *Submitted to MNRAS*
- * **S. Bustamante**, M. Sparre, V. Springel, R.J.J Grand., Merger-induced metallicity dilution in cosmological galaxy formation simulations, 2018, [MNRAS 479 3381](#)
- **S. Bustamante**, J.E. Forero-Romero., Tensor anisotropy as a tracer of cosmic voids, 2015, [MNRAS 453 1 497](#)

* part of this thesis.

Coauthor

- R.J.J. Grand, **S. Bustamante**, F.A. Gómez, D. Kawata, F. Marinacci, R. Pakmor, H-W. Rix., C.M. Simpson, M. Sparre, V. Springel., Origin of chemically distinct discs in the Auriga cosmological simulations, 2018, [MNRAS 474 3629](#)
- A. Monachesi, F.A. Gómez, R.J.J. Grand, C.M. Simpson, G. Kauffmann, **S. Bustamante**, F. Marinacci, R. Pakmor, V. Springel, C.S. Frenk, S.D.M. White, P. Tissera., The Auriga Stellar Haloes: Connecting stellar population properties with accretion and merging history, 2018, [MNRAS 485 2589](#)

List of publications

- J.I. Zuluaga, **S. Bustamante**, Geomagnetic properties of Proxima Centauri b analogues, 2018, *P&SS* [152 55](#)
- F.A. Gómez, R.J.J. Grand, A. Monachesi, S.D.M. White, **S. Bustamante**, F. Marinacci, R. Pakmor, C.M. Simpson, V. Springel, D.J.R. Campbell, C.S. Frenk, A. Jenkins., Lessons from the Auriga discs: the hunt for the Milky Way's ex situ disc is not yet over, 2017, *MNRAS* [472 3 3772](#)
- J.I. Zuluaga, **S. Bustamante**, P.A Cuartas, J.H. Hoyos., The influence of thermal evolution in the magnetic protection of terrestrial planets, 2013, *ApJ* [770 23](#)
- J.E. Forero-Romero, Y. Hoffman, **S. Bustamante**, S. Gottloeber, G. Yepes., The kinematics of the Local Group in a cosmological context, 2013, *ApJL* [767 L5](#)

Bibliography

- Abazajian K. N., et al. 2009, ApJS, 182, 543 [73](#)
- Abbott B. P., et al., 2016, Phys. Rev. Lett., 116, 061102 [30](#), [96](#), [147](#)
- Albrecht A., Steinhardt P. J., 1982, Physical Review Letters, 48, 1220 [3](#)
- Bañados E., et al., 2016, The Astrophysical Journal Supplement Series, 227, 11 [4](#), [27](#), [29](#)
- Balbus S. A., Hawley J. F., 1991, ApJ, 376, 214 [31](#), [32](#)
- Baldry I. K., Balogh M. L., Bower R. G., Glazebrook K., Nichol R. C., Bamford S. P., Budavari T., 2006, MNRAS, 373, 469 [127](#)
- Baldry I. K., Glazebrook K., Brinkmann J., Ivezić Ž., Lupton R. H., Nichol R. C., Szalay A. S., 2004, ApJ, 600, 681 [20](#), [21](#)
- Bardeen J. M., 1970, Nature, 226, 64 [99](#)
- Bardeen J. M., Press W. H., Teukolsky S. A., 1972, ApJ, 178, 347 [99](#)
- Barnes J., Hut P., 1986, Nature, 324, 446 [37](#), [117](#)
- Barnes J. E., 2004, MNRAS, 350, 798 [57](#)
- Begelman M. C., 2014, arXiv e-prints, p. arXiv:1410.8132 [111](#), [114](#)
- Bell E. F., Wolf C., Meisenheimer K., Rix H.-W., Borch A., Dye S., Kleinheinrich M., Wisotzki L., McIntosh D. H., 2004, ApJ, 608, 752 [21](#)
- Belli S., Jones T., Ellis R. S., Richard J., 2013, ApJ, 772, 141 [48](#), [72](#)

BIBLIOGRAPHY

- Bellovary J., Volonteri M., Governato F., Shen S., Quinn T., Wadsley J., 2011, *ApJ*, 742, 13
[111](#)
- Berger M. J., Colella P., 1989, *Journal of Computational Physics*, 82, 64 [38](#)
- Black J. H., 1981, *MNRAS*, 197, 553 [24](#)
- Blandford R. D., Znajek R. L., 1977, *MNRAS*, 179, 433 [97](#), [112](#)
- Blecha L., Cox T. J., Loeb A., Hernquist L., 2011, *MNRAS*, 412, 2154 [110](#), [132](#)
- Blumenthal G. R., Faber S. M., Primack J. R., Rees M. J., 1984, *Nature*, 311, 517 [4](#), [5](#)
- Bondi H., 1952, *MNRAS*, 112, 195 [30](#), [109](#)
- Bondi H., Hoyle F., 1944, *MNRAS*, 104, 273 [30](#), [109](#)
- Brandt W. N., Hasinger G., 2005, *Annual Review of Astronomy and Astrophysics*, 43, 827
[33](#)
- Brinchmann J., Charlot S., White S. D. M., Tremonti C., Kauffmann G., Heckman T., Brinkmann J., 2004, *MNRAS*, 351, 1151 [74](#)
- Brown J. S., Martini P., Andrews B. H., 2016, *MNRAS*, 458, 1529 [48](#), [72](#)
- Bustamante S., Sparre M., Springel V., Grand R. J. J., 2018, *MNRAS*, 479, 3381 [5](#), [72](#)
- Butcher H. R., Oemler Jr. A., 1984, *Nature*, 310, 31 [5](#)
- Campanelli M., Lousto C., Zlochower Y., Merritt D., 2007, *ApJ*, 659, L5 [97](#), [108](#), [132](#)
- Carroll B. W., Ostlie D. A., 2006, *An introduction to modern astrophysics and cosmology*
[7](#), [8](#)
- Cen R., 1992, *ApJS*, 78, 341 [24](#), [41](#)
- Chabrier G., 2003, *PASP*, 115, 763 [43](#), [51](#)
- Chandrasekhar S., 1943, *Reviews of Modern Physics*, 15, 1 [147](#)
- Chandrasekhar S., 1983, *The mathematical theory of black holes* [28](#)

BIBLIOGRAPHY

- Christensen L., Richard J., Hjorth J., Milvang-Jensen B., Laursen P., Limousin M., Dessauges-Zavadsky M., Grillo C., Ebeling H., 2012, MNRAS, 427, 1953 [48](#)
- Cortijo-Ferrero C., González Delgado R. M., Pérez E., Cid Fernandes R., Sánchez S. F., de Amorim A. L., Di Matteo P., García-Benito R., Lacerda E. A. D., López Fernández R., Tadhunter C., 2017, MNRAS, 467, 3898 [48](#), [72](#), [91](#)
- Cox T. J., Jonsson P., Somerville R. S., Primack J. R., Dekel A., 2008, MNRAS, 384, 386 [59](#), [68](#)
- Croton D. J., Springel V., White S. D. M., De Lucia G., Frenk C. S., Gao L., Jenkins A., Kauffmann G., Navarro J. F., Yoshida N., 2006, MNRAS, 365, 11 [96](#)
- Daddi E., Dickinson M., Morrison G., Chary R., Cimatti A., Elbaz D., Frayer D., Renzini A., Pope A., Alexander D. M., Bauer F. E., Giavalisco M., Huynh M., Kurk J., Mignoli M., 2007, ApJ, 670, 156 [22](#)
- Daddi E., Elbaz D., Walter F., Bournaud F., Salmi F., Carilli C., Dannerbauer H., Dickinson M., Monaco P., Riechers D., 2010, ApJ, 714, L118 [56](#)
- Darg D. W., Kaviraj S., Lintott C. J., Schawinski K., Sarzi M., Bamford S., Silk J., Andreescu D., Murray P., Nichol R. C., Raddick M. J., Slosar A., Szalay A. S., Thomas D., Vandenberg J., 2010, MNRAS, 401, 1552 [75](#)
- Davé R., Rafieferantsoa M. H., Thompson R. J., Hopkins P. F., 2017, MNRAS, 467, 115 [48](#), [69](#), [72](#)
- Davis M., Efstathiou G., Frenk C. S., White S. D. M., 1985, ApJ, 292, 371 [4](#), [5](#)
- Dawson J. M., 1983, Rev. Mod. Phys., 55, 403 [37](#)
- Dayal P., Ferrara A., Dunlop J. S., 2013, MNRAS, 430, 2891 [48](#), [72](#)
- De Rossi M. E., Bower R. G., Font A. S., Schaye J., Theuns T., 2017, MNRAS, 472, 3354 [48](#), [69](#), [72](#)
- Dekel A., Birnboim Y., 2006, MNRAS, 368, 2 [18](#), [21](#)
- Devecchi B., Volonteri M., 2009, ApJ, 694, 302 [30](#)

BIBLIOGRAPHY

- Di Matteo P., Bournaud F., Martig M., Combes F., Melchior A.-L., Semelin B., 2008, *A&A*, 492, 31 [57](#)
- Di Matteo T., Springel V., Hernquist L., 2005, *Nature*, 433, 604 [34](#), [96](#)
- Dicke R. H., Peebles P. J. E., Roll P. G., Wilkinson D. T., 1965, *ApJ*, 142, 414 [3](#)
- Dotti M., Colpi M., Pallini S., Perego A., Volonteri M., 2013, *ApJ*, 762, 68 [105](#), [125](#), [138](#), [146](#)
- Dotti M., Volonteri M., Perego A., Colpi M., Ruzszkowski M., Haardt F., 2010, *MNRAS*, 402, 682 [133](#), [138](#)
- Dressler A., Oemler Jr. A., Couch W. J., Smail I., Ellis R. S., Barger A., Butcher H., Poggianti B. M., Sharples R. M., 1997, *ApJ*, 490, 577 [5](#)
- Dubois Y., Gavazzi R., Peirani S., Silk J., 2013, *MNRAS*, 433, 3297 [147](#)
- Dubois Y., Volonteri M., Silk J., 2014, *MNRAS*, 440, 1590 [97](#), [125](#), [138](#), [146](#)
- Dubois Y., Volonteri M., Silk J., Devriendt J., Slyz A., 2014, *MNRAS*, 440, 2333 [105](#), [122](#)
- Einstein A., 1916, *Annalen der Physik*, 49, 769 [7](#)
- Eisenstein D. J., Hu W., 1998, *ApJ*, 496, 605 [119](#)
- Elbaz D., Daddi E., Le Borgne D., Dickinson M., Alexander D. M., Chary R. R., Starck J. L., Brandt W. N., Kitzbichler M., MacDonald E., Nonino M., Popesso P., Stern D., Vanzella E., 2007, *A&A*, 468, 33 [22](#)
- Ellison S. L., Mendel J. T., Patton D. R., Scudder J. M., 2013, *MNRAS*, 435, 3627 [73](#), [75](#)
- Ellison S. L., Nair P., Patton D. R., Scudder J. M., Mendel J. T., Simard L., 2011, *MNRAS*, 416, 2182 [72](#)
- Ellison S. L., Patton D. R., Simard L., McConnachie A. W., 2008a, *ApJ*, 672, L107 [26](#), [48](#), [72](#), [76](#), [143](#)
- Ellison S. L., Patton D. R., Simard L., McConnachie A. W., 2008b, *AJ*, 135, 1877 [5](#), [48](#), [72](#), [75](#), [91](#)

BIBLIOGRAPHY

- Ellison S. L., Patton D. R., Simard L., McConnachie A. W., Baldry I. K., Mendel J. T., 2010, *MNRAS*, 407, 1514 [87](#)
- Event Horizon Telescope Collaboration Akiyama K., Alberdi A., Alef W., Asada K., Azulay R., Baccko A.-K., Ball D., Baloković M., Barrett J., et al. 2019, *ApJ*, 875, L1 [28](#), [147](#)
- Fall S. M., Efstathiou G., 1980, *MNRAS*, 193, 189 [4](#), [5](#), [18](#)
- Fanidakis N., Baugh C. M., Benson A. J., Bower R. G., Cole S., Done C., Frenk C. S., 2011, *MNRAS*, 410, 53 [97](#), [98](#), [105](#)
- Faucher-Giguère C.-A., Lidz A., Zaldarriaga M., Hernquist L., 2009, *ApJ*, 703, 1416 [41](#)
- Favata M., Hughes S. A., Holz D. E., 2004, *ApJ*, 607, L5 [132](#)
- Ferrarese L., Ford H., 2005, *Space Sci. Rev.*, 116, 523 [28](#)
- Ferrarese L., Merritt D., 2000, *The Astrophysical Journal*, 539, L9 [5](#), [34](#), [95](#)
- Fiacconi D., Sijacki D., Pringle J. E., 2018, *MNRAS*, 477, 3807 [97](#)
- Friedmann A., 1922, *Zeitschrift fur Physik*, 10, 377 [10](#)
- Gabor J. M., Capelo P. R., Volonteri M., Bournaud F., Bellovary J., Governato F., Quinn T., 2016, *A&A*, 592, A62 [57](#)
- Garofalo D., Evans D. A., Sambruna R. M., 2010, *MNRAS*, 406, 975 [114](#), [139](#), [146](#)
- Genel S., Vogelsberger M., Nelson D., Sijacki D., Springel V., Hernquist L., 2013, *MNRAS*, 435, 1426 [69](#)
- Genzel R., Eisenhauer F., Gillessen S., 2010, *Reviews of Modern Physics*, 82, 3121 [27](#)
- Glover S. C. O., Abel T., 2008, *MNRAS*, 388, 1627 [41](#)
- González J. A., Sperhake U., Brüggemann B., Hannam M., Husa S., 2007, *Phys. Rev. Lett.*, 98, 091101 [132](#)
- Grand R. J. J., Gómez F. A., Marinacci F., Pakmor R., Springel V., Campbell D. J. R., Frenk C. S., Jenkins A., White S. D. M., 2017, *MNRAS*, 467, 179 [44](#), [49](#), [50](#), [51](#), [82](#)

BIBLIOGRAPHY

- Grand R. J. J., Springel V., Gómez F. A., Marinacci F., Pakmor R., Campbell D. J. R., Jenkins A., 2016, MNRAS, 459, 199 [51](#)
- Grasshorn Gebhardt H. S., Zeimann G. R., Ciardullo R., Gronwall C., Hagen A., Bridge J. S., Schneider D. P., Trump J. R., 2016, ApJ, 817, 10 [48](#), [72](#)
- Greene J. E., Peng C. Y., Kim M., Kuo C.-Y., Braatz J. A., Impellizzeri C. M. V., Condon J. J., Lo K. Y., Henkel C., Reid M. J., 2010, ApJ, 721, 26 [4](#), [27](#), [28](#), [95](#)
- Grønnow A. E., Finlator K., Christensen L., 2015, MNRAS, 451, 4005 [26](#), [48](#), [64](#), [65](#), [69](#), [72](#), [79](#), [81](#), [143](#)
- Guillet T., Teyssier R., 2011, Journal of Computational Physics, 230, 4756 [37](#)
- Guth A. H., 1981, Phys. Rev. D, 23, 347 [3](#), [14](#)
- Haardt F., Madau P., 2012, ApJ, 746, 125 [41](#)
- Hani M. H., Sparre M., Ellison S. L., Torrey P., Vogelsberger M., 2018, MNRAS, 475, 1160 [72](#), [91](#)
- Häring N., Rix H.-W., 2004, ApJ, 604, L89 [5](#), [34](#), [95](#)
- Hayward C. C., Torrey P., Springel V., Hernquist L., Vogelsberger M., 2014, MNRAS, 442, 1992 [57](#)
- Henriques B. M. B., White S. D. M., Thomas P. A., Angulo R., Guo Q., Lemson G., Springel V., Overzier R., 2015, MNRAS, 451, 2663 [96](#)
- Hernquist L., 1989, Nature, 340, 687 [5](#)
- Heusler M., 1996, Helvetica Physica Acta, 69, 501 [28](#), [145](#)
- Hopkins P. F., Cox T. J., Hernquist L., Narayanan D., Hayward C. C., Murray N., 2013, MNRAS, 430, 1901 [57](#)
- Hopkins P. F., Richards G. T., Hernquist L., 2007, ApJ, 654, 731 [34](#)
- Hoyle F., 1951, in Problems of Cosmical Aerodynamics The Origin of the Rotations of the Galaxies. p. 195 [18](#)

- Hoyle F., Lyttleton R. A., 1939, Proceedings of the Cambridge Philosophical Society, 35, 405 [30](#), [109](#)
- Hubble E., 1929, Proceedings of the National Academy of Science, 15, 168 [11](#)
- Hubble E. P., 1926, ApJ, 64 [19](#)
- Hughes S. A., Blandford R. D., 2003, ApJ, 585, L101 [21](#)
- Ichimaru S., 1977, ApJ, 214, 840 [111](#)
- Jester S., 2005, ApJ, 625, 667 [21](#)
- Just A., Khan F. M., Berczik P., Ernst A., Spurzem R., 2011, MNRAS, 411, 653 [147](#)
- Karakas A. I., 2010, MNRAS, 403, 1413 [44](#), [53](#)
- Karman W., Macciò A. V., Kannan R., Moster B. P., Somerville R. S., 2015, MNRAS, 452, 2984 [57](#)
- Katz N., Weinberg D. H., Hernquist L., 1996, ApJS, 105, 19 [41](#)
- Kauffmann G., et al., 2003, MNRAS, 341, 33 [21](#)
- Kauffmann G., Haehnelt M., 2000, MNRAS, 311, 576 [5](#), [34](#), [95](#), [145](#)
- Kauffmann G., Heckman T. M., Tremonti C., Brinchmann J., Charlot S., White S. D. M., Ridgway S. E., Brinkmann J., Fukugita M., Hall P. B., Ivezić Ž., Richards G. T., Schneider D. P., 2003, MNRAS, 346, 1055 [74](#)
- Kellermann K. I., Sramek R., Schmidt M., Shaffer D. B., Green R., 1989, AJ, 98, 1195 [21](#)
- Kelson D. D., Illingworth G. D., Franx M., van Dokkum P. G., 2001, ApJ, 552, L17 [21](#)
- Kennicutt Jr. R. C., 1998, ARA&A, 36, 189 [21](#), [42](#)
- Kereš D., Katz N., Weinberg D. H., Davé R., 2005, MNRAS, 363, 2 [18](#), [21](#)
- Kerr R. P., 1963, Physical Review Letters, 11, 237 [29](#), [32](#)
- Kewley L. J., Dopita M. A., 2002, ApJS, 142, 35 [74](#), [81](#)
- Kewley L. J., Ellison S. L., 2008, ApJ, 681, 1183 [74](#), [81](#)

BIBLIOGRAPHY

- Kewley L. J., Rupke D., Zahid H. J., Geller M. J., Barton E. J., 2010, *ApJ*, 721, L48 [48](#)
- Khan F. M., Berentzen I., Berczik P., Just A., Mayer L., Nitadori K., Callegari S., 2012, *ApJ*, 756, 30 [147](#)
- King A., 2003, *ApJ*, 596, L27 [34](#)
- King A. R., Lubow S. H., Ogilvie G. I., Pringle J. E., 2005, *MNRAS*, 363, 49 [102](#), [104](#)
- King A. R., Pringle J. E., Hofmann J. A., 2008, *MNRAS*, 385, 1621 [104](#), [105](#)
- Kormendy J., Ho L. C., 2013, *Annual Review of Astronomy and Astrophysics*, 51, 511 [115](#), [126](#), [127](#), [128](#), [138](#), [139](#), [146](#)
- Krumholz M. R., Dekel A., McKee C. F., 2012, *ApJ*, 745, 69 [56](#)
- Lagos C. d. P., Theuns T., Schaye J., Furlong M., Bower R. G., Schaller M., Crain R. A., Trayford J. W., Matthee J., 2016, *MNRAS*, 459, 2632 [48](#), [69](#), [72](#)
- Lara-López M. A., Cepa J., Bongiovanni A., Pérez García A. M., Ederoclite A., Castañeda H., Fernández Lorenzo M., Pović M., Sánchez-Portal M., 2010, *A&A*, 521, L53 [48](#), [72](#)
- Lequeux J., Peimbert M., Rayo J. F., Serrano A., Torres-Peimbert S., 1979, *A&A*, 80, 155 [25](#), [143](#)
- Lilly S. J., Carollo C. M., Pipino A., Renzini A., Peng Y., 2013a, *ApJ*, 772, 119 [22](#)
- Lilly S. J., Carollo C. M., Pipino A., Renzini A., Peng Y., 2013b, *ApJ*, 772, 119 [76](#)
- Linde A. D., 1982, *Physics Letters B*, 116, 335 [3](#), [14](#)
- Longair M., 2008, *Galaxy Formation*, second edn. Springer, New York [7](#), [10](#), [13](#), [14](#)
- Lotz J. M., Jonsson P., Cox T. J., Primack J. R., 2008, *MNRAS*, 391, 1137 [54](#)
- Lynden-Bell D., 1969, *Nature*, 223, 690 [5](#), [19](#), [27](#), [95](#), [99](#)
- Mac Low M.-M., Klessen R. S., 2004, *Reviews of Modern Physics*, 76, 125 [41](#)
- Madau P., Dickinson M., 2014, *Annual Review of Astronomy and Astrophysics*, 52, 415 [22](#)
- Magorrian J., et al., 1998, *AJ*, 115, 2285 [5](#), [34](#), [95](#)

- Maiolino R., et al. 2008, *A&A*, 488, 463 [81](#)
- Mannucci F., Cresci G., Maiolino R., Marconi A., Gnerucci A., 2010, *MNRAS*, 408, 2115
[26](#), [48](#), [63](#), [64](#), [72](#), [79](#), [81](#), [82](#), [143](#)
- Marconi A., Risaliti G., Gilli R., Hunt L. K., Maiolino R., Salvati M., 2004, *MNRAS*, 351,
169 [33](#)
- Marinacci F., Pakmor R., Springel V., 2014, *MNRAS*, 437, 1750 [51](#)
- Marino R. A., et al. 2013, *A&A*, 559, A114 [81](#)
- Martig M., Bournaud F., 2008, *MNRAS*, 385, L38 [57](#)
- Mayer L., Kazantzidis S., Madau P., Colpi M., Quinn T., Wadsley J., 2007, *Science*, 316,
1874 [122](#), [129](#)
- Mazzucchelli C., et al., 2017, *ApJ*, 849, 91 [4](#), [27](#), [29](#)
- McCarthy I. G., Bower R. G., Balogh M. L., 2007, *MNRAS*, 377, 1457 [5](#), [19](#), [34](#), [96](#)
- McKee C. F., Ostriker J. P., 1977, *ApJ*, 218, 148 [42](#)
- Mendel J. T., Simard L., Palmer M., Ellison S. L., Patton D. R., 2014, *ApJS*, 210, 3 [73](#)
- Mesa V., Duplancic F., Alonso S., Muñoz Jofré M. R., Coldwell G., Lambas D. G., 2018,
A&A, 619, A24 [131](#)
- Mihos J. C., Hernquist L., 1996, *ApJ*, 464, 641 [57](#)
- Mitra S., Davé R., Finlator K., 2015, *MNRAS*, 452, 1184 [76](#)
- Mo H., van den Bosch F. C., White S., 2010, *Galaxy Formation and Evolution* [4](#), [7](#)
- Mo H. J., Mao S., White S. D. M., 1998, *MNRAS*, 295, 319 [18](#)
- Monaghan J. J., 1992, *ARA&A*, 30, 543 [38](#)
- Montuori M., Di Matteo P., Lehnert M. D., Combes F., Semelin B., 2010, *A&A*, 518, A56
[68](#)

BIBLIOGRAPHY

- Moreno J., Bluck A. F. L., Ellison S. L., Patton D. R., Torrey P., Moster B. P., 2013, MNRAS, 436, 1765 [76](#), [87](#)
- Moreno J., Torrey P., Ellison S. L., Patton D. R., Bluck A. F. L., Bansal G., Hernquist L., 2015, MNRAS, 448, 1107 [57](#)
- Moster B. P., Macciò A. V., Somerville R. S., Naab T., Cox T. J., 2011, MNRAS, 415, 3750 [49](#)
- Navarro J. F., Frenk C. S., White S. D. M., 1997, ApJ, 490, 493 [18](#)
- Nelson D., Pillepich A., Genel S., Vogelsberger M., Springel V., Torrey P., Rodriguez-Gomez V., Sijacki D., Snyder G. F., Griffen B., Marinacci F., Blecha L., Sales L., Xu D., Hernquist L., 2015, Astronomy and Computing, 13, 12 [113](#)
- Nelson D., Pillepich A., Springel V., Weinberger R., Hernquist L., Pakmor R., Genel S., Torrey P., Vogelsberger M., Kauffmann G., Marinacci F., Naiman J., 2018, MNRAS, 475, 624 [113](#), [133](#)
- Netzer H., 2013, The Physics and Evolution of Active Galactic Nuclei [33](#)
- Noeske K. G., et al. 2007, ApJ, 660, L43 [22](#), [76](#)
- Novikov I. D., Thorne K. S., 1973, in Dewitt C., Dewitt B. S., eds, Black Holes (Les Astres Occlus) Astrophysics of black holes.. pp 343–450 [32](#), [100](#)
- Ogilvie G. I., 1999, MNRAS, 304, 557 [102](#)
- Okamoto T., Frenk C. S., Jenkins A., Theuns T., 2010, MNRAS, 406, 208 [43](#)
- Padmanabhan T., 1995, Structure Formation in the Universe, first edn. Cambridge University Press, Great Britain [7](#), [14](#), [15](#)
- Pakmor R., Springel V., 2013, MNRAS, 432, 176 [38](#)
- Pakmor R., Springel V., Bauer A., Mocz P., Munoz D. J., Ohlmann S. T., Schaal K., Zhu C., 2016, MNRAS, 455, 1134 [49](#)
- Papaloizou J. C. B., Pringle J. E., 1983, MNRAS, 202, 1181 [102](#)

BIBLIOGRAPHY

- Park C., Choi Y.-Y., Vogele M. S., Gott III J. R., Blanton M. R., SDSS Collaboration 2007, *ApJ*, 658, 898 [76](#), [87](#)
- Patton D. R., Carlberg R. G., Marzke R. O., Pritchett C. J., da Costa L. N., Pellegrini P. S., 2000, *ApJ*, 536, 153 [75](#)
- Patton D. R., Pritchett C. J., Carlberg R. G., Marzke R. O., Yee H. K. C., Hall P. B., Lin H., Morris S. L., Sawicki M., Shepherd C. W., Wirth G. D., 2002, *ApJ*, 565, 208 [75](#)
- Patton D. R., Qamar F. D., Ellison S. L., Bluck A. F. L., Simard L., Mendel J. T., Moreno J., Torrey P., 2016, *MNRAS*, 461, 2589 [73](#), [74](#), [75](#), [76](#), [77](#), [78](#), [87](#)
- Patton D. R., Torrey P., Ellison S. L., Mendel J. T., Scudder J. M., 2013, *MNRAS*, 433, L59 [62](#), [73](#), [78](#)
- Peebles P. J. E., 1969, *ApJ*, 155, 393 [18](#)
- Peng Y., Maiolino R., Cochrane R., 2015, *Nature*, 521, 192 [92](#)
- Peng Y.-j., et al., 2010, *ApJ*, 721, 193 [127](#), [139](#)
- Penzias A. A., Wilson R. W., 1965, *ApJ*, 142, 419 [3](#)
- Perez J., Michel-Dansac L., Tissera P. B., 2011, *MNRAS*, 417, 580 [48](#)
- Peterson B. M., 2014, *Space Sci. Rev.*, 183, 253 [28](#)
- Pillepich A., Nelson D., Hernquist L., Springel V., Pakmor R., Torrey P., Weinberger R., Genel S., Naiman J. P., Marinacci F., Vogelsberger M., 2018, *MNRAS*, 475, 648 [30](#), [44](#), [119](#), [120](#)
- Planck Collaboration Ade P. A. R., Aghanim N., Armitage-Caplan C., Arnaud M., Ashdown M., Atrio-Barandela F., Aumont J., Baccigalupi C., Banday A. J., et al. 2014, *A&A*, 571, A16 [49](#)
- Planck Collaboration Ade P. A. R., Aghanim N., Arnaud M., Ashdown M., Aumont J., Baccigalupi C., Baker M., Balbi A., Banday A. J., et al. 2011, *A&A*, 536, A1 [4](#), [7](#)
- Planck Collaboration et al., 2016, *A&A*, 594, A13 [3](#), [119](#)
- Planck Collaboration et al., 2018, arXiv e-prints, p. arXiv:1807.06209 [11](#), [14](#), [35](#)

BIBLIOGRAPHY

- Plewa T., 2001, in Zinnecker H., Mathieu R., eds, *The Formation of Binary Stars Vol. 200 of IAU Symposium, Numerical Hydrodynamics: SPH versus AMR*. p. 563 [39](#)
- Portinari L., Chiosi C., Bressan A., 1998, *A&A*, 334, 505 [44](#)
- Price D. J., 2008, *Journal of Computational Physics*, 227, 10040 [39](#)
- Pringle J. E., 1992, *MNRAS*, 258, 811 [100](#)
- Puchwein E., Sijacki D., Springel V., 2008, *ApJ*, 687, L53 [5](#), [19](#), [34](#), [96](#)
- Rees M. J., 1978, in Berkhuijsen E. M., Wielebinski R., eds, *Structure and Properties of Nearby Galaxies Vol. 77 of IAU Symposium, Emission from the nuclei of nearby galaxies - Evidence for massive black holes*. pp 237–242 [29](#)
- Rees M. J., Ostriker J. P., 1977, *MNRAS*, 179, 541 [18](#), [21](#)
- Renaud F., Bournaud F., Kraljic K., Duc P.-A., 2014, *MNRAS*, 442, L33 [59](#)
- Reynolds C. S., 2013, *Classical and Quantum Gravity*, 30, 244004 [28](#), [125](#), [126](#), [138](#), [146](#)
- Rezzolla L., Barausse E., Dorband E. N., Pollney D., Reisswig C., Seiler J., Husa S., 2008, *Phys. Rev. D*, 78, 044002 [106](#), [108](#), [147](#)
- Riess A. G., et al., 1998, *AJ*, 116, 1009 [12](#)
- Rodighiero G., et al., 2011, *ApJ*, 739, L40 [23](#)
- Rodriguez-Gomez V., Genel S., Vogelsberger M., Sijacki D., Pillepich A., Sales L. V., Torrey P., Snyder G., Nelson D., Springel V., Ma C.-P., Hernquist L., 2015, *MNRAS*, 449, 49 [50](#)
- Rodriguez-Gomez V., Snyder G. F., Lotz J. M., Nelson D., Pillepich A., Springel V., Genel S., Weinberger R., Tacchella S., Pakmor R., Torrey P., Marinacci F., Vogelsberger M., Hernquist L., Thilker D. A., 2019, *MNRAS*, 483, 4140 [113](#), [135](#), [139](#), [146](#)
- Rubin V. C., Ford Jr. W. K., Thonnard N., 1980, *ApJ*, 238, 471 [4](#)
- Rupke D. S. N., Kewley L. J., Chien L.-H., 2010, *ApJ*, 723, 1255 [48](#)
- Sabater J., Best P. N., Argudo-Fernández M., 2013, *MNRAS*, 430, 638 [76](#), [87](#)

- Salim S., Lee J. C., Davé R., Dickinson M., 2015, *ApJ*, 808, 25 [48](#), [72](#)
- Salpeter E. E., 1955, *ApJ*, 121, 161 [43](#)
- Sanders D. B., Scoville N. Z., Soifer B. T., 1991, *ApJ*, 370, 158 [56](#)
- Sanders R. L., Shapley A. E., Kriek M., Freeman W. R., Reddy N. A., Siana B., Coil A. L., Mobasher B., Davé R., Shivaee I., Azadi M., Price S. H., Leung G., Fetherholf T., de Groot L., Zick T., Fornasini F. M., Barro G., 2018, *ApJ*, 858, 99 [48](#), [72](#)
- Schaye J., Dalla Vecchia C., Booth C. M., Wiersma R. P. C., Theuns T., Haas M. R., Bertone S., Duffy A. R., McCarthy I. G., van de Voort F., 2010, *MNRAS*, 402, 1536 [23](#)
- Schaye J., et al., 2015, *MNRAS*, 446, 521 [30](#), [49](#), [96](#), [119](#)
- Schive H.-Y., Tsai Y.-C., Chiueh T., 2010, *ApJS*, 186, 457 [39](#)
- Schmidt M., 1963, *Nature*, 197, 1040 [27](#)
- Schmidt M., 1968, *ApJ*, 151, 393 [27](#), [32](#)
- Scoville N. Z., 2013, *Evolution of star formation and gas*. Cambridge University Press, p. 491 [56](#)
- Scudder J. M., Ellison S. L., Mendel J. T., 2012, *MNRAS*, 423, 2690 [74](#)
- Scudder J. M., Ellison S. L., Torrey P., Patton D. R., Mendel J. T., 2012, *MNRAS*, 426, 549 [5](#), [48](#), [59](#), [60](#), [61](#), [62](#), [68](#), [72](#), [75](#), [83](#), [86](#), [91](#), [144](#)
- Shakura N. I., Sunyaev R. A., 1973, *A&A*, 24, 337 [27](#), [30](#), [31](#), [98](#), [111](#)
- Shankar F., 2009, *New Astronomy Reviews*, 53, 57 [127](#), [128](#)
- Shapiro S. L., Lightman A. P., Eardley D. M., 1976, *ApJ*, 204, 187 [111](#)
- Sijacki D., Springel V., Di Matteo T., Hernquist L., 2007, *MNRAS*, 380, 877 [34](#), [96](#)
- Sijacki D., Springel V., Haehnelt M. G., 2009, *MNRAS*, 400, 100 [110](#)
- Sijacki D., Springel V., Haehnelt M. G., 2011, *MNRAS*, 414, 3656 [110](#), [132](#)

BIBLIOGRAPHY

- Sijacki D., Vogelsberger M., Genel S., Springel V., Torrey P., Snyder G. F., Nelson D., Hernquist L., 2015, MNRAS, 452, 575 [112](#)
- Sikora M., Stawarz Ł., Lasota J.-P., 2007, ApJ, 658, 815 [21](#)
- Silk J., 1977, ApJ, 211, 638 [18](#), [21](#)
- Skillman E. D., Kennicutt R. C., Hodge P. W., 1989, ApJ, 347, 875 [24](#)
- Smoot G. F., et al., 1992, ApJ, 396, L1 [4](#), [7](#)
- Sołtan A., 1982, Monthly Notices of the Royal Astronomical Society, 200, 115 [5](#), [27](#), [33](#), [95](#)
- Sparre M., Springel V., 2016, MNRAS, 462, 2418 [56](#), [57](#), [59](#), [87](#), [113](#)
- Sparre M., Springel V., 2017, MNRAS, 470, 3946 [49](#)
- Speagle J. S., Steinhardt C. L., Capak P. L., Silverman J. D., 2014, ApJS, 214, 15 [76](#)
- Spergel D. N., Verde L., Peiris H. V., Komatsu E., Nolta M. R., Bennett C. L., Halpern M., Hinshaw G., Jarosik N., Kogut A., Limon M., Meyer S. S., Page L., Tucker G. S., Weiland J. L., Wollack E., Wright E. L., 2003, ApJS, 148, 175 [4](#), [7](#)
- Springel V., 2005, MNRAS, 364, 1105 [37](#), [38](#)
- Springel V., 2010, MNRAS, 401, 791 [39](#), [49](#), [116](#), [117](#)
- Springel V., Di Matteo T., Hernquist L., 2005, MNRAS, 361, 776 [57](#), [96](#), [111](#)
- Springel V., Hernquist L., 2003, MNRAS, 339, 289 [41](#), [42](#), [43](#), [51](#), [117](#)
- Springel V., Pakmor R., Pillepich A., Weinberger R., Nelson D., Hernquist L., Vogelsberger M., Genel S., Torrey P., Marinacci F., Naiman J., 2018, MNRAS, 475, 676 [44](#), [119](#)
- Springel V., White S. D. M., Jenkins A., Frenk C. S., Yoshida N., Gao L., Navarro J., Thacker R., Croton D., Helly J., Peacock J. A., Cole S., Thomas P., Couchman H., Evrard A., Colberg J., Pearce F., 2005, Nature, 435, 629 [34](#), [50](#)
- Springel V., Yoshida N., White S. D. M., 2001, New A, 6, 79 [40](#)

- Stott J. P., Sobral D., Bower R., Smail I., Best P. N., Matsuda Y., Hayashi M., Geach J. E., Kodama T., 2013, *MNRAS*, 436, 1130 [48](#), [72](#)
- Strateva I., et al., 2001, *AJ*, 122, 1861 [21](#)
- Sutherland R. S., Dopita M. A., 1993, *ApJS*, 88, 253 [41](#)
- Tchekhovskoy A., Narayan R., McKinney J. C., 2011, *MNRAS*, 418, L79 [97](#)
- Teyssier R., 2002, *A&A*, 385, 337 [38](#)
- Teyssier R., Chapon D., Bournaud F., 2010, *ApJ*, 720, L149 [57](#)
- Thielemann F.-K., Argast D., Brachwitz F., Hix W. R., Höflich P., Liebendörfer M., Martinez-Pinedo G., Mezzacappa A., Panov I., Rauscher T., 2003, *Nuclear Physics A*, 718, 139 [44](#), [53](#)
- Thorne K. S., 1974, *ApJ*, 191, 507 [32](#), [100](#)
- Thorp M. D., Ellison S. L., Simard L., Sánchez S. F., Antonio B., 2019, *MNRAS*, 482, L55 [72](#), [91](#)
- Toomre A., 1977, in Tinsley B. M., Larson D. Campbell R. B. G., eds, *Evolution of Galaxies and Stellar Populations Mergers and Some Consequences*. p. 401 [5](#)
- Torrey P., Cox T. J., Kewley L., Hernquist L., 2012, *ApJ*, 746, 108 [48](#), [51](#), [53](#), [59](#), [68](#), [72](#), [91](#)
- Torrey P., Vogelsberger M., Hernquist L., McKinnon R., Marinacci F., Simcoe R. A., Springel V., Pillepich A., Naiman J., Pakmor R., Weinberger R., Nelson D., Genel S., 2018, *MNRAS*, 477, L16 [68](#), [69](#)
- Torrey P., Vogelsberger M., Marinacci F., Pakmor R., Springel V., Nelson D., Naiman J., Pillepich A., Genel S., Weinberger R., Hernquist L., 2019, *MNRAS*, 484, 5587 [48](#), [56](#), [68](#), [72](#)
- Torrey P., Vogelsberger M., Sijacki D., Springel V., Hernquist L., 2012, *MNRAS*, 427, 2224 [56](#)
- Travaglio C., Hillebrandt W., Reinecke M., Thielemann F.-K., 2004, *A&A*, 425, 1029 [44](#), [53](#)

BIBLIOGRAPHY

- Tremmel M., Governato F., Volonteri M., Quinn T. R., 2015, MNRAS, 451, 1868 [110](#), [147](#)
- Tremmel M., Karcher M., Governato F., Volonteri M., Quinn T. R., Pontzen A., Anderson L., Bellovary J., 2017, MNRAS, 470, 1121 [111](#)
- Tremonti C. A., Heckman T. M., Kauffmann G., Brinchmann J., Charlot S., White S. D. M., Seibert M., Peng E. W., Schlegel D. J., Uomoto A., Fukugita M., Brinkmann J., 2004, ApJ, 613, 898 [25](#), [47](#), [71](#), [76](#), [143](#)
- Vogelsberger M., Genel S., Sijacki D., Torrey P., Springel V., Hernquist L., 2013, MNRAS, 436, 3031 [51](#)
- Vogelsberger M., Genel S., Springel V., Torrey P., Sijacki D., Xu D., Snyder G., Bird S., Nelson D., Hernquist L., 2014, Nature, 509, 177 [119](#)
- Vogelsberger M., Genel S., Springel V., Torrey P., Sijacki D., Xu D., Snyder G., Nelson D., Hernquist L., 2014, MNRAS, 444, 1518 [96](#)
- Volonteri M., 2010, A&A Rev., 18, 279 [29](#), [111](#)
- Volonteri M., Sikora M., Lasota J.-P., 2007, ApJ, 667, 704 [101](#), [105](#), [139](#)
- Weinberger R., Springel V., Hernquist L., Pillepich A., Marinacci F., Pakmor R., Nelson D., Genel S., Vogelsberger M., Naiman J., Torrey P., 2017, MNRAS, 465, 3291 [31](#), [97](#), [109](#), [111](#), [112](#), [113](#), [114](#), [115](#), [125](#), [146](#)
- Weinberger R., Springel V., Pakmor R., Nelson D., Genel S., Pillepich A., Vogelsberger M., Marinacci F., Naiman J., Torrey P., Hernquist L., 2018, MNRAS, 479, 4056 [5](#), [30](#), [113](#), [125](#)
- Whitaker K. E., van Dokkum P. G., Brammer G., Franx M., 2012, ApJ, 754, L29 [22](#), [23](#)
- White S. D. M., 1984, ApJ, 286, 38 [18](#)
- White S. D. M., Rees M. J., 1978, MNRAS, 183, 341 [4](#), [18](#)
- Wiersma R. P. C., Schaye J., Smith B. D., 2009, MNRAS, 393, 99 [24](#), [41](#)
- Wilson A. S., Colbert E. J. M., 1995, ApJ, 438, 62 [21](#)
- Xu C., Livio M., Baum S., 1999, AJ, 118, 1169 [21](#)

Xu G., 1995, *ApJS*, 98, 355 [117](#)

Yabe K., Ohta K., Akiyama M., Bunker A., Dalton G., Ellis R., Glazebrook K., Goto T., Imanishi M., Iwamuro F., Okada H., Shimizu I., Takato N., Tamura N., Tonegawa M., Totani T., 2015, *pasj*, 67, 102 [48](#), [72](#)

Yoshida N., Omukai K., Hernquist L., Abel T., 2006, *ApJ*, 652, 6 [29](#)

Yoshisato A., Morikawa M., Gouda N., Mouri H., 2006, *ApJ*, 637, 555 [15](#)

Yuan F., Narayan R., 2014, *ARA&A*, 52, 529 [112](#)

Zajaček M., Tursunov A., Eckart A., Britzen S., 2018, *MNRAS*, 480, 4408 [29](#)

Zaritsky D., Kennicutt Jr. R. C., Huchra J. P., 1994, *ApJ*, 420, 87 [24](#)

Zeldovich Y., 1970, *Astronomy and Astrophysics*, 5, 84 [15](#)

Zwicky F., 1933, *Helvetica Physica Acta*, 6, 110 [4](#)

Acknowledgements

At the end of this adventure full of challenges and rewarding experiences, I can only feel an immense gratitude toward those that were present during this period of my life. Without their support, encouragement and advice, the culmination of this thesis would not have been possible.

First of all, I would like to express my sincerest gratitude to my advisor Volker Springel for giving me the great opportunity to work with him and do frontier science. His guidance, his support and his willingness to help me with all sort of problems I encountered during my PhD made me a better scientist. In addition to this, the experience of working and living in Germany has changed me personally in many positive ways. I also thank Andreas Just, who kindly agreed to referee this thesis and welcomed me in his group during the last year of my PhD.

I would like to specially thank Martin Sparre for all his support, his friendship and his encouragement to pursue a secondary PhD project that now comprises a part of this thesis. My heartfelt thanks also go to the rest of my colleagues at the Theoretical Astrophysics group at HITS, Christian Arnold, Christine Simpson, Dandan Xu, Felipe Goicovic, Freeke van de Voort, Jolanta Zjupa, Kevin Schaal, Rainer Weinberger, Robert Grand, Svenja Jacob and Thomas Guillet, also to my new office mates Branislav Avramov and Matteo Mazzarini, I really enjoyed working with you. I graciously acknowledge funding by the Deutscher Akademischer Austauschdienst (DAAD); without their support, this journey would not have been possible. Moreover, I wish to acknowledge the support from the International Max Planck Research School for Astronomy and Cosmic Physics at the University of Heidelberg.

I feel deeply thankful to my family in Colombia: my father Anibal Bustamante, my mother Gilma Jaramillo and my brother Santiago Bustamante. Without their unconditional love, their support and their faith in me, I would not be standing where I am now and I would not be the person I have become. To them I dedicate this thesis. I am also very grateful to my girlfriend Laura Armbruster for her love, for being there for me and for making me feel like home. Last but not least, I thank my friends Ana Herrera, Sergio Avila, Natalia Pacheco, Phillip Lang, Yulong Zhuang, Kristian Ehlert, Felipe Goicovic and many others for all their support and unforgettable moments. You have been a second family in Germany.